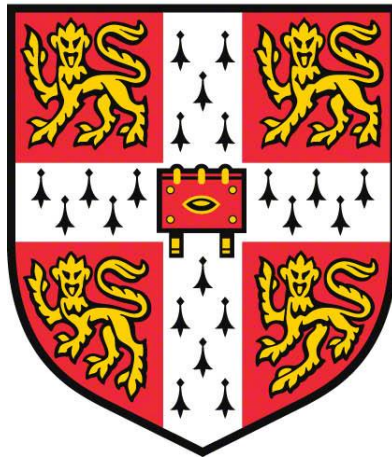# Flexible Polymer Waveguides for High-Speed Short-Reach Links

Fengyuan Shi

Sidney Sussex College

Department of Engineering

University of Cambridge

THIS DISSERTATION IS SUBMITTED FOR THE DEGREE OF DOCTOR OF PHILOSOPHY

May 2019

DECLARATION

This dissertation is the result of my own work and includes nothing which is the outcome of work done in collaboration except where specifically indicated in the text.

It is not substantially the same as any that I have submitted, or, is being concurrently submitted for a degree or diploma or other qualification at the University of Cambridge or any other University or similar institution except as declared in the Preface and specified in the text. I further state that no substantial part of my thesis has already been submitted, or, is being concurrently submitted for any such degree, diploma or other qualification at the University of Cambridge or any other University or similar institution except as declared in the Preface and specified in the text. It does not exceed the prescribed word limit for the relevant Degree Committee.

_____

Fengyuan Shi

Cambridge, May 2019

I

FLEXIBLE POLYMER WAVEGUIDES FOR HIGH-SPEED SHORT-REACH LINKS

FENGYUAN SHI

ABSTRACT

This dissertation presents a detailed study of flexible polymer waveguides for used in short-reach communication links. Flexible polymer waveguides enable a wider range of applications as compared to the rigid polymer waveguides, especially for the rack-to-rack links and data bus systems in autonomous car and avionic industry. However, their optical performance including bending and twisting loss, crosstalk, bandwidth and mode coupling behaviour hasn't been studied in detail when the flexure is applied to the waveguide. This research quantifies those performances when flexible polymer waveguides are being flexed and provides a useful guideline when designing those flexible polymer links in the real world. In addition, some suggestions have been discussed, which can be used to improve waveguide loss performance. A lot simulation work has been done to support the observations from the experimental results. The flexible polymer waveguides are proven to be robust and have low propagation loss (0.03 dB/cm) and high temperature resistance (up to 350 °C). They can be bent down to 2 mm without cracks and the resultant excess bending loss can be less than 2 dB. The excess twisting loss is also shown to be very low, around 0.02 dB for $4 \times 360°$ full twisting turns as long as lateral tension is carefully reduced. The crosstalk results reveal their values are < -25 dB under any launch conditions when waveguides are flexed. The dynamic behaviour study shows that flexible polymer waveguides are robust and can work dynamically for a long-time horizon. In addition, a new design of flexible polymer waveguides has been proposed which can reduce the excess bending loss to around 0.5 dB at 2 mm bending, which is a big improvement. As for the mode coupling behaviour, both simulation and experimental works have been done to investigate how optical modes will evolve due to the small bends, micro bends and rough sidewalls. A better understanding of propagation mechanism inside waveguide is given and discussed. Then, the ultra-short laser pulse measurements are carried out to get the bandwidth length products (BLP) of the waveguides under flexure. The results indicate polymer waveguide can support over 100 GHz×m BLP and small bends have the ability of improving bandwidth performance further. At last, a 40 Gbps transmission over 1-m spiral flexible polymer waveguides under different bending radius has successfully been demonstrated.

ACKNOWLEDGEMENTS

ABSTRACT

This dissertation presents a detailed study of flexible polymer waveguides for used in short-reach communication links. Flexible polymer waveguides enable a wider range of applications as compared to the rigid polymer waveguides, especially for the rack-to-rack links and data bus systems in autonomous car and avionic industry. However, their optical performance including bending and twisting loss, crosstalk, bandwidth and mode coupling behaviour hasn't been studied in detail when the flexure is applied to the waveguide. This research quantifies those performances when flexible polymer waveguides are being flexed and provides a useful guideline when designing those flexible polymer links in the real world. In addition, some suggestions have been discussed, which can be used to improve waveguide loss performance.

A lot simulation work has been done to support the observations from the experimental results. The flexible polymer waveguides are proven to be robust and have low propagation loss (0.03 dB/cm) and high temperature resistance (up to 350 °C). They can be bent down to 2 mm without cracks and the resultant excess bending loss can be less than 2 dB. The excess twisting loss is also shown to be very low, around 0.02 dB for $4 \times 360°$ full twisting turns as long as lateral tension is carefully reduced. The crosstalk results reveal their values are < -25 dB under any launch conditions when waveguides are flexed. The dynamic behaviour study shows that flexible polymer waveguides are robust and can work dynamically for a long-time horizon. In addition, a new design of flexible polymer waveguides has been proposed which can reduce the excess bending loss to around 0.5 dB at 2 mm bending, which is a big improvement.

As for the mode coupling behaviour, both simulation and experimental works have been done to investigate how optical modes will evolve due to the small bends, micro bends and rough sidewalls. A better understanding of propagation mechanism inside waveguide is given and discussed. Then, the ultra-short laser pulse measurements are carried out to get the bandwidth length products (BLP) of the waveguides under flexure. The results indicate polymer waveguide can support over 100 GHz×m BLP and small bends have the ability of improving bandwidth performance further. At last, a 40 Gbps transmission over 1-m spiral flexible polymer waveguides under different bending radius has successfully been demonstrated.

LIST OF PUBLICATIONS

[1] Shi, F., Bamiedakis, N., Vasil'ev, P.P., Penty, R.V., White, I.H. and Chu, D., 2018. Flexible multimode polymer waveguide arrays for versatile high-speed short-reach communication links. Journal of Lightwave Technology (JLT), 36(13), pp.2685-2693.

[2] Bamiedakis, N., Shi, F., Chu, D., Penty, R.V. and White, I.H., 2018. High-Speed Data Transmission Over Flexible Multimode Polymer Waveguides Under Flexure. IEEE Photonics Technology Letters (PTL), 30(14), pp.1329-1332.

[3] Shi, F., Bamiedakis, N., Penty, R.V., White, I.H. and Chu, D., 2018, November. Flexible Polymer Waveguide Technology for Low-Cost In-Car and In-Plane Optical Interconnects. In 2018 IEEE Avionics and Vehicle Fiber-Optics and Photonics Conference (AVFOP) (pp. 1-2). IEEE.

[4] Shi, F., Bamiedakis, N., Penty, R.V., White, I.H. and Chu, D., 2017, April. Flexible Multimode Polymer Waveguides for High-Speed Optical Interconnects. The 19th edition of the European Conference on Integrated Optics (ECIO), T4.4.

[5] Bamiedakis, N., Shi, F., Chu, D., Penty, R.V. and White, I.H., 2017, July. Flexible multimode polymer waveguides for versatile high-speed optical interconnects. In 2017 19th International Conference on Transparent Optical Networks (ICTON) (pp. 1-4). IEEE.

[6] Bamiedakis, N., Shi, F., Chu, D., Penty, R.V. and White, I.H., 2019, March. Mode-mixing in multimode polymer waveguides for on-board optical interconnects. In Optical Interconnects XIX (Vol. 10924, p. 1092404). International Society for Optics and Photonics (Photonics West).

[7] Bamiedakis, N., Shi, F., Chu, D., Penty, R.V. and White, I.H., 2018, February. Flexible multimode polymer waveguides for high-speed short-reach communication links. In Optical Interconnects XVIII (Vol. 10538, p. 105380N). International Society for Optics and Photonics (Photonics West).

[8] Li D., Shi, F., Ding Y., Bamiedakis, N., Liaw S.K. and Chu, D., 2018, February. Characteristics Measurement and Evaluation of Polymer Optical Waveguide at Different Laser Wavelengths. International Conference on Network Communication and Computer (ICNCC 2018), Paper ID: N3003.

[9] (Accepted) Shi, F., Bamiedakis, N., Penty, R.V., White, I.H., Chu, D., 2020, February. Bending loss improvement and twisting loss study of flexible multimode polymer waveguides. In Optical Interconnects XVIII. International Society for Optics and Photonics (Photonics West).

TABLE OF CONTENTS

Chapter 5 Analysis of mode coupling in flexible polymer waveguides 104

Chapter 6 Bandwidth investigation of flexible polymer waveguides 122

LIST OF FIGURES

XIV

XV

XVI

XVII

XVIII

XIX

XX

LIST OF TABLES

LIST OF ABBREVIATIONS

AC	Auto-Correlator
AOC	Active Optical Cable
BLP	Bandwidth Length Produce
CAN	Controller Area Network
CCD	Charge-Coupled Device
D2B	Domestic Digital Bus
E/O	Electrical-Optical
EMI	Electromagnetic Interference
EUC	Electronic Unit Controller
FBL	Fly-By-Light
FBW	Fly-By-Wire
FFA	Far-Field Angle
FR4	Flame Retardant 4
FWHM	Full Width at Half Maximum
HD	High-Definition
HPC	High Performance Computing
IDB	Internal Data Bus
IPA	Isopropyl Alcohol
LED	Light Emitting Diode
LC	Liquid Crystal
LIN	Local Interconnect Network
MMF	Multimode Fibre
MOST	Media Oriented Systems Transport
NA	Numerical Aperture
NRZ	Non-Return-To-Zero
O/E	Optical-Electrical
PAL	Phase Alternating Line
PAM	Pulse Amplitude Modulation

PCB	Printed Circuit Board
PD	Photodetector
PDL	Polarisation dependent loss
PDMS	Polydimethylsiloxane
PMMA	Poly(methyl methacrylate)
POF	Plastic Optical Fibre
RC	Resistor–Capacitor
RH	Relative Humidity
RIE	Reactive Ion Etching
RMS	Root-Mean-Square
RPM	Rotations Per Minute
SHG	Second Harmonic Generation
SMF	Single Mode Fibre
TE	Transverse Electric
TIR	Total Internal Reflection
TM	Transverse Magnetic
UV	Ultra-Violet
VCSEL	Vertical Cavity Surface-Emitting Laser
VGA	Video Graphics Array

Chapter 1 Introduction

This chapter introduces the history of fibre optics and shows the motivation behind developing multimode polymer waveguides, especially flexible polymer waveguides. An overview of polymer waveguide technology and the progress to date are presented in this chapter. The main applications are reviewed, such as high-performance computing (HPC) servers in data centres, autonomous cars, and avionic airplanes based on polymer waveguide technology. Then, the main challenges of developing such flexible polymer waveguides and their corresponding potential solutions are given and discussed. The last section presents the aims and structure of the dissertation.

1.1 Motivation of developing polymer waveguides

The very earliest communications were implemented by using smoke signals. Then, in 1839, the first experimental electrical telegraphy was developed. Before 1964, a wide range of telecommunications networks were built based on copper cables. However, copper is very heavy, especially for long-haul communications where a few tons of weight is not acceptable. In addition, the bandwidth of the copper link is not enough to meet future data demand. To reduce the weight and increase bandwidth, fibre optics were widely regarded as the most promising candidate for achieving long-haul communication, especially for undersea communication networks. However, the development of optical communication was stagnant due to the large fibre loss (~ 20 dB/km). During the year of 1966, two researchers, C. K. Kao and M. W. Jones, found that such a big fibre loss was caused mainly due to impurities in the glass [1]. By employing better manufacturing processes and getting rid of impurities, the fibre loss was dramatically reduced to 4 dB/km [2]. Today, fibre loss as low as 0.15 dB/km can be achieved by employing current fabrication technologies [3], and over 150 Gbps data transmission rate on a single fibre channel has been successfully demonstrated [4]. Submarine communication cables and mainland network links are all made of optical fibres. With the reduction in fibre cost, city residents have started to replace their copper house communication links with optical fibres in order to increase their download speed. As shown in Figure 1, during the past few decades, optical fibres have replaced traditional copper links in many areas such as telecoms and

datacoms, because fibre optics provide great advantages such as low attenuation, immunity to electromagnetic interference, less power consumption (Normally, a 10 Gbps transceiver in a copper system uses about 6 watts of power while a comparable 10 Gbps optical transceiver uses less than 1 watt to transmit the same signal), smaller size, lighter weight, and much larger bandwidth. It is widely believed that this trend will continue, and nowadays, fibre optics are replacing copper wires at the board level, initiating what has been named as the computer-com era.

WAN,MAN Metro, long-haul	LAN campus, enterprise	System intra/inter-rack	Board Module-module	Board Module-module	Chip On-chip buses
Tele-com	Data-com	Computer-com			
Multi-km Cards	100's m Card edge	10's m Card edge	< 1 m Module	< 10 cm Si C or chip	< 20 mm On chip
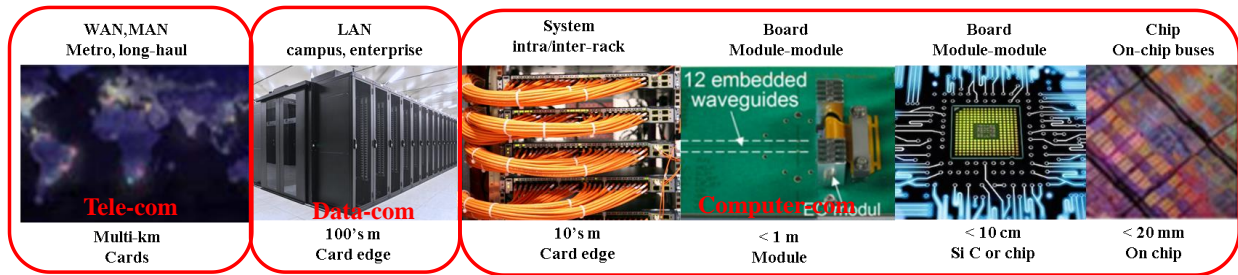
Figure 1 Evolution of fibre optics from telecom to computer-com era [5]. Transmission distance decreases from multi-km range to few-meter range.

In recent years, there has been a rapid increase in data traffic due to the expansion of personal electronic devices. Figure 2 summarises and forecasts the application traffic growth from 2017 to 2022 and reveals that data traffic will reach around 400 Exabytes per month, which is four-fold compared to data traffic in 2017. Such a huge jump in data traffic will require high bandwidth in the link channel to support chip to chip and board to board communications. However, due to the effect of noise and interference, the speed of copper interconnections cannot run higher than a few gigahertz [6]. Building a 3-D structure for the board would be a temporary solution, but it requires much more effort and expenditure. In addition, electrical cables face a fundamental 'communication bottleneck'. When signals operate at a high frequency, the skin effect becomes severe, resulting in a large resistance inside the link and degrading the performance. Another bottleneck of electrical cables would be crosstalk: electromagnetic interference from a neighbouring channel will generate disturbance on the current channel. Although researchers are trying to reduce these problems, sophisticated techniques are needed, which will increase the cost of the whole system and reduce the stability. One promising technique to solve this bandwidth problem would be employing fibre optics as on-board communication links, which has the potential of supporting transmission at a few hundred Gbps.
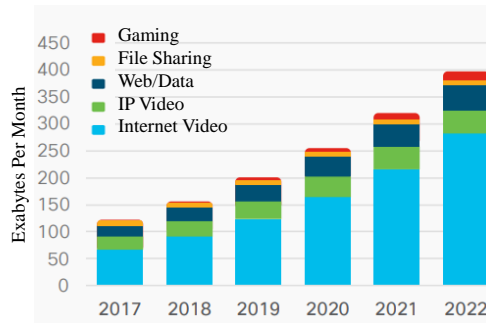
Figure 2 Cisco global IP traffic forecast based on applications from the year of 2017 to 2022 [7].

Goodman proposed using fibre optics to build the interconnections on a chip for the first time in 1984 [8] and later, a variety of research has been done on optical interconnects [9-11]. Currently, there are three main methods for achieving optical interconnects on board: free-space connections, optical fibres embedded in substrate connections, and polymer material-based waveguide connections. Figure 3 shows these three different types of configuration.
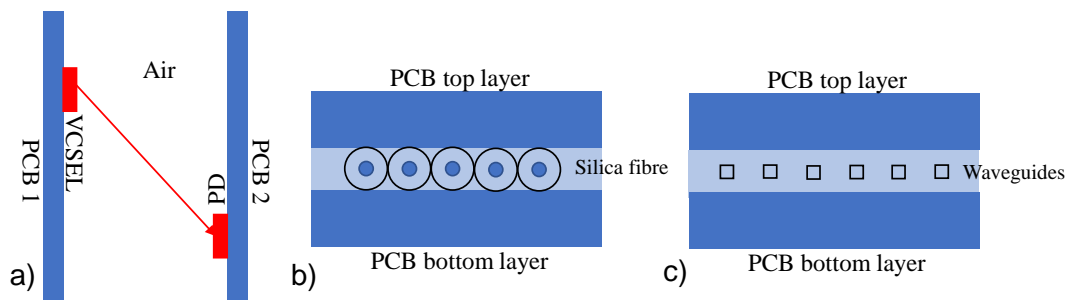
Figure 3 Three different methods for achieving optical interconnects, a) free -space connection, b) embedded fibre connection and c) polymer waveguide-based connection.

There are many research groups studying these three configurations and details of their research work can be found in: free-space [12-15], optical fibres embedded [16-19], and polymer waveguides [20-23]. This section gives a brief introduction to each configuration. For free-space interconnects, a laser and photodetector pair need to be installed on each electronic card. The laser is directly modulated with the data signal. The data is transmitted to the other card via the free space medium. Due to the divergence of the laser diode, a lens is needed to converge the laser beam, which increases the system complexity. In addition, there is a high requirement for the system alignment, especially when two cards are placed far away with each other. The most severe drawback of free space

interconnects is that this free space medium can be easily influenced by the environment such as air disturbance, dust, and temperature. These effects could significantly degrade the system performance.

For fibre embedded interconnects, burying silica fibres inside the substrate can provide much higher performance in terms of propagation loss and bandwidth. Figure 3 demonstrates a fibre embedded array. It is also easy to connect to this fibre array using the MT connector, which is currently commercially available. The main challenge of this method is the cost. Traditional printed circuit boards (PCBs) are made layer by layer with a final lamination process. When fibre arrays are put between, it is easy to break the fibres. Therefore, a separate process needs to be taken to protect the fibre from damage, which makes this method not suitable for integration. Meanwhile, optical PCBs need much more complex optical layouts rather than just a straight fibre link, such as crossings, Y-splitter, and combiners. Using optical fibres to implement those structures would be very difficult and the whole system cost would be unaffordable.

Finally, polymer waveguide based optical interconnects are widely regarded as the most promising candidate for achieving on-board interconnects. Polymer waveguide technology provides low-cost fabrication of optical PCBs with a relaxed tolerance and a high bandwidth. The basic idea of polymer waveguides is to generate a channel within which light can propagate. The most common shape of this channel cross-section is square, and the fabrication process is based on layer by layer steps. Both rigid and flexible polymer waveguides can be fabricated by depositing waveguides on different substrates. Due to the nature of the polymer material, polymer waveguide fabrication can be integrated into the traditional PCB fabrication process providing a low-cost solution. Polymer waveguides also provide a stable connection between the two ends, and complex structures can also be easily built based on polymer waveguide technology. Meanwhile, recent research indicates that they have the ability to support > 100 Gb/s transmission, which is enough to satisfy future data traffic demand.

1.2 Current polymer waveguide technology and applications

As mentioned, polymer waveguides can be divided into two groups: rigid and flexible. Significant research has been carried out on rigid polymer waveguides in recent years [24-26] and numerous demonstrations have been made of optical backplanes based on polymer multimode waveguides [27-30]. These waveguides have been shown to exhibit relatively large bandwidth-length products in excess of 30 GHz×m [31] despite their highly multimode nature, whilst data transmission of 40 Gb/s using non-return-to-zero (NRZ) modulation [32] and 56 Gb/s using 4-level pulse-amplitude modulation (PAM-4) [33] have been demonstrated over a 1 m long spiral multimode polymer waveguide. The combination of large parallel waveguide arrays and high-speed VCSEL arrays can provide low-cost optical board-level interconnection with aggregate data capacities over 1 Tb/s [27]. There is also a group from Keio University focusing on generating circular core polymer waveguides using the Mosquito method. By controlling the speed and monomer wetting, they can control the position and the size of the waveguide core. After diffusion, a graded index profile can be generated which is similar to the optical fibre [34]. Another group from Germany are concentrating on fabricating an on-board optical coupler for polymer waveguides [35]. This polymer waveguide-based coupler is interruption-free which makes it suitable for building optical data bus systems and interruption-free means the waveguide core is intact. Similar to the above research, significant works by different groups are ongoing for rigid polymer waveguides, therefore, the performance of polymer waveguides is improving.

Flexible polymer waveguides also have attracted much more attention in recent years due to the future trend of developing flexible electronics. Flexible polymer waveguides can be made by depositing polymer waveguides onto a flexible substrate, normally polyimide. The application of polymer waveguides, therefore, can be dramatically extended, especially in some spaces where shape and weight are quite important to the system. Developing flexible polymer waveguides also helps to diversify the electro-optical assembly platform, and thin flexible waveguides offer the great advantage of being stacked for complex routing and enhanced bandwidth [36]. Various flexible multimode polymer waveguide technologies have been developed by different groups, and some studies on the

performance of the waveguides under flexure have been reported [36-42]. For example, in [36], bending loss measurements on flexible multimode waveguides using a 62.5 μm multimode fibre (MMF) input indicated that no significant bending loss is induced by a 360° bend for a radius larger than 3 cm. In [40] bending loss studies were carried out on flexible waveguides, demonstrating a 4.3 dB excess loss when the sample is bent at 5 mm under a 9 μm SMF input. Similar studies are reported in [37]. The focus however of these publications has been the development of flexible waveguides and their related opto-electronic sub-assemblies rather than the performance of the waveguides when flexure is applied. Additionally, none of the aforementioned studies consider the fact that the loss performance of such waveguides strongly depends on the launch conditions employed due to their highly-multimoded nature. Currently, the best propagation loss for polymer waveguides is around ~0.03 dB/cm and can be further reduced in the future by reducing the roughness of the waveguide side walls. Polymer waveguides have a relatively large alignment tolerance due to the large core size. Normally, 10 μm offset misalignment will result in around 1 dB power drop, which is suitable for commercial pick-and-place tools. In addition, the crosstalk between adjacent waveguides is less than -40 dB, and the bandwidth has been shown to support >100 GHz×m bandwidth length product (BLP).

1.3 Review of polymer waveguide technology applications

1.3.1 Polymer waveguide technology for data centre

The dramatic growth of traffic data via the cloud, computers, and smart mobiles has been the main driving factor for optical interconnects [43]. There were 2.46 billion worldwide social network users in 2017, and this number is expected to increase to 3.02 billion by 2021 [44]. According to the statistics [44], Facebook had 2271 million active users in January 2019, followed by YouTube which has 1900 million active users. WhatsApp, Facebook Messenger and WeChat ranked 3rd, 4th and 5th, with 1500 million, 1300 million and 1083 million active users, respectively. Those numbers are increasing constantly as more and more wireless device infrastructure and networks are installed worldwide. Therefore, it has been predicted that by 2025, 163 trillion GBs of data will exist [45]. All this data has to be stored, processed and shared among a number of data centres which are located all over the world. Therefore, the current network is built based on the support of those data centres.

Such huge data exchange between users requires high bandwidth links communicating between card-to-card and rack-to-rack.

Over the past few decades, optics have been replacing copper in telecom and datacom areas and boosted their development. History has proven the great success of employing optics for data communication. To meet future data demands, the next generation of optics technology for data centres and High-Performance Computing (HPC) needs to be developed. Simply increasing the number of cores cannot satisfy ambitious targets anymore, as size fragmentation has already reached its limits [46]. On-board chip-to-chip communication and intra-rack design are regarded as effective methods in the industry to reduce physical space, resources and complexity. There are three different types of interconnects for data centres: on-board interconnects, board-to-board interconnects and rack-to-rack interconnects. For a typical board, chip processors and memories are located in different positions. A router is needed on-board to communicate between processors and memories. For traditional copper wire, the following equation indicates the maximum bandwidth for electrical lines [47], where A is the cross-sectional area of wiring, L is the length of the wire, and B_0 is a constant [48] which is equal to around 10^{16} bits/s for RC limited lines.

$$B = B_0 \frac{A}{L^2} \qquad\qquad (\;1\;)$$

Recent analysis shows that a 1 m long electrical line on a standard FR4 is limited to 5 Gb/s [49] and this limitation can be pushed to around 15 Gb/s by using new advanced materials [50]. However, the whole cost of the FR4 board would be much more expensive and complex. In addition, it is very difficult to increase this value over 20 Gb/s for electrical lines. Therefore, developing a high-speed PCB board with low-cost fabrication techniques is quite challenging. Polymer waveguide technology is regarded as one of the most promising candidates to solve this problem.

Figure 4 shows the on-board interconnects implemented using polymer waveguides. To make communications on board among the chips, o/e and e/o conversion units must be installed. One challenge is to increase the alignment tolerance so that laser light can be easily coupled into waveguides, and another challenge it to design appropriate architecture that could reduce the number of o/e/o units used on board.
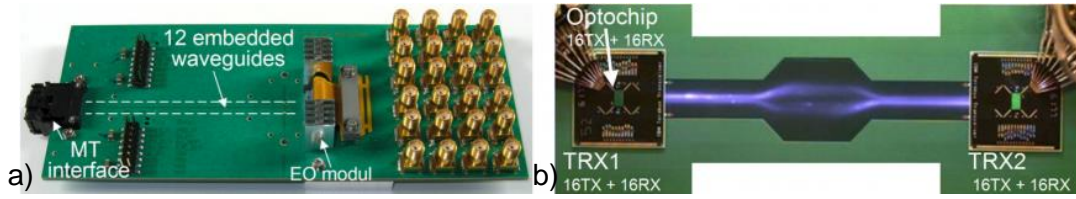
Figure 4 Demonstration of polymer waveguide links on-board. a) 12 parallel polymer waveguides are embedded in PCB

substrate with EO modules and MT interface at each end. b) polymer waveguides with a Y-splitter and a Y-combiner

embedded in PCB substrate [26].

The next level of optical interconnects hierarchy for data centre is board-to-board interconnects. An on-board optical interface is also designed to allow communication between boards and reduce the number of o/e/o units. This situation happens when data from one board needs to go to another board on the same backplane. Figure 5 shows one method of achieving this board-to-board communication. There is an optical bus link on the side and each board is connected to this bus link via its own optical interface. A micro lens and reflective mirror are needed at the conjunction point to change the direction of the optical signal. In most applications, designs require that the boards are pluggable so that users can easily change the board if it breaks. Another method achieving board-to-board communication would be using flexible polymer waveguides. Two boards are connected not through the optical data bus link, but via flexible polymer waveguides. It is easy to connect two boards with the help of an MT connector. Stacked flexible polymer waveguides also offer the ability for communication between multi-boards. The flexible polymer waveguide method can provide a relatively more stable connection and does not need other optical components such as mirror and lens.
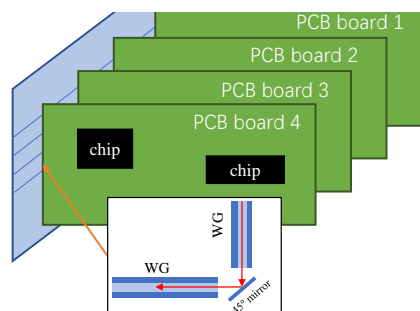
Figure 5 Schematic of board-to-board communications based on optical backplane topology. Four electronic PCBs are

plugged into optical backplane and a 45° reflective mirror is employed to change the signal direction.

Rack-to-rack interconnects need to be built when different servers need to share data with each other. As data centres become larger and larger, the data traffic from rack to rack also increases dramatically. Currently, active optical cables (AOCs) are widely introduced into data centres to replace traditional copper links to support such high data traffic. AOC is a type of cable which has electrical connectors at both ends and uses electrical-to-optical conversion on the cable ends to improve the speed and distance performance of the cable without sacrificing compatibility with standard electrical interfaces. In the near future, when optical PCBS have replaced electrical PCBs in data centres, AOCs will not be needed anymore. Only passive links need to be built between racks. Optical fibre would be the best candidate, however the expensive cost of optical fibre makes it unattractive. In addition, a fibre-based method for on-board communication is hard to achieve as glass is easy to break. As a result, for high-level integration, polymer waveguide technology is much better than optical fibre and, in the meantime, it can provide a low-cost fabrication process. It is better to develop a low-cost flexible polymer waveguide link for rack to rack communication to match the cross-section of a polymer waveguide for on-board and board-to-board communication. Flexible polymer waveguides would be the best solution, as they can provide communication over distances ranging from 1 m to dozens of metres.

In summary, polymer waveguides can support a high data rate for on-board, board-to-board and rack-to-rack communication in a data centre. Also, flexible polymer waveguides enable more applications where space is limited. The most important reason for employing polymer waveguide interconnects in data centres is cost related. Polymer material can enable a low-cost fabrication process. However, some challenges remain to be solved, for example, designing an easy, reliable and stable connector for polymer waveguides is still a problem.
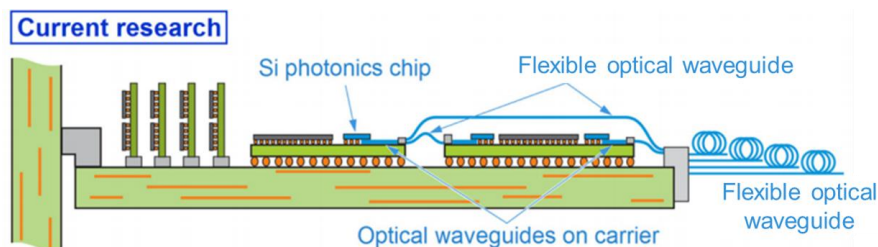
Figure 6 Optical polymer waveguides connecting chips assembled on carriers. Flexible optical waveguides are employed to

make chip-to-chip and board-to-board communications as suggested in figure [51].

1.3.2 Polymer waveguide technology for autonomous cars

Another future application of polymer waveguide technology autonomous car. In automotive networking, electrical and electronic systems are not independent but will influence and complement each other. With the increase in the number of electronic units inside a vehicle, a simple and highly efficient communication system needs to be built. However, a significant number of cable lines and plug connections makes the car heavy and redundant. The solution to this challenge will be introducing serial data bus systems which allow large volumes of data from different electronic units to be transferred. In 1991, the first serial bus system called Controller Area Network (CAN) was built by Mercedes-Benz and was used in the Mercedes-Benz 500E. Details of the CAN bus system can be found in [52-55]. The CAN bus was mainly designed for the automation field, and can be classified as high-speed CAN and low-speed CAN. A high-speed CAN system can be up to 1 Mbit/s and can be used to achieve real-time applications such as engine management systems, electronic transmission control and vehicle stabilisation systems. The data speed of a low-speed CAN system is around 100 Kbit/s, and this system can be used in comfort and body areas such as seat adjustment and control of the air-conditioning system. However, this CAN bus seems to be very inefficient due to the increasing use of mechatronic systems inside a car. Thus, in 1998, several vehicle manufacturers collaborated to try to build a cost-effective bus system as an alternative to replace the low-speed CAN bus system. The Local Interconnect Network (LIN) bus system was invented by this workgroup and introduced to Mercedes-Benz SL first in early 2001. The LIN bus is designed for sensors and actuator networking, and also provide a very low data rate, around 20 KBit/s. The LINK bus system is used as a subsystem of the CAN bus system and is responsible for control of door locking, climate regulation, and light & rain sensing. Detailed specifications of the LIN bus can be found in [56-58], which defines transmission protocols, transmission medium, and interface standard.

With increases to people's life quality, people are no longer satisfied with buying a car that can only be used as a commuting tool. Therefore, manufacturers have introduced infotainment systems into cars to meet people's requirements. However, audio and video, especially high definition (HD) video transmission, require a very high data rate. Electromagnetic interference (EMI) is another problem affecting the performance of an electrical bus. A fibre-optic data link can provide a high data rate as well as immunity to EMI. Thus, building an optical data bus seems to be the best solution. In

1998, the first optical fibre-based data bus, called a digital domestic bus (D2B), was successfully introduced into Mercedes-Benz cars [59, 60] with a data operating rate of 11.2 Mega-baud. The D2B bus employs a ring bus topology and 1 mm core diameter polymer optical fibres (POFs). Red light-emitting diodes (LEDs) are used as transmitters in this system. Such a high-speed optical data bus can support the transmission of audio and video in a car via low-cost means [61]. Therefore, some other alternative data buses based on optical links have been proposed, such as ByteFlight bus, FlexRay bus and Media Oriented Systems Transport (MOST) bus. ByteFlight bus was proposed by BMW, together with some other manufacturers, and this data bus was designed to solve safety-related problems [62]. Using fibre optics, ByteFlight provides a data rate of 10 Mbps and shows many advantages compared to previous data buses, such as fast reaction times, low system cost, and suitability for an increased number of functions [63]. Similarly, the FlexRay bus is also based on fibre optics and provides high-speed, deterministic and fault-tolerant communication. The first FlexRay bus was successfully introduced into cars in 2006 with an operating data rate of 10 Mbps. Details of the FlexRay bus can be found in [64, 65]. The last and most popular fibre-based vehicle data bus is the MOST bus. The MOST bus was also developed by BMW (along with DaimlerChrysler, Harman/Becker, and Oasis Silicon Systems) in 1998 and was initially designed for all kinds of automotive multimedia applications such as audio, video, CD players, GPS navigation, and telecommunication [66]. The MOST bus adopted ring bus topology [67] and its generic architecture is given in Figure 7.
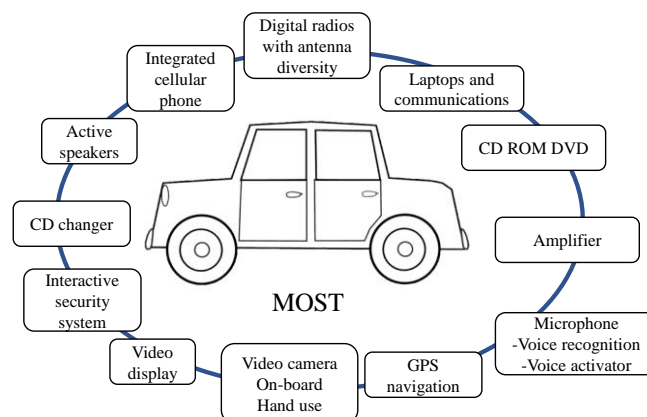
Figure 7 Generic architecture of Media Oriented Systems Transport (MOST) data bus system. Each unit is connected via

POF link based on ring topology.

Each unit is this bus is based on a point-to-point network connected by plastic optical fibres (POFs). Any device, such as video, GPS navigation, CD, and DVD, can be plugged into this ring bus and the data signal will experience O/E and E/O conversions. The first MOST bus was called MOST25 which permits ~23 Mbps data transmission. A few years later, MOST50 was proposed, which doubled the transmission speed and in October 2007, the latest MOST bus (MOST150) allows ~150Mbps transmission. Its physical layer was still based on the POF link [68, 69].

Different bus systems may communicate with each other via a hub or a gateway. Currently the most popular optical data bus for cars is the MOST bus, which as previously mentioned can carry a maximum 150 Mbps data rate and is used in more than 150 car models including Audi, BMW, VOLVO, Land Rover, etc. since 2001. However, 150Mbps seems still not to be enough for future requirements. In order to further improve the data rate, the MOST data bus organisation is preparing to publish a high data transmission rate of 1.5 Gbit/s standard. Alternatively, another data bus called the Intelligent transportation systems Data bus (IDB)-1394a was recently proposed, which allows 400 Mbps transmission in a car [19], and its next version IDB-1394b will be designed to support 3.2 Gbps transmission. The following table summarises the required data speeds of different video formats required inside a car. One thing that must be mentioned is that all the data rates are calculated based on an uncompressed format. From this table, if 4K screens are to be installed in cars, an optical data bus must be installed that is capable of greater than 10 Gbit/s.

Table 1 Data transmission rate required for common video standards without video compression technique involved [21], i is for interlaced video and p for progressive scan.

Standard	Resolution	Frame rate	MPixel/s	RGB24 (bit/s)
VGA	640*480	60p	18.4	442.4 M
PAL	720*576	50i	10.4	249.8 M
Full HD	1920*1080	60p	124.4	2986 M
4K	3840*2160	60p	497.7	11.9 G
8K	7680*4320	120i	1990.6	47.8 G

Over the past few decades, the data demand for vehicles has undergone a significant increase. More and more electronic units (estimated over 3000) have been added into vehicles, and it is roughly estimated that the cost of electrical and electronic unit controllers (EUCs) will occupy 20–40% of a regular car price [70]. On the other hand, the many EUCs and their cables increase the car weight. According to [71], approximately 100 kg of wires are added to a typical car. In order to increase the bandwidth and reduce the car weight, polymer waveguides could be a competing technology for the automotive industry.

1.3.3 Polymer waveguide technology for avionic industry

The wiring system in the aircraft controls different functions from antennas and landing gears to audio and entertainment devices. According to estimations, there are more than a hundred miles of electrical cables on an aircraft, which dramatically increases the aircraft weight. Electromagnetic interference (EMI) also causes severe problems when maintenance is not done properly. Such a huge number of electrical cables bundled together can easily cause system failure and fires. In addition, most of the EUCs in aircraft need real-time communication. Reducing the latency and increasing the bandwidth would also be another challenge to building on board data bus systems for aircraft. Fibre optics are regarded as the best candidate, which can solve all those problems above. Fibre optics have been used for many years in the mission systems of aircraft, since the first experimental link was introduced in 1988 [72]. Nowadays, fibres are widely employed in modern aircraft. For example, the Boeing 777 employed an ARINC 636 fibre optical data bus. Details of the ARINC 636 can be found in [73]. The fibre for ARINC 636 is 62.5 μm in diameter and its length is less than 2 km. This data bus provides a 125 Mbit/s data transmission rate and is based on ring topology. Another example is the F-35 developed by Lockheed Martin. According to the report, this aircraft employs over 300 fibres for its data bus, and some channels can support 2 GB/s transmission [74, 75]. The Fly-By-Light (FBL) control system was also recently introduced into aircraft control systems [76]. As compared to the conventional Fly-By-Wire (FBW) control system in which all electronics units are connected via electrical interface, FBL uses the same protocols but provides an optical link and optical connection in aircraft. Introducing optical fibres reduces EMI, increases the bandwidth and decreases the weight. In addition, FBL requires less maintenance. Currently, Boeing 787 and Airbus A380 are using fully

automated FBW control systems while the FBL system is still in the research stage. As FBL offers great advantages over the FBW system, it has the potential to be the future technology for aircraft light control systems [77].

Flexible polymer waveguides are the best candidate to replace silica fibres over a short communication range and can also offer low-cost high-speed links for aircraft. Meanwhile, flexible polymer waveguides have more mechanical advantages, which make them greatly suitable for aircraft because some links need to fit into a very small space. In addition, in the future, when PBCs are co-packaged with on board optical units, flexible polymer waveguides can provide a match in geometry with other on-board polymer waveguides.

1.4 Challenges of flexible polymer waveguides for short-reach links

As mentioned before, even though significant work has been done on flexible polymer waveguides, no systematic studies have been done into flexible polymer waveguides. What are the loss, crosstalk and bandwidth performance of flexible polymer waveguides when they are bent or twisted? How would waveguide modes change when bending is applied? And can any approach overcome those degradations introduced due to the bends and twists? In addition, the performance of multimode polymer waveguides is also highly reliant on the input launch. Different input launch conditions will excite different waveguide modes. Such multimode polymer waveguides can support over a thousand waveguide modes inside, which makes it extremely difficult to carry out waveguide simulation. Quantifying the performance of flexible polymer waveguides and giving guidelines for their successful deployment in real-world systems are the main outcomes of this work. The second challenge is the fundamental study of waveguide mode behaviour. Waveguide modes will experience mode mixing and mode loss when they propagate along the waveguides. Mode mixing means that part of the power of the modes will couple into other waveguide modes for various reasons, and mode loss means that part of the power of the modes is lost, not due to the coupling effect but just through leakage out of the waveguide. Bends, surface roughness, and material scattering are all reasons that

result in mode coupling and loss. Therefore, both simulation and experimental work are needed to explore waveguide mode behaviour.

1.5 Contributions of the dissertation

Flexible polymer waveguides have drawn great interest for use in short-reach high-speed communications. Flexible polymer waveguides have been shown to be much more flexible and lighter than optical fibres. In addition, the flexible polymer waveguide is much more suitable for board integration and interconnects between electronic boards and racks. The cost of flexible polymer waveguides will be much lower than that of silica fibres in the future development of fabrication techniques. Compared to POFs, which are the promising candidate to replace silica fibre for >50 m long communications [43], polymer waveguides concentrate on short-reach communications (1 m to 10 m) and can provide a high bandwidth (>40 Gb/s). To characterise flexible polymer waveguides, a detailed study of flex effects must first be carried out. Therefore, the contributions of this PhD work are given below:

i. The performance of flexible polymer waveguides relies heavily on the input mode excitation. Different input modes will result in a big difference in waveguide performance. The mode excitation effect on the waveguide performance and control of this input condition have been investigated.

ii. Carried out the investigation of the bending and twisting loss performance of the flexible polymer waveguide. Quantified the results on how bends and twists would affect the loss and crosstalk performance.

iii. Designed a new structure of polymer waveguide which is bend-insensitive. Carried out both simulation and experimental work to prove the new concept.

iv. Waveguide mode behaviour studies. Demonstrated how waveguide modes would change during propagation, especially finding out methods to control mode behaviour such as mode mixing and mode loss.

v. Bandwidth studies of flexible polymer waveguides. Due to the highly multimoded nature of flexible polymer waveguides, the bandwidth of a flexible polymer waveguide is mainly limited by the mode dispersion. However, due to the mode mixing effect, bends suppress

modes which could enhance the bandwidth of the waveguide. Experimental work was carried out on the investigation of bandwidth performance when waveguides are under flexure

vi.   Last, demonstrated that a flexible polymer waveguide is robust even under dynamic states. Long-time movement under different speeds and vibration were applied, with continual monitoring of the performance of the waveguide.

A very detailed and systematic investigation into the behaviour of flexible polymer waveguides under flex is presented using all the experiments and simulations carried out above.

1.6 Structure of the dissertation

Each chapter in this dissertation concentrates on a specific topic regarding the development of flexible polymer waveguides. The first chapter illustrates the motivations behind carrying this work and outlines the structure of the whole thesis. The second chapter is mainly a literature review of polymer waveguide materials, coupling methods, and their fabrication. Chapter 3 and Chapter 4 address simulation work and experimental work, respectively. Further studies and discussion are carried out in detail in Chapter 5 and Chapter 6 to support the experimental work in Chapter 4. Finally, Chapter 7 summarises all the work and draws conclusions. Detailed contents of each chapter are given below.

Chapter 1- This chapter reviews the history of polymer waveguide technology and shows the current achievements. The motivation behind developing such a technology is also given. This chapter shows many applications for flexible polymer waveguides including big data centres, autonomous cars, and avionic industries. However, the widespread deployment of flexible polymer waveguides commercially is still challenging. Those challenges are also discussed in this chapter. Finally, the contributions of this work and the structure of this dissertation are listed based on this guideline.

Chapter 2- This chapter is mainly a literature review of polymer waveguide related techniques. This section introduces the material properties involved in this work and analyses their influence. The current fabrication methods are described and evaluated, including photolithography, soft lithography, laser direct writing, and the recent new mosquito injection. Two major coupling schemes, in-plane and out-of-plane couplings are illustrated, and comparisons are made between those coupling

schemes. Lastly, analysis is carried out of the important alignment tolerance as well as propagation loss.

Chapter 3- The methodology is presented in this chapter, including an introduction of mode calculation based on different methods. Based on the equations involved, the mode profile distribution can be determined and simulated. Excess bending losses can then be extracted from the simulation results. The refractive index profile is studied in order to reduce the bending loss, and some combinations of RI profiles are carried out with the resulting performance evaluated. Finally, the simulation indicates a new layout of the waveguide structure which could improve the bending loss performance.

Chapter 4- Detailed studies of flexible polymer waveguides are carried out in this chapter. Much experimental work is done to support this work. In this chapter, the bending and twisting effects are investigated regarding losses and crosstalk. In addition, the dynamic behaviour of flexible polymer waveguides is tested, and the results indicate that robust and stable links could be implemented by polymer waveguides. Lastly, a new layout for a bend-insensitive polymer waveguide is proposed and relevant experimental work is done to prove its better performance.

Chapter 5- This chapter further studies the mode coupling effect in flexible polymer waveguides. Micro-bends and small bending of the curvature are carried out to see the mode coupling behaviours. The main scattering effects of surface roughness scattering are investigated. This scattering mechanism is regarded as the main reason for mode mixing inside the waveguides, and the investigation can help with greater understanding of the behaviour of modes when propagating along the waveguides.

Chapter 6- This chapter concentrates on the bandwidth and high-speed data transmission of the flexible polymer waveguide. Ultra-short pulse measurement is used to estimate the bandwidth of the waveguides. The accuracy of this measurement will also be assessed, and further improvements will be discussed. This chapter also demonstrates high-speed data transmission over a 1 m long waveguide.

Chapter 7- The first part summarises all the work I have conducted during the PhD period, and draws conclusions. The second part discusses future potential work that will be worth carrying out.

Chapter 2 Polymer waveguide materials and fabrication

This chapter presents the fundamental knowledge of polymer waveguide technology. In the first section, the most common polymer materials are given, and details of their properties are discussed. Once we have decided the material, the waveguide fabrication methods are introduced, including photolithography, soft lithography, laser direct writing and the new mosquito injection. In the next section, two main coupling schemes are presented: out-of-plane coupling and in-plane coupling and lists of each specific coupling scheme are compared. The final part concentrates on basic loss analysis, including coupling loss and propagation loss of the polymer waveguide.

2.1 Polymer materials for waveguides

Light is confined in the optical waveguide due to the phenomenon of total internal reflection. A material surrounded by other material which has lower refractive index can result in this total internal reflection at boundary region. Different combinations of core and cladding materials will generate different waveguide properties. For example, a smaller refractive index difference between core and cladding material and a small size of core area will let a waveguide support only one mode, which is called a single-mode waveguide. If it supports more than 1 mode, it is called a multimode waveguide. The performance of waveguides from single mode to multimode is quite different. In the waveguide, each mode is characterised by frequency, effective refractive index, power distribution, electric field, and magnetic field strength [78]. Polymer materials play an important role in affecting all these parameters. Normally, polymer materials which are suitable for integrated optics include polysiloxanes, acrylates, polyimides, polycarbonates, and olefins, and typical processing methods include photoresist patterning and (reactive-ion etching) RIE. Most optical polymers are highly transparent and have a low absorption loss (<0.1 dB/cm) over all key communication wavelength windows such as 850 nm, 1330 nm, and 1550 nm. The scattering loss can also be minimised by using advanced photopatterning methods and by changing the refractive index profile of the polymer material. A graded index profile results in a low scattering loss but will also lose the confinement of optical modes inside the waveguide. Environmental stability is another important consideration when

choosing a material as most polymers cannot withstand daily operation in communication environments. Most polymers will undergo significant changes over time when exposed to heat, light, or oxygen. These changes will have a dramatic effect on the service life and properties of the polymer and can only be prevented or slowed down by the addition of UV stabilizers and antioxidants. Polymers that can stand up to 85°C/85% RH conditions have been developed, and some polymer materials can pass the Bellcore 1209 and 1221 environmental tests [78]. Much research has been done on developing polymer materials, and currently, polymers are highly transparent and reliable, and those environmental requirements no longer limit the lifetime of components.

2.1.1 Material analysis of waveguide performance

i) Polarizability, packing density:

The refractive index of a polymer is related to its packing density and polarizability. Dense packing or large polarizability will result in a higher refractive index. Material polarizability contains three different mechanisms: electric, atomic, and dipole orientation. Details regarding these three types of polarizability can be found in [78]. In liquids and gases, dipole orientation polarization dominates the total polarization, while in the solid phase, electronic polarization dominates the total polarization. In addition, introducing fluorine atoms into a polymer will decrease its refractive index.

ii) Birefringence:

The birefringence, which is the refractive index difference between the TE mode and TM mode, indicates the optical anisotropy of the material. In an isotropic material, birefringence can also be generated by stress and thermal treatment. Some polymers have a large birefringence such as polyimides (<0.24), however, polymers can be molecularly engineered to achieve very low birefringence ($\sim 10^{-6}$).

iii) Temperature dependence:

The great difference between polymers and traditional optical materials is that polymers are temperature dependent. The refractive index of polymers changes rapidly as compared to conventional optical materials, such as glass, when the temperature changes. Normally, a 1 °C increase results in a 10^{-4} decrease in the polymer refractive index.

iv) Humidity dependence

Humidity also changes the refractive index of polymer material, and this is much more severe for single mode waveguides as the core and cladding material may change at different rates. The humidity dependence is due to the counterbalance between moisture absorption and swelling due to the existence of hydrophilic groups. Normally for d-PMMA, humidity dependence is $\sim 10^{-5}/\%RH$ [79].

v) Wavelength dependence:

Wavelength dependence is also known as material dispersion $(dn/d\lambda)$, which is generally to be avoided in most optical systems. Polymers have an order of $10^{-5} \sim 10^{-6}/nm$ dispersion which is similar to SiO_2.

vi) Absorption loss:

Both electronic and vibrational absorptions result in an optical loss for polymers. Polymers normally have a large absorption loss for ultraviolet light due to fundamental excitations of their electrons. The following figure shows the loss spectrum for a typical polymer material: PMMA. Normally, the absorption loss for polymers is around 0.1 to 0.2 dB/cm.
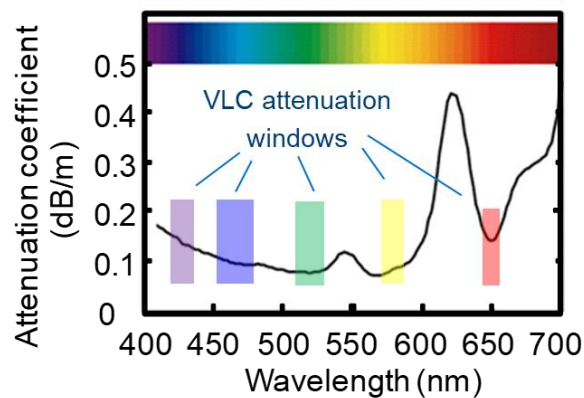
Figure 8 Loss spectrum of PMMA material, several attenuation windows are indicated in visible light range and the unit of attenuation coefficient is dB/m [20].

vii) Scattering loss:

There are a number of factors which can cause scattering loss, including particles, voids, cracks, and bubbles. Extrinsic scattering in polymers comes from unfiltered particles, dust, dissolved bubbles,

and unreacted monomer while intrinsic scattering in polymers originates from density fluctuations and compositional inhomogeneities. For a normal slab waveguide, a loss of 0.03 dB/cm is caused due to the surface roughness of the waveguide sidewall (mainly due to side surface). The RMS roughness of the cladding and core interfaces is around 40 nm. The experimental scattering data can usually be fitted with an empirical law of the form, where A is the contribution of large particle scattering ($\gg \lambda$), B is the inhomogeneity known as Mie scattering ($\sim \lambda$), and D is the contribution from small inhomogeneities known as Rayleigh-like scattering ($\ll \lambda$) [79]:

$$\alpha_{scatter} = A + B/\lambda^2 + D/\lambda^4 \qquad\qquad (2)$$

viii) Polarisation dependent loss:

Polarisation dependent loss (PDL) is referred to as the attenuation difference between two polarisation states. The surface roughness and stress of the material will influence the PDL. The TE loss in the waveguide is higher than the TM loss as the vertical walls normally have higher roughness than the horizontal walls. Applied stress on the material will also cause increased losses of both TE and TM modes [79].

ix) Insertion loss:

Insertion loss is defined as $-10log_{10}(P_{out}/P_{in})$ where P_{out} is the output power and P_{in} is the input power. The total insertion loss achieved in planar polymer waveguides can approach the value of the material absorption loss when fabrication techniques and coupling method are optimised.

x) Return loss:

Return loss is defined as $-10log_{10}(P_{refl}/P_{in})$ where P_{refl} is the reflected power and P_{in} is the input power. Return loss can sometimes result in severe problems as unwanted laser light is coupled back to the transmission system.

xi) Radiation loss and fibre coupling loss:

The radiation loss normally refers bending loss, which is caused due to the small bending curvature of waveguides. Fibre coupling loss can be minimised by matching the mode distribution side with the fibre and planar waveguides. Meanwhile, roughness on the facet of the waveguide

cross-section will also result in a large coupling loss. Index matching gel can be used to minimise this loss.

xii) Mechanical properties:

Polymers can be deposited on rigid and flexible substrates such as glass, quartz, oxidised silicon, and polyimides. By controlling the spin coating speed and polymer/solvent ratio, the film thickness can be fabricated in the range of 100 nm to 100 μm.

xiii) Thermal stability and reliability:

It is better to make sure that polymers do not change their behaviours after long time use under extreme environments. Normally, polymers easily yellow upon thermal aging. However, as mentioned above, polymers now can stand up to 85°C/85% RH conditions and can pass the Bellcore 1209 and 1221.

2.1.2 Siloxane polymer for this work

The wavelength used for short-reach communications is normally around 850 nm and, based on the analysis from the last section, there are some polymers which have been engineered to exhibit low losses and good properties, which are quite suitable for short-reach communications. The following table summarises the common polymers which are now used for short-reach communications in the 850 nm wavelength window. Details of each polymer material can be found in each reference.

Table 2 Common polymer materials used for optical interconnects.

Manufacture	Polymer material	Patterning methods	Propagation loss	Ref
Corning	Acrylate	Photoexposure / wet etch / RIE / laser ablation	0.02 dB/cm @ 840 nm	[80]
Dow Corning	Polysiloxane	Photoexposure / wet etch	0.04 dB/cm @ 850 nm	[20]

General Electric	Polyetherimide	RIE/ laser ablation	0.24 dB/cm @ 830 nm	[81]
NTT	Halogenated acylate	RIE	0.02 dB/cm @ 830 nm	[82]
Optical Crosslinks	Acrylate	Diffusion	0.18 dB/cm @ 800 nm	[83]

Siloxane polymers exhibit excellent optical and mechanical properties. Figure 9 shows that the backbone of siloxane is formed of oxygen and silicon atoms, with no carbon atoms being involved in the backbone, which makes it quite stable at high temperatures and resistant to humidity and oxidation [84]. It also has a very low birefringence ($\sim 10^{-6}$) [84] and low thermo-optic coefficient ($\sim -5 \times 10^{-5}/°C$) [85].
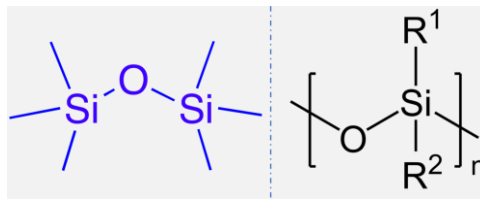
Figure 9 Atomic structure of siloxane polymer, no carbon atoms involved.

The siloxane material involved in this work developed by Dow Corning® is engineered to exhibit suitable mechanical, thermal and optical properties. It can withstand temperatures over 350 °C and can survive the solder reflow and board lamination process without damaging the waveguides. This material also has a low material loss, see its spectrum loss in Figure 10, which is around 0.04 dB/cm at a wavelength of 850 nm. These materials, known as WG-1020 for the core and WG-1023 for the cladding, can be deposited on various substrates such as glass, FR4, silicon, and polyimide. The refractive indices for the core and cladding are around 1.5255 and 1.5104, respectively.
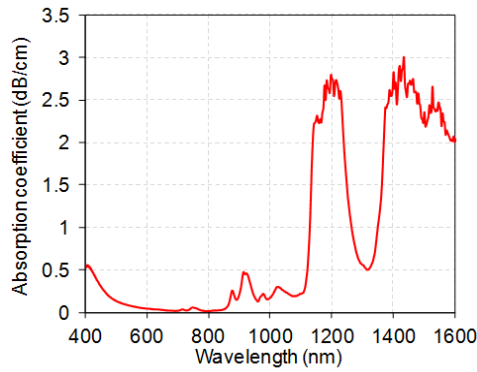
Figure 10 Measured propagation loss of Dow Corning siloxane material within the wavelength range from 400 nm to 1600

nm. Lowest loss value at around 850 nm wavelength window which is less than 0.05 dB/cm [36].

2.1.3 Siloxane based polymer waveguides

The waveguides used in this work were fabricated on 125 μm thick polyimide substrates using conventional photolithography. Details of fabrication methods will be introduced in Section 2.2. They have a cross section of ~$50 \times 50 \ um^2$ and this cross section matches the core diameter of a standard 50 μm multimode fibre (MMF). Such a big cross section offers a relaxed alignment tolerance, and ±10 μm offset will result in only 1 dB loss [20]. There are many other advantages such as suitability for integration on PCBs and offering a high manufacturability. The refractive index difference between the core and cladding materials is ~0.05 at 850 nm, yielding a numerical aperture (NA) of ~0.25 for the waveguides. Such a highly multimode waveguide could support more than several hundred waveguide modes inside. Figure 11 shows that each flexible sample contains an array of 12 waveguides with a pitch of 250 μm, which also matches the standard pitch of multimode fibre ribbons and VCSEL arrays.
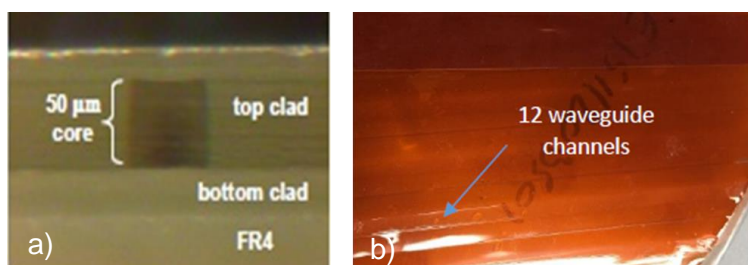
Figure 11 Siloxane polymer waveguide samples, a) cross-section view: squared-shape polymer waveguide core in the

middle of cladding with FR4 substrate and b) top view: 12 parallel waveguides are deposited on polyimide substrate.

24

2.2 Polymer waveguide fabrication

There are various fabrication methods for polymer waveguides, such as photolithography, soft lithography, embossing, laser direct writing, and the new mosquito method. Different fabrication methods offer their different advantages. For example, embossing fabrication provides a low-cost and fast fabrication process as a waveguide mould can be repeatedly used. However, the waveguide quality is not as good as those made by using photolithography. The mosquito injection method is a new method which can provide a graded index profile and circular shape of the waveguide, but it is very different to control its speed and injection depth. Different fabrication methods can then be chosen depending on their different purposes.

2.2.1 Photolithography

A common way to fabricate polymer waveguides is the photolithography method due to its low cost and simple steps. The following figure indicates the steps for fabricating waveguides using this method.
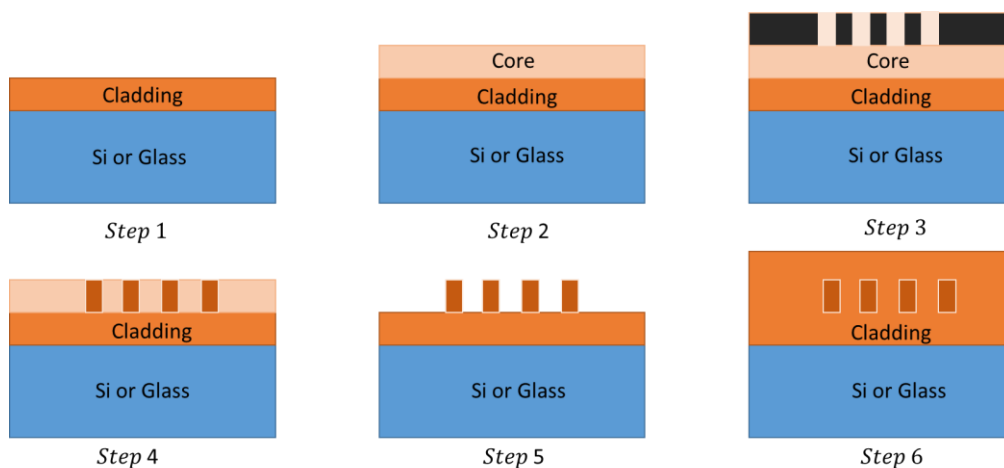
Figure 12 Common polymer waveguide fabrication steps based on photo-lithography method. Waveguide core material is photo-sensitive, and a variety of materials can be chosen as substrate depending on different purposes.

In step 1, a clean substrate is needed, which can be silicon, glass or polyimide, depending on the purpose for which the waveguide will be used. Cladding material is first spin coated on the top surface of the substrate, which is known as bottom cladding. To prevent the light leaking out of the

25

waveguides, the thickness of the bottom cladding is usually made around 30 μm. Then, the sample is baked on a hot plate and the solvent is evaporated. After a few minutes, the bottom cladding is cured and stuck to the substrate.

In step 2, siloxane core material is spin coated on top of the bottom cladding. In this step, speed and time need to be controlled precisely as the core thickness needs to be around 50 μm. After spin coating, another step needs to be taken to check the surface to see if there are any air bubbles or dust on top.

In step 3, a photo mask is put top of the sample with some small supporters at the edges. Those supporters can generate a small gap between the mask and sample, avoiding contact between them. Then, the whole sample is exposed under UV light for around 30 seconds until the waveguide core is cured.

In step 4, the generated sample is shown in this step, in which those areas exposed under UV light are cured and the uncured parts are washed using acetone.

In step 5, after washing, the waveguide channel is almost finished. The whole sample is then baked to evaporate water and unused solvent. The last step is to spin coat with another cladding layer on top to protect the waveguide core and then bake the whole sample again.

Finally, a buried slab polymer waveguide is fabricated and shown in this step. The photolithographic method can only be used for polymer waveguides deposited on flat substrates. Non-flat substrates are normally fabricated using the soft lithography method.

2.2.2 Soft lithography

Soft lithography is a family of techniques that fabricates structures using moulds or stamps. In this method, a master (mould) needs to be fabricated first, which normally is made of polydimethylsiloxane (PDMS). One of the widely used soft lithography methods is called micro-transfer moulding [86, 87]. As shown in Figure 13, the soft lithography method is normally done by casting, embossing and moulding these steps, which is quite convenient and reduces the fabrication costs. The PDMS mould is also reusable if it is carefully peeled off. This method is

capable of fabricating a large-scale waveguide, and the side face of the waveguide also shows an excellent performance [88]. However, the core material resin cannot be fully expelled by the pressure, consequently, it will result in a remnant layer between the waveguide core and cladding, which dramatically degrades the performance of the polymer waveguide.
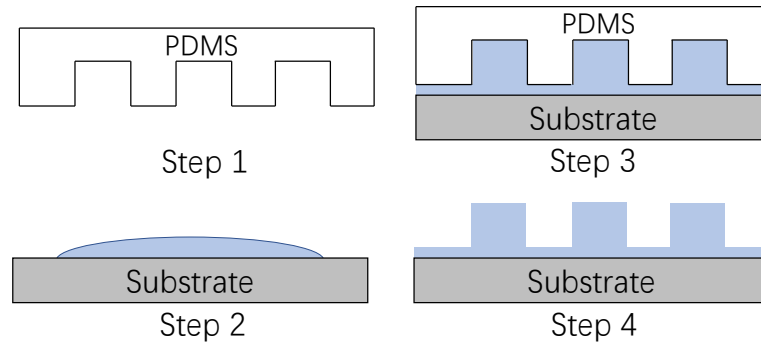
Figure 13 Soft lithography method for fabricating polymer waveguides. A mould is needed to be built first which is made of PDMS material. A remnant layer can be generated as the core material cannot be fully expelled by the mould, which results in a high propagation loss [88].

2.2.3 Laser direct writing

The laser direct writing method is normally used when long polymer waveguides need to be fabricated. [89] shows that the fabrication error can be controlled within 0.15 μm using a 3-axis air-bearing motion platform. A UV writing beam is mounted on an XYZ moveable stage and the focused UV beam is scanned along the core material, as shown in Figure 14. Those materials in the core layer illuminated by focused UV light will be polymerised. Both single mode and multimode polymer waveguides can be built by controlling the beam size. In addition, this fabrication process is a non-contact process and exhibits excellent accuracy [90, 91]. The fabricated multimode polymer waveguides have a propagation loss of ~0.04 dB/cm at 850 nm.

27
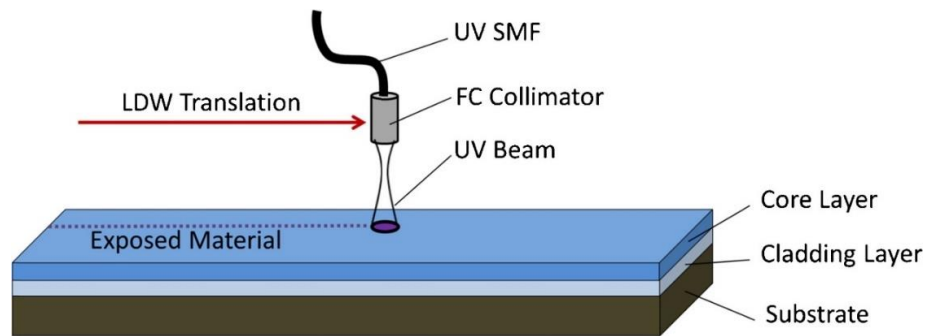
Figure 14 Schematic of laser direct writing process for the fabrication of polymer waveguides. Core material is photo-sensitive and being polymerised by focused UV light. The waveguide core size is controlled by the scanning speed and UV beam size. Both single mode waveguide and multi-mode waveguide can be made using laser direct writing method [89].

2.2.4 Mosquito injection

The mosquito method is a new fabrication method which was proposed by T. Ishigure's group from Keio University [92]. The advantage of this method is that it can provide a circular geometry of polymer waveguide with a graded refractive index profile which perfectly matches the standard 50 μm MMF. The operation steps are shown in Figure 15. First, the cladding layer is coated on the substrate, and next the viscous monomer for the core is dispensed into the cladding layer by inserting the bottom of the needle. The needle is scanned along the horizontal direction and core monomer is injected along the direction. In the final step, both core and cladding are cured under UV exposure and baked at 100 °C. By controlling the scan velocity, different sizes of the waveguide can be obtained ranging from 20 μm to 90 μm. The group also recently reported that a circular core single-mode polymer optical waveguide can be fabricated using this method with a low insertion loss [93]. The researchers believe this mosquito method is a promising method to simply fabricate polymer parallel optical waveguides with a graded index profile for optical PCB applications.
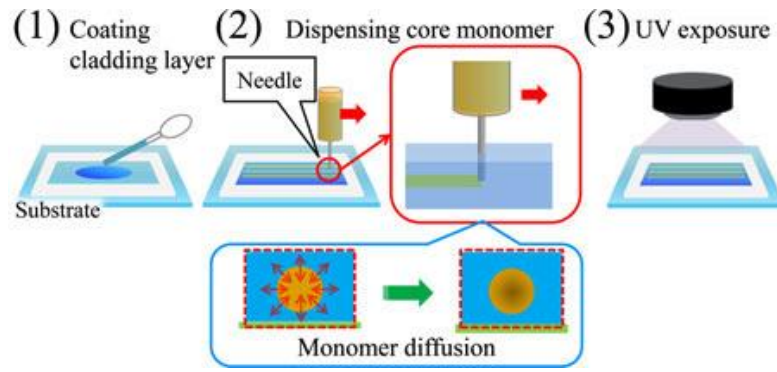
Figure 15 Mosquito method for fabricating circular graded index profile of polymer waveguides. Waveguide core material is injected into cladding via a needle along propagation direction and waveguide core size is controlled by the scanning speed. After core monomer diffusion, a graded index profile can be formed [92].

In addition to these four polymer waveguide fabrication methods, there are also many other methods such as hot embossing, roll-to-roll method, RIE, Doctor blade, etc. There is no strict criterion saying which fabrication method is the best. Researchers can combine those fabrication methods to design waveguides for their own purposes. A summary table of all those fabrication methods and details can be found in [94].

2.3 Waveguide coupling scheme

This section reviews the waveguide coupling methods. It is of great importance to develop cost effective assembly techniques for optical interconnection systems. Good coupling methods can provide low coupling loss as well as robust connection, while poor coupling may generate many more modes and severely degrade the system performance. There are two essential coupling configurations, based on the layout of the active components: out-of-plane coupling, and in-plane coupling. Figure 16 a) shows the out-of-plane coupling scheme. In this configuration, O/E and E/O conversions are placed at the same electrical layer. Laser light goes vertically and is then transferred into horizontal propagation via a 45° reflection mirror. In-plane coupling is quite straight-forward, as shown in Figure 16 b). The active components are placed directly in front of the waveguide end facet. The signals can be transferred and detected directly at the optical layer. There are various approaches to achieving both coupling schemes, and details of each are shown in the following subsections.
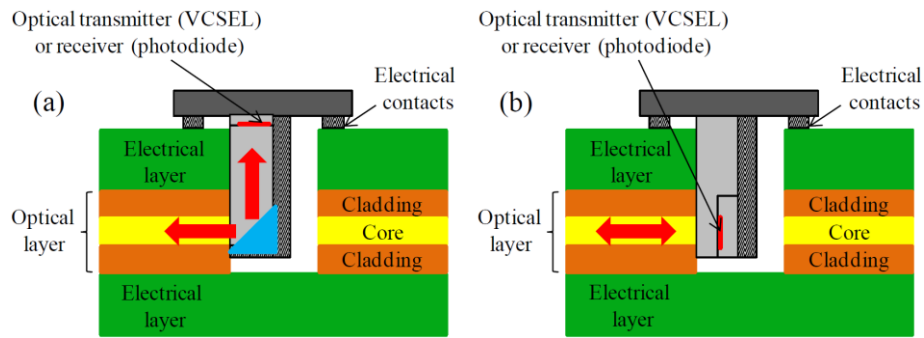
Figure 16 Two essential coupling schemes: a) out-of-plane coupling and b) in-plane coupling. In out-of-plane coupling scheme, the active components are located at the different layer from polymer waveguide while in-plane coupling scheme, the active components are placed at the same layer as polymer waveguide [95].

2.3.1 Out-of-plane coupling

2.3.1.1 Grating coupling

There are two gratings on the top surface of the polymer waveguide. According to the refractive index, and the pitch and depth values of the gratings, specific light with a right angle can couple into the waveguide and become guided modes inside the waveguide. The larger the diffraction efficiency of the grating, the large percentage of light will be coupled into the waveguide. Recent research shows that this coupling method can achieve over 78.8% (1.05 dB Loss) coupling efficiency [96]. However, the drawbacks of this method are obvious. First, one extra step needs to be carried out to generate those precise gratings. Second, the alignment of the laser source to the grating is not relaxed. A specific incident angle is needed and cannot be changed after the grating has been made. The grating structure also damages the integrity of the waveguide core causing additional losses, and sometimes it is very hard to peel off the top cladding to generate those grating couplers.
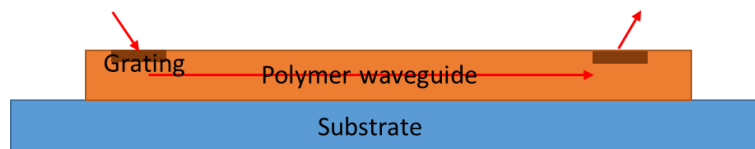
Figure 17 Schematic of grating coupling scheme. Gratings are normally made on the top surface of waveguide core. Laser light illuminates the grating vertically with a specific incident angle and light power can be coupled and transmitted horizontally within the waveguide. Coupling efficiency can go above 78%.

30

2.3.1.2 Prism coupling

In this method, a prism is used to couple the light into the waveguide, as shown in Figure 18. There are many advantages of employing this coupling method, for example, the facet of the core film does not need to be polished precisely and sub-micrometre alignment precision is also not needed. Meanwhile, the diameter of the light beam can be hundreds of times of the thickness of the thin film. The coupling efficiency of this prism coupling method can go as high as 92% [97]. One challenging part would be how to clamp the prism onto the surface of the waveguide. In addition, extra space needs to be reserved for the prisms which makes it unsuitable for system integration.
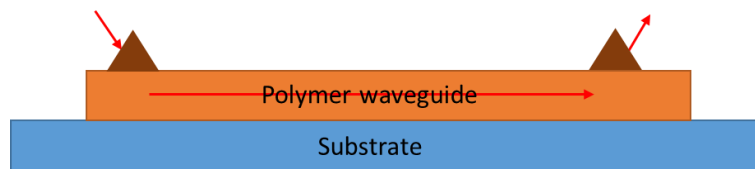
Figure 18 Schematic of the prism coupling scheme. Two prisms are placed on the top surface of waveguide core. When laser light hits the bottom surface of prism, total internal reflection occurs, which can generate an evanescent field at the polymer waveguide core region. Optical power is therefore coupled from outside into waveguide core.

2.3.1.3 45° micro-mirror coupling

In this configuration, a 45° total internal reflection (TIR) micro-mirror is used to guide the laser beam from the vertical direction to the horizontal direction. Normally, this 45° micro-mirror is produced by cutting the polymer waveguide itself to form a 45° tilted surface. There is a simple fabrication method which can create this micro-mirror with a tolerance with $\pm 1°$ and an insertion loss of the uncoated mirror of around 1.6 dB. Some other techniques such as UV-lithography and diamond balding can also be used to cut this 45° tilted surface [98]. The 45° micro-mirror coupling method does not introduce any other passive components, which makes it suitable for system integration. This is also the reason why this method is normally used for achieving out-of-plane coupling schemes. However, the divergence angle of the laser beam needs to be considered as sometimes the gap between the top VCSEL and the mirror is quite big and laser lights will leak out of the waveguide when coupling. In this case, an extra objective lens is normally needed.

31
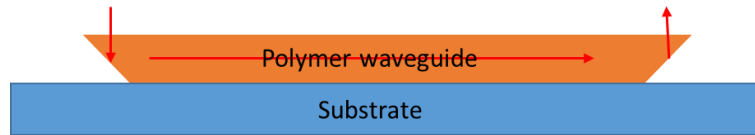
Figure 19 Schematic of a 45° micro-mirror coupling scheme. The vertical direction of incident laser light is changed to horizontal direction via a 45° mirror. The resultant light is then confined within polymer waveguide core.

2.3.1.4 Evanescent coupling

An evanescent wave (field) exists where there is total internal reflection. When the laser beam strikes the medium boundary at an angle which is larger than a critical angle, total internal reflection occurs, resulting in an evanescent field located very close to the surface of a dense medium. As a consequence, when we put two optical waveguides very close together, the evanescent field generated by one waveguide excites a wave in the other waveguide. We could also use this method to guide the light out from the fibre to the waveguide as shown in Figure 20. This method works very well for single mode coupling, and the coupling efficiency can reach up to 100% in theory. As for a highly multimode waveguide, for example the polymer waveguide involved in this work, when putting two waveguides close enough, the coupling behaviour is much like a directional coupler. Light leaking from one waveguide will inject into another waveguide, and the coupling efficiency is around 50% depending on their contact length.
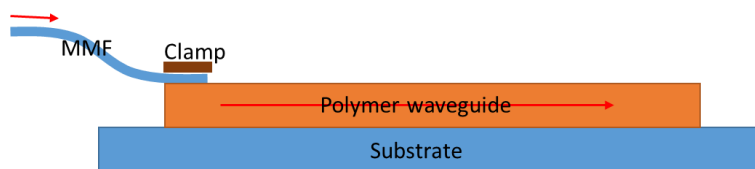
Figure 20 Schematic of evanescent coupling scheme. When total internal reflection occurs, an evanescent filed located close to the surface of dense medium is generated. Then, this evanescent field is confined within waveguide core. For single mode coupling, this coupling efficient can reach 100%.

2.3.1.5 Bent waveguide coupling

The bend waveguide coupling method is a recent new coupling method which allows for bidirectional interruption free coupling [35]. A flexible polymer waveguide on top is bent at a small radius by introducing a defined force. Then the top flexible waveguide contacts the straight

32

waveguide and the power will leak from the top flexible waveguide to the straight one. By controlling the applied force and coupling length, different coupling ratios can be obtained. Currently, the coupling efficiency is around 35%. However, this coupling method does not need extra passive components and does not damage the waveguide core, which makes it perfect for building an optical data bus backplane. As one of the branches, 35% coupling efficiency is enough for the branch unit to detect the signal. If the branch unit is removed, only the top curved waveguide (branch unit) is removed and the main data bus link (straight waveguide) remains intact. There is no degradation of the whole system if unwanted branches are plugged out. However, there are two drawbacks to this coupling method which are that the position of these waveguides needs to be controlled precisely, and the waveguide core is exposed to air without any protection.
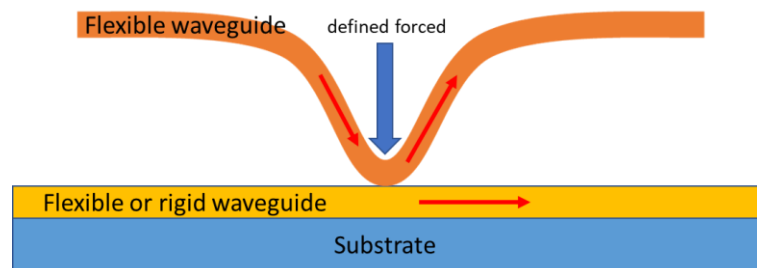
Figure 21 Schematic of bent waveguide coupling scheme. A curved waveguide is generated due to the defined force. Some optical power therefore will leak out of waveguide in this curved waveguide region. Partial leakage power will re-couple back to the straight waveguide. The coupling efficient for this method is currently around 35%.

2.3.2 In-plane coupling

2.3.2.1 End-butt coupling

In this layout configuration, active components (lasers and PDs) are located at the optical layer, see Figure 22. The laser light emitted from the VCSEL directly goes into the polymer waveguide. Due to the divergence of the laser beam, sometimes a lensed fibre is introduced to converge the beam. This often happens when the light is coupled into a single mode waveguide due to its small size. In most cases, the laser light is directly coupled into the waveguide via a very small gap. For the 50 μm waveguide, this coupling method provides a relaxed alignment tolerance. An offset mismatch of 10

μm will cause around 1 dB loss in power. The whole system normally does not need extra beam turning elements such as a micro-mirror and prism, which reduces the system costs and complexity.
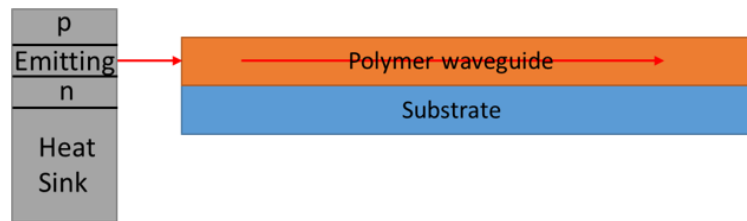
Figure 22 Schematic of end-butt coupling scheme. VCSEL is placed at the same layer as polymer waveguide. The laser light is directly coupled into polymer waveguide, which is quite simple and straightforward.

Current end-butt coupling is made based on two main different configurations. The first is an L-shaped connector as shown in Figure 23 a) [99]. This approach allows the pick-and-place technique that is commonly used in the electronics industries and provides a simple low-cost solution. The drawback of this method is that a hole needs to be drilled and an alignment reference plane needs to be designed precisely. The second one is MT connector-based end-butt coupling [100], see Figure 23 b). This design originates from fibre ribbon connections. However, researchers found that a polymer-based MT connector also works very well. Currently, this MT connector can provide dimension tolerance less than 2.5 μm, and the corresponding loss is less than 0.5 dB for 50 μm squared core waveguides.
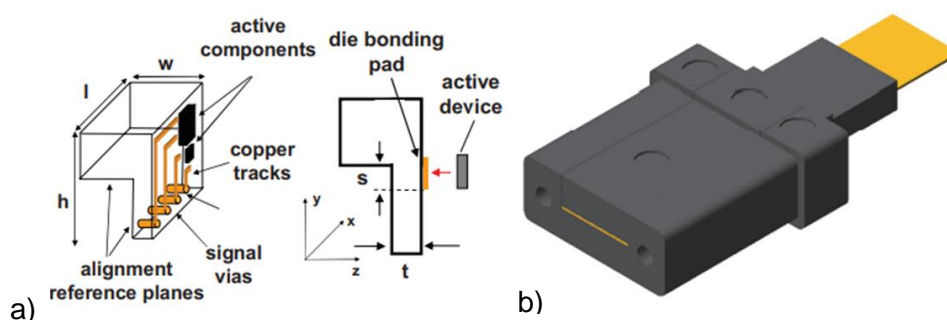
Figure 23 Examples of end-butt coupling elements a) L-shape connector and b) Pluggable polymer MT connector [99, 100].

The following table summarises both the advantages and disadvantages of out-of-plane and in-plane coupling schemes. The comparison is mainly based on achieving complexity and low costs.

Table 3 Comparisons between out-of-plane and in-plane coupling schemes.

Layout	Advantages	Disadvantages
Out-of-plane	- Simple PCB board assembly - Simple electrical connections among OE devices	- Relies on beam turning components - Extra passive components such as micro-lenses - High coupling loss
In-plane	- Simple, straightforward and low cost - Compatibility with pick-and-place assembly process - Low coupling loss - Stable and robust	- Complicated PCB board design - Needs accurate alignment position - Flexibility is worse

2.4 Waveguide loss analysis

2.4.1 Alignment tolerance analysis

The end-butt coupling scheme is used in all the experiments involved in this work, due to its simple and cost-efficient configuration. However, when a laser beam couples into the waveguide, a small part of the beam will be reflected back at the facet boundary due to the mismatch of refractive index, known as Fresnel losses, which can be calculated as below, where n_{co} and n_a are the refractive indices of the waveguide and the medium, respectively:

$$Loss_{FR} = -10 \times log \left(\frac{4n_{co}n_a}{(n_{co}+n_a)^2} \right) \quad in \ (dB) \qquad (3)$$

The waveguide samples involved have a refractive index of around 1.52, and the refractive index of air is 1.0. The Fresnel loss can be calculated based on the equation above, which is around 0.18 dB for each facet boundary and 0.36 dB for both facets. In order to minimise the loss, index matching gel

is normally used on both facets of the waveguide. In this way, the Fresnel losses can be reduced to around 0.

Apart from Fresnel loss, the main coupling loss is caused by the geometry differences in the input fibres and waveguides. For the un-polished facet waveguides, scratches also are one of the reasons for coupling loss. In order to have a straightforward feeling of alignment tolerance for polymer waveguides, the following table summarises the 1 dB coupling loss introduced by a mismatch of position between the input fibres and the waveguide [99]. From the table, if the gap between the input and waveguide is 50 μm, the maximum offset is observed to be around 20 μm.

Table 4 Input and output coupling loss performance analysis of end-butt coupling scheme for VCSEL to waveguide (input side) and waveguide to photodetector (output side) [99].

1 dB coupling loss	Input Side		Output Side	
	d_{gap}		d_{gap}	
	50 μm	100 μm	50 μm	100 μm
X $-$ axis Δx (μm)	+20.2	+15.5	±18.9	±15.2
Y $-$ axis Δy (μm)	+21.0	+17.2	±18.9	±15.2
Rotation R (°)	+7.6	+7.6	±19.6	±8.4
Tilt T (°)	+8.5	+8.5	±19.6	±8.4
Z $-$ axis Δz (μm)	+143		+125	

2.4.2 Propagation loss analysis

There are many reasons that result in power loss when light propagates along the waveguide, such as material absorption, scattering loss, and substrate leakage loss [101]. Material absorption depends on the materials used and can be improved by developing advanced polymer materials. Scattering loss is due to the roughness of the waveguide facet and sidewalls, which will scatter incoming light in different directions at random angles, and it can be reduced by employing better fabrication steps and moulds [102]. Currently, the sidewall roughness of a waveguide is in the range of 40 to 70 nm while the top and bottom walls are somewhat smoother because rougher sidewall is generated due to photo-lithography process while top and bottom walls are generated by spin coating process. As for substrate leakage loss, a small proportion of optical power will exist in the cladding and show an exponential decay in the cladding area. When the bottom cladding thickness is too thin,

some power will go through the cladding and leak into the substrate. An approximation method has been proposed to estimate the substrate leaking loss [101], which shows that leaking loss is around 0.0001 dB/cm for the fundamental mode when the bottom cladding thickness is 2 μm, which is quite small and can be neglected. Also, in real waveguides, the bottom cladding is much thicker than 2 μm.

2.4.3 Bending loss analysis

Bending loss can be divided into two parts: transition loss and radiation loss [103]. When a waveguide starts to bend, the mode distribution profiles are different in the two sections (straight and bent). The optical modes in the straight waveguide section cannot fully couple into the modes in the bent waveguide section and, therefore, result in a loss called transition loss. This loss cannot be simply eliminated but can be reduced. A large curvature of bending is a one effective way to reduce this transition loss. In [104], researchers designed a pair of named mode converter structures which can be used to convert the straight waveguide modes to bent modes with a conversion efficiency of 99.3%. As for radiation loss, bent waveguides only support leaky modes instead of bound modes. For leaky modes, the power in the outer cladding layer does not show an exponential decay. Instead, the energy of the light beam will radiate continuously out of the bent waveguides. [105, 106] show that the power radiation of a specific mode is unique and is determined by the mode order and waveguide parameters. Details of bent mode studies will be introduced in Chapter 3. In conclusion, the total loss referred to as insertion loss occurring inside a waveguide can be expressed as follows, where CL and TL are coupling loss and transition loss, respectively:

$$Loss_{total} = CouplingLoss_{in} + TransitionLoss_{in} + Loss_{radiation} +$$

$$CouplingLoss_{out} + TransitionLoss_{out} + Loss_{propation} \qquad (\ 4\ )$$

Chapter 3 Simulation of waveguide modes and bending effects

This chapter introduces the common methodologies used to calculate optical waveguide mode distributions and contains all the simulation work conducted. Both ray tracing and electromagnetic wave methods can be used to derive mode distributions inside a waveguide channel. Therefore, they can also be used to simulate beam propagation along waveguides. This chapter simulates both straight and bent waveguide modes and analyses their performance. In addition, their performance is evaluated based on the change in RI profiles (SI and GI). Bending loss is regarded as one of the key parameters to evaluate the performance of a flexible waveguide, therefore, an idea for a new waveguide layout which could improve bending loss is simulated and discussed.

3.1 Methodology

Different approaches can be employed to calculate mode distribution inside the waveguides, each of which has its own advantages. This chapter concentrates on three main types of approach: ray tracing analysis, electromagnetic treatment, and simple mathematical calculation. The ray tracing method is a simple and easy method which can simulate beam propagation in different shapes of waveguides, and electromagnetic treatment is an accurate but complex method which is normally used when optical mode behaviours need to be considered. In the last section, a very simple and fast mathematical method is also introduced which is simply based on Snell's Law when tracing the rays, and which can provide a very rough estimation.

3.1.1 Ray tracing method

To simplify the calculation, a parallel planar waveguide is used as a model, see Figure 24. This is a sandwiched structure and the refractive indices for the layers from top to bottom are assumed to be n_3, n_1 and n_2, respectively. The model goes to infinity in the Z and Y directions, and the electromagnetic wave is assumed to propagate along the Z direction.
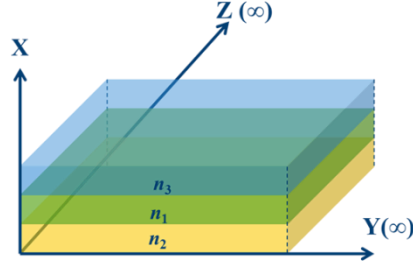
Figure 24 Parallel planar waveguide model, three layers with infinite width (Y) and length (Z).

Firstly, the electric and magnetic fields of a typical electromagnetic wave in the space can be expressed in the following format, where $E_0(r)$ and $H_0(r)$ are the amplitude of the electric and magnetic field at position $\vec{r}$, respectively, ω is the angular frequency, t is the propagating time, $\vec{k}$ is the vector of the wave number, and j is the imaginary unit:

$$E(r,t) = E_0(r)e^{j(\omega t - \vec{k}\vec{r})} \ \& \ H(r,t) = H_0(r)e^{j(\omega t - \vec{k}\vec{r})} \tag{5}$$

Because $\vec{r}$ is the vector in space, it can be decomposed as:

$$\vec{r} = \vec{x} + \vec{y} + \vec{z} \tag{6}$$

Similarly, the wave number vector $\vec{k}$ can also be expressed as follows, where $\vec{l}$ is the unit vector for x, y and z directions:

$$\vec{k} = k_x \vec{l_x} + k_y \vec{l_y} + k_z \vec{l_z} \tag{7}$$

For k in each direction, its scalar equation is expressed as $k = nk_0 = n\frac{2\pi}{\lambda_0}$ where n is the refractive index for each direction. Due to the continuous properties of wave number at the layer boundaries, the wave number in each layer remains the same, which is:

$$k_{1x} = k_{2x} = k_{3x} \tag{8}$$

$$k_{1y} = k_{2y} = k_{3y} \tag{9}$$

$$k_{1z} = k_{2z} = k_{3z} \tag{10}$$

There is no boundary limitation in the Y direction and the wave propagates in the Z direction. Therefore, the wavenumber in the Y direction is 0, which is:

39

$$k_{1y} = k_{2y} = k_{3y} = 0 \qquad (11)$$

Next, the propagation constant which is the wave number in the Z direction is calculated as below. The following figure shows how to calculate the propagation constant (β) and the effective refractive index in the propagation direction. The propagation constant of a sinusoidal electromagnetic wave is a measure of the change undergone by the amplitude and phase of the wave as it propagates in a given direction.:

$$\beta = k_{1z} = k_{2z} = k_{3z} = k_0 n_1 \sin(\theta_1) \qquad (12)$$

$$|\vec{k}| = |\vec{n}|k_0 = |\vec{n}|\frac{2\pi}{\lambda_0} \qquad (13)$$
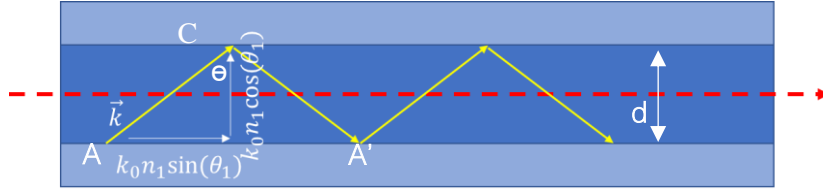
Figure 25 Schematic of parallel planar waveguide model based on ray tracing method. A single ray starts from point A, hits point C and then reflects back to point A', which is defined as one round trip of propagation. d is the thickness of waveguide core and θ is the angle between transmitted light ray and vertical normal line in waveguide core.

The wave number vectors can be rewritten in magnitude format as follows:

$$\left|\overrightarrow{k_3}\right|^2 = k_0^2 n_3^2 = k_{3x}^2 + k_{3y}^2 + k_{3z}^2 = k_{3x}^2 + \beta^2 \ (top \ layer \ 3) \qquad (14)$$

$$\left|\overrightarrow{k_1}\right|^2 = k_0^2 n_1^2 = k_{1x}^2 + k_{1y}^2 + k_{1z}^2 = k_{1x}^2 + \beta^2 \ (core \ layer \ 1) \qquad (15)$$

$$\left|\overrightarrow{k_2}\right|^2 = k_0^2 n_2^2 = k_{2x}^2 + k_{2y}^2 + k_{2z}^2 = k_{2x}^2 + \beta^2 \ (bot \ layer \ 2) \qquad (16)$$

Solving the above equations produces:

$$k_{3x}^2 = k_0^2 n_3^2 - \beta^2 \ (top \ layer \ 3) \qquad (17)$$

$$k_{1x}^2 = k_0^2 n_1^2 - \beta^2 \ (core \ layer \ 1) \qquad (18)$$

$$k_{2x}^2 = k_0^2 n_2^2 - \beta^2 \ (bot \ layer \ 2) \qquad (19)$$

40

First, the mode distribution in the middle core layer can be solved from the definition of the propagation constant:

$$\beta = k_0 n_1 \sin(\theta_1) \leq k_0 n_1 \qquad (20)$$

Thus:

$$k_{1x}^2 = k_0^2 n_1^2 - \beta^2 \geq 0 \qquad (21)$$

and k_{1x} is a real number. Then, k_{1x} can be substituted back into the original electric field (TE mode) equation (5), to produce (similar to the magnetic field for TM mode):

$$E(r,t) = E_0(r)e^{j(\omega t - \vec{k}\vec{r})} = E_0(r)e^{j(\omega t - (k_{1x}x + \beta z))} = E_0(r)e^{-jk_{1x}x}e^{j(\omega t - \beta z)} \qquad (22)$$

The mode field equation shows that the former part $E_0(r)$ determines the magnitude of the electric field, and this magnitude does not decrease along the propagation distance z. The following part $e^{-jk_{1x}x}e^{j(\omega t - \beta z)}$ has unit length and only phase changes when the wave propagates along the z direction.

Second, the mode distribution in both the top and bottom cladding can also be determined. From the equations above, we get:

$$k_{3x}^2 = k_0^2 n_3^2 - \beta^2 \ (top\ layer\ 3) \qquad (23)$$

$$k_{2x}^2 = k_0^2 n_2^2 - \beta^2 \ (bot\ layer\ 2) \qquad (24)$$

In order to confine the modes in the waveguide, β must be:

$$\beta^2 \geq k_0^2 n_3^2 \qquad (25)$$

$$\beta^2 \geq k_0^2 n_2^2 \qquad (26)$$

Thus, k_{3x}^2 and k_{2x}^2 are less than zero. k_{3x} and k_{2x} are not real numbers.

Let:

$$p^2 = -k_{2x}^2 \qquad (27)$$

$$q^2 = -k_{3x}^2 \qquad (28)$$

Because k_{3x} and k_{2x} are not real numbers, $-k_{2x}^2$ and $-k_{3x}^2$ are bigger than 0, which also means that p and q are real numbers. Solving above equations, we get:

$$k_{2x} = \pm jp \qquad\qquad (29)$$

$$k_{3x} = \pm jq \qquad\qquad (30)$$

We obtained the propagation constants of the wave in the top and bottom claddings, respectively. Substituting these two obtained equations into the original electric field equation (5), we finally get the mode distribution in the top and bottom cladding

For the top cladding:

$$E(r,t) = E_0(r)e^{j(\omega t - \vec{k}\vec{r})} = E_0(r)e^{j(\omega t - (k_{3x}x + \beta z))}$$

$$= E_0(r)e^{\pm qx}e^{j(\omega t - \beta z)} \qquad\qquad (31)$$

For the bottom cladding:

$$E(r,t) = E_0(r)e^{j(\omega t - \vec{k}\vec{r})} = E_0(r)e^{j(\omega t - (k_{2x}x + \beta z))}$$

$$= E_0(r)e^{\pm px}e^{j(\omega t - \beta z)} \qquad\qquad (32)$$

The final mode field equations show that it can still be divided into two parts. The $E_0(r)e^{\pm px}$ determines the magnitude of the field, however, it shows an exponential decay trend in the X direction, which means that partial modes are confined in the cladding area when propagating, as shown in Figure 26 [107]. This optical field is called the evanescent field, and the parameters p and q are referred to as attenuation constants. Also, this magnitude does not reduce along the propagation direction (Z direction). The following part $e^{j(\omega t - \beta z)}$ only determines the phase and changes along the Z direction. Because no optical energy leaks out of the cladding, the optical power is confined inside the waveguide. The majority of power is confined in the WG core area and a small part of energy is confined in the cladding.
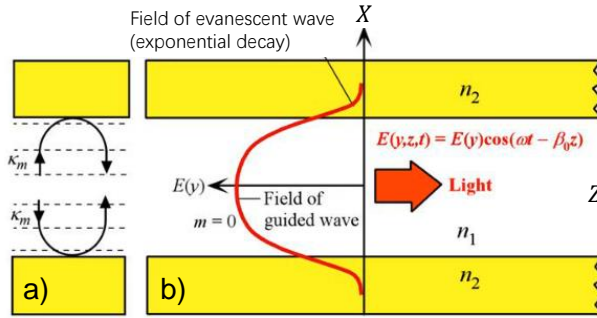
Figure 26 a): Upward and downward travelling waves have equal but opposite wave vector, which could form standing waves between two boundaries. b): electric field of lowest (m=0) mode inside planar waveguide [108].

However, not all the lights with a satisfied propagation constant are able to propagate through the waveguide. The propagated lights also need to satisfy the transverse resonant condition. Figure 25 shows that a light ray starts from A point, will hit C point, and then is reflected back to A' point. The distance that the light ray travels in the X direction is $2d$, where d is the thickness of the waveguide core layer. The total phase change due to this travelling distance can be calculated as:

$$\Delta\varphi = 2dk_x = 2dk_0 n_1 cos\theta_1 \qquad (33)$$
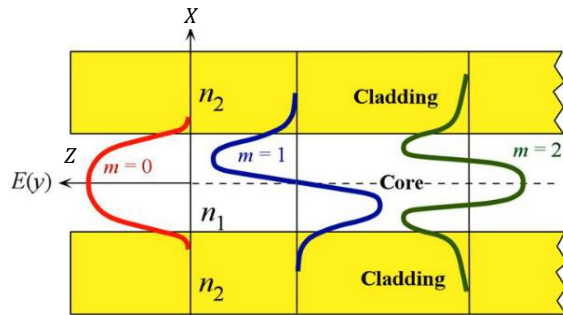
Figure 27 Electric field patterns of first three modes (m = 0, 1, 2) in planar waveguide. Exponential decay profiles are seen from cladding regions [108].

In addition, when total internal reflection (TIR) occurs, the light ray will undergo a small lateral distance called the Goos-Hanchen effect, which will also generate a phase shift, as shown in Figure 28.

43
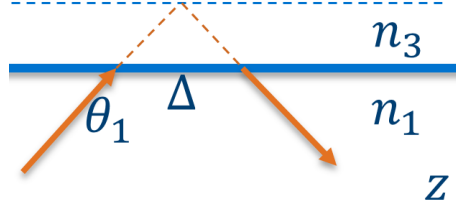
Figure 28 Schematic of Goos-hanchen effect. When total internal reflection occurs, incident light ray will get into cladding in a short range and then is reflected back, which generates a phase shift. Here, $n_3 < n_1$.

In order to simplify the calculation, the phase shift is denoted by $2\Phi_{13}$ and $2\Phi_{12}$, where the subscripts indicate the interface where TIR occurs. The two shifted phases can be calculated according to the Fresnel equation, which is shown below for the TE mode:

$$\Phi_{12}^{TE} = tan^{-1}\left(\frac{\sqrt{sin^2\theta_1 - (n_2/n_1)^2}}{cos(\theta_1)}\right) \tag{34}$$

$$\Phi_{13}^{TE} = tan^{-1}\left(\frac{\sqrt{sin^2\theta_1 - (n_3/n_1)^2}}{cos(\theta_1)}\right) \tag{35}$$

Thus, the total phase change $\Delta\theta$ for transverse direction can be written as:

$$\Delta\theta = 2dk_0n_1cos\theta_1 - 2\Phi_{12} - 2\Phi_{13} \tag{36}$$

Only those light rays which satisfy the transverse resonant condition can propagate along the waveguide, which means that the total phase changes are $2m\pi$, where m is the positive integer numbers. Finally, we could deduce dispersion equation which is:

$$2dk_0n_1cos\theta_1 - 2\Phi_{12} - 2\Phi_{13} = 2m\pi \tag{37}$$

Where the integer number m is called the mode number.

3.1.2 Electromagnetic treatment

Optical light is a small part of the electromagnetic wave spectrum, as shown in Figure 29, and it is a transverse wave comprising oscillating electric and magnetic fields. The resultant vibrating plane is orthogonal to its propagation direction [109].
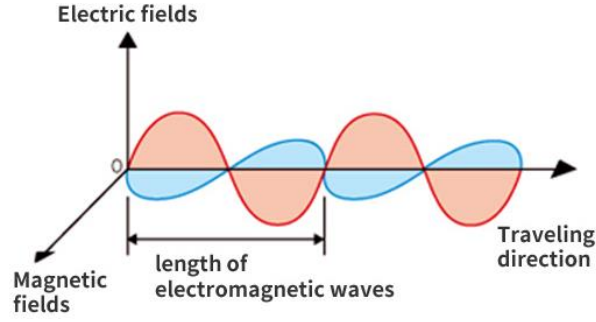
Figure 29 Scheme of electromagnetic wave, its electric field and magnetic field are oscillating and orthogonal with each other and also orthogonal with its propagation direction [109].

Thus, Maxwell equations can be employed to solve mode distributions inside a waveguide by applying boundary conditions. For a dielectric waveguide, the Maxwell equations are denoted as:

$$\nabla \times E = -\frac{\partial B}{\partial t} = -j\omega\mu_0 H \tag{38}$$

$$\nabla \times H = \frac{\partial D}{\partial t} = j\omega\varepsilon_r\varepsilon_0 E \tag{39}$$

$$\nabla \cdot D = \nabla \cdot \varepsilon E = 0 \tag{40}$$

$$\nabla \cdot B = \nabla \cdot H = 0 \tag{41}$$

where D is the electric flux and B is the magnetic flux density, $D = \varepsilon E$ and $B = \mu H$, ε and μ are the permittivity and permeability of the medium, respectively, and E and H are the electric and magnetic field, respectively. As for operators, $\nabla \cdot$ is a divergence operator which is defined as $\nabla \cdot A = \frac{\partial A_x}{\partial x} + \frac{\partial A_y}{\partial y} + \frac{\partial A_z}{\partial z}$; $\nabla \times$ is a curl operator denoted as $\nabla \times A = \left(\frac{\partial A_z}{\partial y} - \frac{\partial A_y}{\partial z}\right)j_x + \left(\frac{\partial A_x}{\partial z} - \frac{\partial A_z}{\partial x}\right)j_y + \left(\frac{\partial A_y}{\partial x} - \frac{\partial A_x}{\partial y}\right)j_z$.

From the first two equations in Maxwell equations, we get:

$$\nabla \times (\nabla \times E) = -j\omega\mu_0 E \times j\omega\varepsilon_r\varepsilon_0 \tag{42}$$

$$\nabla(\nabla \cdot E) - \nabla^2 E = \omega^2\mu_0\varepsilon_r\varepsilon_0 E \tag{43}$$

From the speed of light in a vacuum, $c = 1/\sqrt{\mu_0 \varepsilon_0}$, the speed of light in a dielectric medium with a refractive index n, $v = c/n$, and the relationship between the refractive index and the permittivity $n^2 = \varepsilon_r = \varepsilon/\varepsilon_0$, we can obtain:

$$k^2 = n^2 k_0^2 = \frac{\varepsilon}{\varepsilon_0} \cdot \left(\frac{\omega}{c}\right)^2 = \frac{\varepsilon}{\varepsilon_0} \cdot \omega^2 \mu_0 \varepsilon_0 = \varepsilon \omega^2 \mu_0 \qquad (44)$$

Substituting this equation $n^2 k_0^2 = \varepsilon \omega^2 \mu_0$ back into the electric field $\nabla(\nabla \cdot E) - \nabla^2 E = \omega^2 \mu_0 \varepsilon_r \varepsilon_0 E$ (similar for a magnetic field), the Helmholtz equations are therefore obtained:

$$\nabla^2 E + n^2 k_0^2 E = 0 \qquad (45)$$

$$\nabla^2 H + n^2 k_0^2 H = 0 \qquad (46)$$

TE mode consists only of the field components E_y, H_x and H_z while the TM mode only contains the H_y, E_x and E_z fields. To simplify the calculation, only the E_y field of the TE mode is calculated here, and the rest of the fields can be calculated using the same steps. In order to solve this second order differential equation, let us first assume it that has the following general solution format:

$$E_y = E_{y_0} e^{j(\omega t - \beta z)} \qquad (47)$$

Substituting the equation above into Helmholtz equations, we get:

$$\frac{\partial^2 E_y}{\partial x^2} + (n^2 k_0^2 - \beta^2) E_y = 0 \qquad (48)$$

This is the second order homogeneous equation, and the solutions are dependent on the value of the term $(n^2 k_0^2 - \beta^2)$. For $n^2 k_0^2 - \beta^2 > 0$, the solution is in sinusoidal format and for $n^2 k_0^2 - \beta^2 < 0$, the solution shows an exponential decay format.

For a guided wave in the core layer, we have:

$$n_2 k_0 < \beta < n_1 k_0 \qquad (49)$$

$$n_3 k_0 < \beta < n_1 k_0 \qquad (50)$$

Based on the inequality equations above, we can get general solutions of this second order homogeneous equation for each layer, which are shown below:

$$E_{y3}(x) = A'e^{qx} + Ae^{-qx} \qquad\qquad (51)$$

$$E_{y1}(x) = Fe^{jhx} + F'e^{-jhx} \qquad\qquad (52)$$

$$E_{y2}(x) = Ce^{px} + C'e^{-px} \qquad\qquad (53)$$

By applying boundary conditions: 1) the thickness of the cladding layers goes to infinity, and 2) the tangent vector of E_y should be continuous, we could simplify above equations:

$$E_y(x) = \begin{cases} Ae^{-qx} & x > 0 \\ A cos(hx) + B sin(hx) & -d \le x \le 0 \\ [A cos(hd) - B sin(hd)]e^{p(x+d)} & x < -d \end{cases} \qquad (54)$$

where $q = \sqrt{\beta^2 - n_3^2 k_0^2}$, $p = \sqrt{\beta^2 - n_2^2 k_0^2}$ and $h = \sqrt{n_1^2 k_0^2 - \beta^2}$. Parameters A and B are real numbers determined by the power distribution of the incident light. The dispersion equation can be deduced according to another boundary condition (3) $\partial E_y / \partial x\ (H_z)$, continuous at $x = -d$. Due to the periodicity of tangent function, a set of solutions can be found corresponding to the different orders of waveguide modes.

$$tan(hd) = \frac{h(p+q)}{h^2 - pq} \qquad\qquad (55)$$

3.1.3 Simple mathematical tracing method

This method is also one of the ray tracing methods, which means that the calculation is only based on the laws of geometric optics. It is the simplest and the most straightforward method to simulate light propagation inside the waveguide [110]. However, based on the previous analysis, we know that only some certain light can propagate along the waveguide. This simple mathematic tracing method allows all the light that satisfies the TIR criteria to transmit inside the waveguide. This method works very well when there is no mode coupling, and mode loss is involved in the simulation, especially since the large size of polymer waveguides contain over a thousand modes. This tracing method is the best way that is both accurate and time saving, but it cannot simulate mode behaviours. The details of this method are shown below.

A typical slab waveguide is formed of a square channel with a large refractive index, surrounded by cladding material with lower refractive index. Once the rays are confined (satisfying TIR) inside

47

the waveguide, they will continue to be confined unless TIR is no longer satisfied. A laser beam is regarded as many single rays with different incident angles and powers. There is a relationship between the initial incident angle θ_0 and its refractive angle θ_r, and the equation is given by Snell's Law:

$$n_{air} \, sin(\theta_0) = \theta_{core} sin\,(\theta_i) \qquad\qquad (56)$$
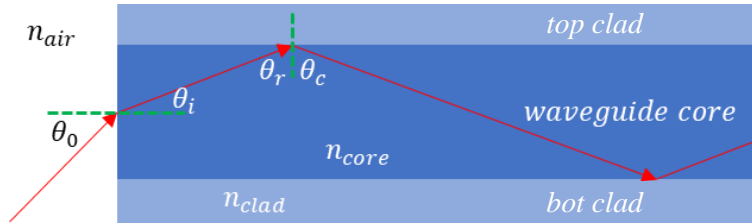
Figure 30 Illustration of total internal reflection inside the planar waveguide. θ_0 is the laser light incident angle, θ_i is the

refraction angle, θ_r is the complement angle of θ_i which is $90°$ - θ_i and θ_c is the reflection angle which is equal to θ_r.

Based on this equation, any input beams can be divided into enormous single rays and their corresponding refractive angles can also be determined. Therefore, a linear equation can be used to describe each single ray:

$$y_i = b \cdot tan(\theta) + c \qquad\qquad (57)$$

where c is a parameter to be determined which determines the position of this ray, θ determines the angle of the ray, and b is another parameter that determines the power of the ray. By generating an array in MATLAB, any input launch is therefore simulated. Next, based on the parameters of the waveguide such as width and thickness, we can generate another two lines, where d is the thickness of the waveguide:

$$y = d \; (top \; boundary) \qquad\qquad (58)$$

$$y = 0 \; (bot \; boundary) \qquad\qquad (59)$$

Combined with all three equations above, the roots can be solved. Those roots represent the hitting points of the rays. Next, the reflected rays start from the same hitting position, but have different angle vectors. According to the Fresnel equation, the value of angle remains the same $\theta_r =$

θ_c but the direction changes. The following equation can then be used to determine the new reflected rays:

$$y'_r = b \cdot tan(-\theta) + c' \qquad\qquad (\text{ }60\text{ })$$

By repeating the above steps above until the rays reach the end of the waveguide, all the trajectories of the light rays can be traced by this method.

3.2 Simulation of waveguide modes

3.2.1 Optical waveguide mode

Both ray tracing and wave equation analysis as mentioned in Section 3.1 are based on a model of the parallel planar waveguide. This model assumes that one direction of the waveguide goes to infinity. However, a real waveguide is normally rectangular, and the optical modes are confined in two directions. In 1969, Enrique Marcatili proposed a new method which can be used to analyse how light propagates through a rectangular dielectric optical waveguide [111, 112]. The basic idea of this approach is that the four corner quadrants are neglected, and the rest of the structure can be treated as two parallel waveguides. Therefore, the previous analysis methods for a parallel waveguide can be used. However, as shown in Figure 31[113], when we calculate the 2nd parallel waveguide, the core refractive index is replaced by the effective refractive index of the modes in the 1st parallel waveguide.
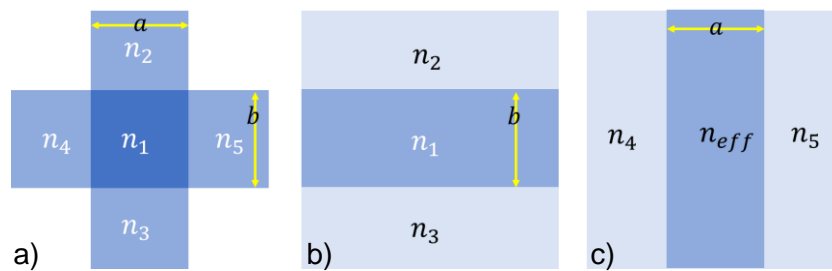
Figure 31 a) Configuration of the rectangular dielectric waveguide, b) equivalent confinement of a 1D guide in the y

direction and c) equivalent 1D guide with confinement in the x direction

Based on Marcatili's method, both mode distribution profiles and their mode simulation can be calculated as shown in Figure 32.
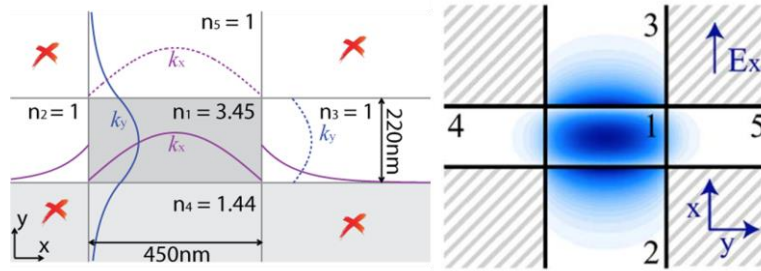
Figure 32 Sketch of fundamental mode profile of a rectangular waveguide and its TE-like mode simulation [114]

There are also some other methods which can be used to calculate slab waveguide modes such as the film mode matching (FMM) method, variational mode expansion method (VMEM), and the finite element method (FEM) [115-118]. Some methods are quite complex but accurate. In the real world, when optical modes are calculated inside the waveguides, the Maxwell equations do not need to be solved by hand. There is commercial software which can be used to simulate those waveguide modes. However, what the software does is help solve those equations. They are essentially the same thing.

The following simulation work of optical waveguide modes was based on the commercially available software, OptiBPM. As shown in Figure 33, the cladding size for this rectangular waveguide profile is $100 \times 100 \ \mu m^2$ and the core cross-section area is $50 \times 50 \ \mu m^2$. The refractive indices of the core and cladding materials are indicated on the plot.
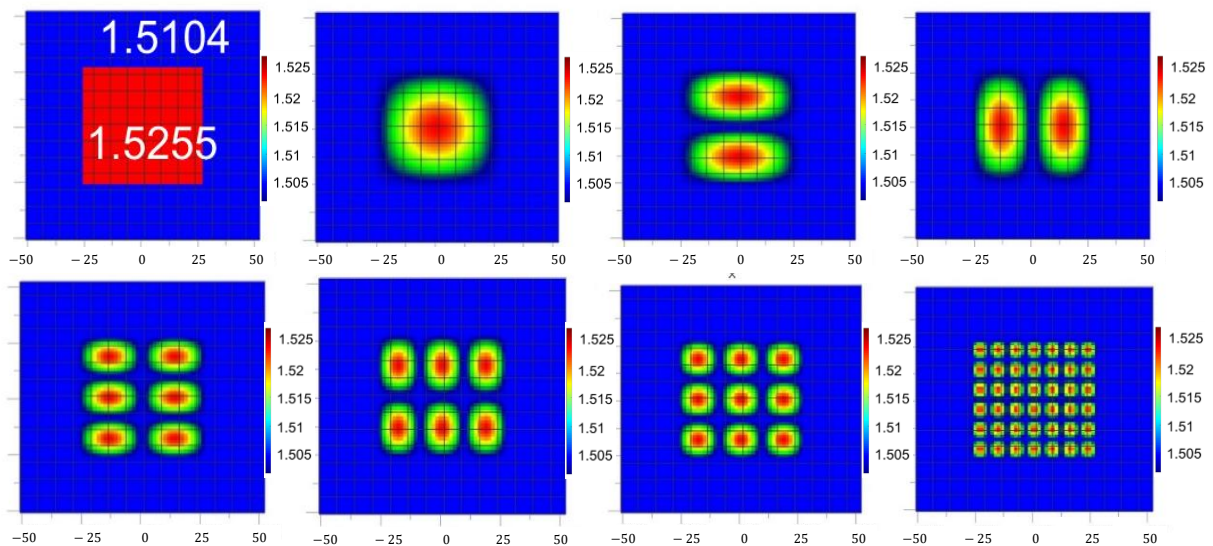
Figure 33 Simulation of optical modes for $50 \times 50 \ \mu m^2$ waveguides under 850 nm wavelength based on OptiBPM

software. Refractive index values for core and cladding are set to be 1.5255 and 1.5104, respectively, which are close to the

values measured from the real waveguide samples.

50

The simulation results indicated an agreement with the theoretical waveguide functions. For the fundamental mode, the peak value was located at the centre. Also, the mode order number could be easily read from the figure, in the number of valleys in each direction. The last plot shows a very high order mode. Its power distribution shows that it is roughly uniform. One conclusion which could be drawn is that the lower the mode, the concentrated the power. During the simulation, when you multiply any two modes in the electric field, the sum is 0, which indicates another conclusion that any of two optical modes inside the waveguide are orthogonal to each other. The power of one mode could not transfer to another mode if no disturbance occurs.

3.2.2 Bent optical waveguide mode

Much research has been carried out on exploring bent mode studies [119-126]. Calculations of bent waveguide modes are quite complex. In order to make the results clearer to understand, some assumptions are made to simplify the calculations. Currently, there are some new methods, the Finite-element based perfectly matched layer (FE-PML) method [127] and the transformation optics method [128], which can be used to calculate the bending waveguide modes. Details of these can be found in those papers. This section concentrates only on the fundamental equations of deriving bent mode functions.

First, for a bent rectangular waveguide in a cylindrical coordinate system (r, y, θ), the electric E and magnetic fields H which propagate along the azimuthal direction can be described as follows according to [123]:

$$E(r, \theta, y, t) = E_r^0(r)E_\theta^0(r)E_y^0(r)e^{j(\omega t - \gamma R\theta)} \tag{61}$$

$$H(r, \theta, y, t) = H_r^0(r)H_\theta^0(r)H_y^0(r)e^{j(\omega t - \gamma R\theta)} \tag{62}$$

where $\gamma = \beta - j\alpha$, β is the phase constant, α is the attenuation constant, γ is the propagation constant of the bend mode, and ω is the angular frequency corresponding to vacuum wavelength λ. By substituting the above two equations into the Maxwell equations and calculating a in polar coordinate system, the Bessel equation can be obtained below, which are used to describe the electromagnetic field. Details of the calculation are in [129]:

$$\frac{\partial^2 \phi}{\partial r^2} + \frac{1}{r}\frac{\partial \phi}{\partial r} + \left(n^2 k^2 - \frac{\gamma^2 R^2}{r^2}\right)\phi = 0 \qquad (63)$$

The solution for the Bessel equation is the combination of the Bessel functions. In this situation, [129] has already calculated the solution which is shown below:

$$\phi(r) = \begin{cases} A_s J_v(n_s kr) & 0 \leq r \leq R^- \\ A_f J_v(n_f kr) + B_f Y_v(n_f kr) & R^- \leq r \leq R^+ \\ A_c H_v^{(2)}(n_c kr) & R^+ \leq r \end{cases} \qquad (64)$$

where $J_v(x)$ is the first kind of Bessel function, Y_v is the second kind of Bessel function, and $H_v^{(2)}(x)$ is the second kind of Hankel function, which is equal to $J_v(n_c kr)$+j$Y_v(n_c kr)$. A_s, A_f, B_f and A_c are unknown parameters so far and can be determined by the boundary conditions. The following figure shows the fundamental mode bending at different curvatures from [130], along with the bent mode distribution and how well that waveguide confines the bent mode at different bending radii. Clearly, part of the distribution leaks out of the waveguide continuously, causing radiation loss.
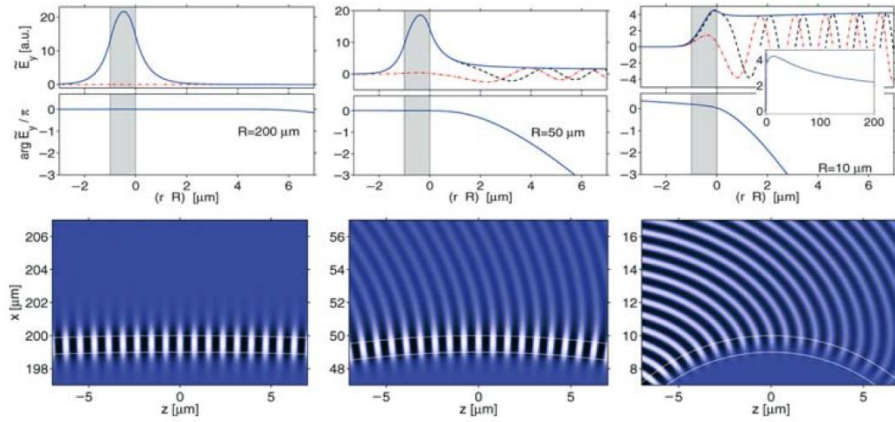
Figure 34 TE_0 bent mode profiles and snapshots of propagating bending modes. Waveguide structure is set to be bent at 200 μm, 50 μm and 10 μm from left to right, respectively [123].

The above simulation is based on a single mode waveguide. In order to observe the distribution of higher order bent modes in multimode waveguides, software named wgms3d is used which is based on a free full-vectorial waveguide mode solver [131]. The waveguide core cross-section was set to $50 \times 50 \ \mu m^2$ and was surrounded by cladding with a lower refractive index. In order to get rid of the boundary influence, a perfect matching layer (PML) was set as indicated by the dashed black line.

PML had a large attenuation coefficient and the optical field decayed significantly after passing through this PML.

From the simulation results in Figure 35, the first row shows the waveguide modes in the straight condition ($R = \infty$), where all the modes are symmetric. The second row is the bent modes when bending at 20 cm. This is a large bending radius, and the centre of all waveguide modes tends to shift towards the outer layer of the waveguide. The third row is much more obvious when bending at 10 cm. The power for all modes is much more concentrated in the outer area of the waveguide. A real waveguide experiences power leakage if the confinement between the core and cladding is not strong. In addition, the area of each mode also became smaller, which indicates that bends have an effect of suppressing optical modes. This would be very useful as some modes can be suppressed or filtered out after passing through carefully designed waveguide bend structures.
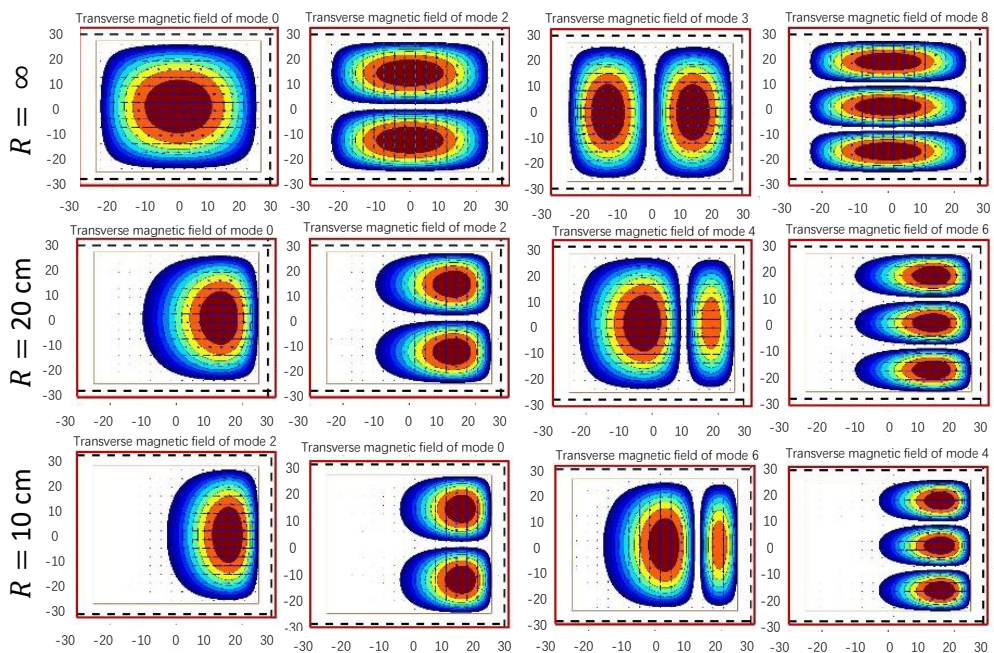
Figure 35 Example of some bending modes in multimode waveguides at different bending curvatures, R = 10 cm and R = 20 cm. Waveguide modes in straight waveguide R = ∞ are given for comparison as well.

3.3 Simulation of effects of bending on waveguide performance

3.3.1 Leaking and bending loss in step-index and graded-index profiles

Waveguides can be categorised into two classes based on the refractive index profile of the waveguide core: step-index and graded index, as shown in Figure 36. A step-index waveguide has a uniformly raised refractive index profile while the graded-index waveguide has a continuously raised refractive index profile.
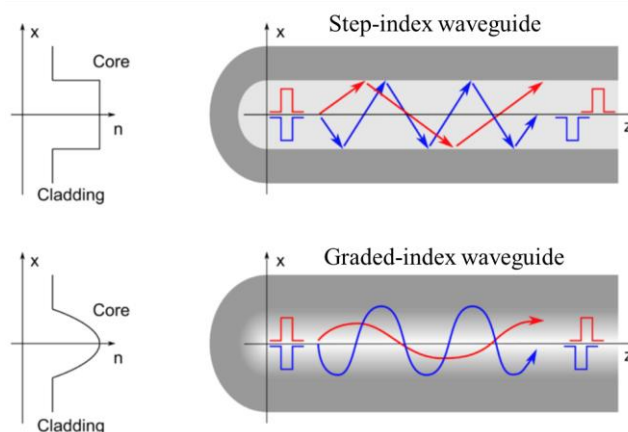
Figure 36 Refractive index profile and path trajectories of step-index and graded-index waveguides. Dispersion generated in GI waveguide is smaller than SI waveguide due to the faster transmission speed of the rays with bigger incident angle [132].

The main difference of these two types of waveguides is the ability to retain the pulse shape. The figure above shows that the blue and red pulses have a big offset in the step waveguide as compared to the graded waveguide, which means that the pulse is more broadening after propagating a long distance in a step-index waveguide than in a graded-index waveguide. Another difference is that from the ray paths, for the step-index waveguide, light rays hit the core-cladding boundary and are then reflected, while in graded-index waveguide, there is no clear core-cladding boundary. This phenomenon indicates that waveguide will have a smaller propagation loss in a graded-index profile as rays do not hit the rough boundaries.

However, how will the refractive index profiles affect the performance of waveguides, especially for flexible waveguides? In order to quantify this question, a simulation of bending loss performance

was carried out based on two different refractive index profiles: step-index profile and graded-index profile. The simulation software was a commercially available software named ZEMAX, based on the ray tracing method. The whole system setup is shown in Figure 37.
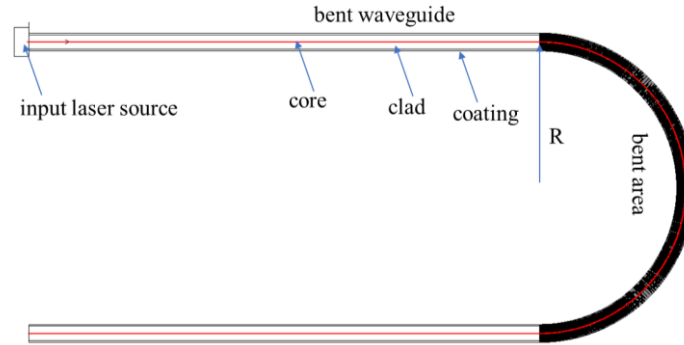
Figure 37 Simulation of bending loss performance system setup using ZEMAX software. The waveguide is formed of two straight sections and one bent section. Waveguide core cross-section is $50 \times 50 \ \mu m^2$ surrounded by $200 \times 200 \ \mu m^2$ cladding and a polyimide material layer is coated outside surface of cladding layer.

At the input side, we can set different types of input launch conditions. Details of the different launch conditions will be introduced in Section 4.2. The waveguide had a core size of $50 \times 50 \ \mu m^2$ which is the same as a real polymer waveguide. The thickness of the cladding was set to be $200 \ \mu m$, surrounded by a polyimide material coating with a refractive index of 1.72. The core profile was set to be step-index or graded index, and the cladding material was set to have a refractive index of 1.5104. The whole waveguide was bent at $180°$ with a variable bending radius R. In each simulation, the bending radius was changed, and the related input and output powers were recorded. Thus, the bending loss could be obtained using the following equation:

$$Bending\ loss = 10\ log\left(\frac{P_{in}}{P_{out}}\right) \quad in\ (dB) \qquad (65)$$

Figure 38 shows the refractive index distribution used in the simulation for the step-index and graded-index waveguides. For the step-index waveguide, the core material distribution was uniform with a value of 1.5255, and for the graded-index waveguide, the refractive index distribution was parabolic in the x-direction and showed a linear decay in the y-direction. The largest RI area located in the bottom central area of the waveguide had the same value of 1.5255. The reason for choosing

this graded index profile was that it shows a similar RI profile as the real waveguide sample, details of which will be explained in Section 4.1.
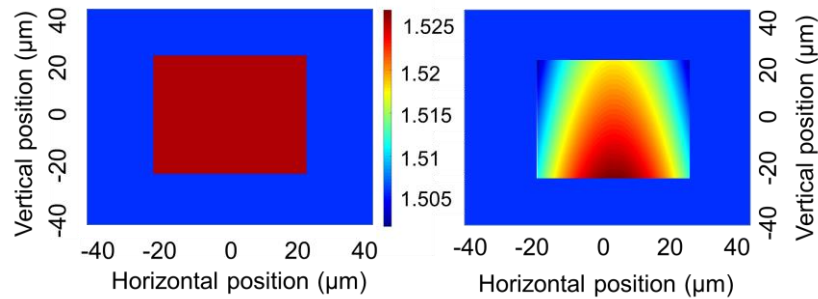
Figure 38 Refractive index profiles used in simulation for SI and GI waveguides. SI waveguide: with core RI value of 1.5255. GI waveguide: with maximum core RI value of 1.5255 and a parabolic-like RI pattern. Cladding values for both SI and GI waveguide are the same with the constant value of 1.5104.

The following Figure 39 shows the results of bending loss under different launch conditions for a step-index waveguide (filled markers) and a graded-index waveguide (unfilled markers). Details of all launch conditions and their distributions are given and discussed in Section 4.2. More restricted launch will result in much better loss performance in short. First, under a 4 μm SMF launch (restricted launch), the bending losses were almost 0 dB when the bending radius was greater than 7 mm for both SI and GI waveguides. Then they showed an exponential increase when the bending radius was reduced to 3 mm. The steepness of the curve for the SI waveguide was much bigger than the GI waveguide. The bending loss performance under 50 μm MMF input indicated similar behaviour. However, there was still around 0.5 dB loss when the bending radius was greater than 10 mm. Details of the bending loss for each bending radius and each launch condition can be found in the figure. Two conclusions could be drawn from this simulation. First, a step-index waveguide will result a much higher bending loss compared to a graded-index waveguide, and second, the bending loss performance of a waveguide is highly reliant on the input launch conditions. A restricted launch condition will result in much smaller losses.
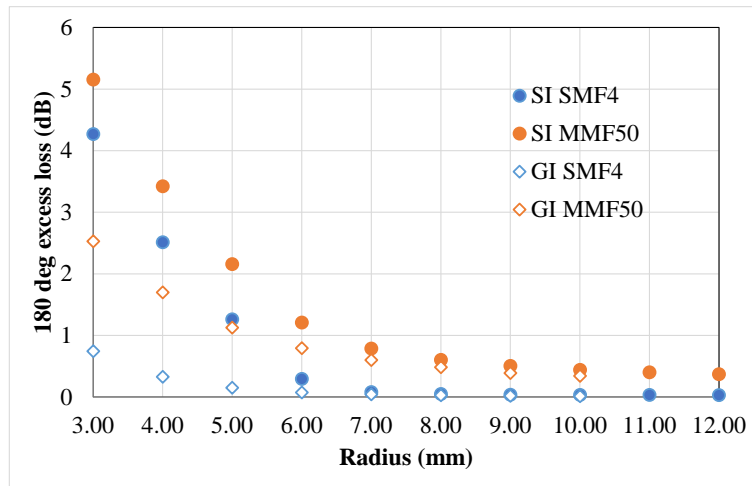
Figure 39 Simulated bending loss performance of step-index (SI) and graded-index (GI) waveguides under different launch conditions. Filled are SI waveguide simulation results and unfilled are GI waveguide simulation results. Bending degree is set to be 180° in both cases.

3.3.2 Effects of graded-index profiles

The last section showed that graded-index profiles have many advantages compared to step-index profiles. In this section, based on a real refractive index profile, we will explore how different refractive index patterns influence the waveguide performance. The following figure shows the structure chart of the graded index profile mentioned in the last section. The value change of RI is a linear decay in the x direction and parabolic in the y-direction.
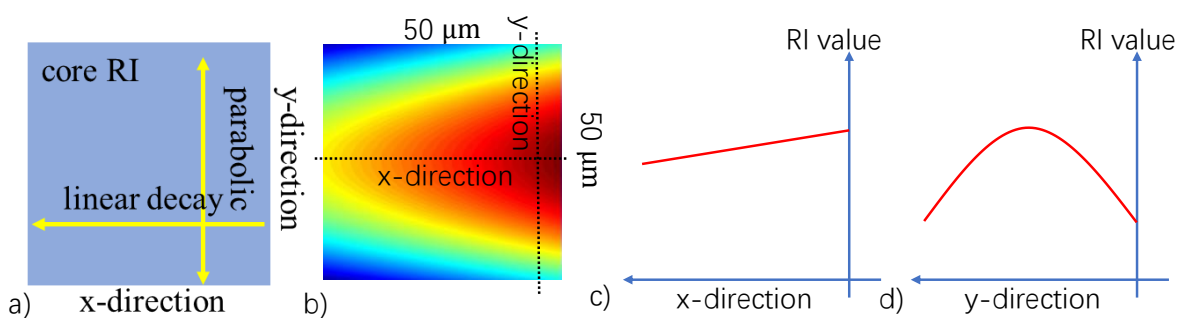
Figure 40 a) Schematic structure of graded-index profile distribution. b) generated graded-index RI profile for waveguide core in simulation. c) linear decrease of RI value in x-direction, cut from horizontal dash line in b. d) parabolic shape of RI value in y-direction, cut from vertical dash line in b.

First, the value change of RI in the x direction varies linearly with a step value of 0.002 and RI in y direction remains the same. The resultant RI patterns are shown in Figure 41. The highest refractive index point at the right middle point remains the same while the value of the left middle point decreases by 0.002 each time. The RI of the cladding material is set to remain constant.
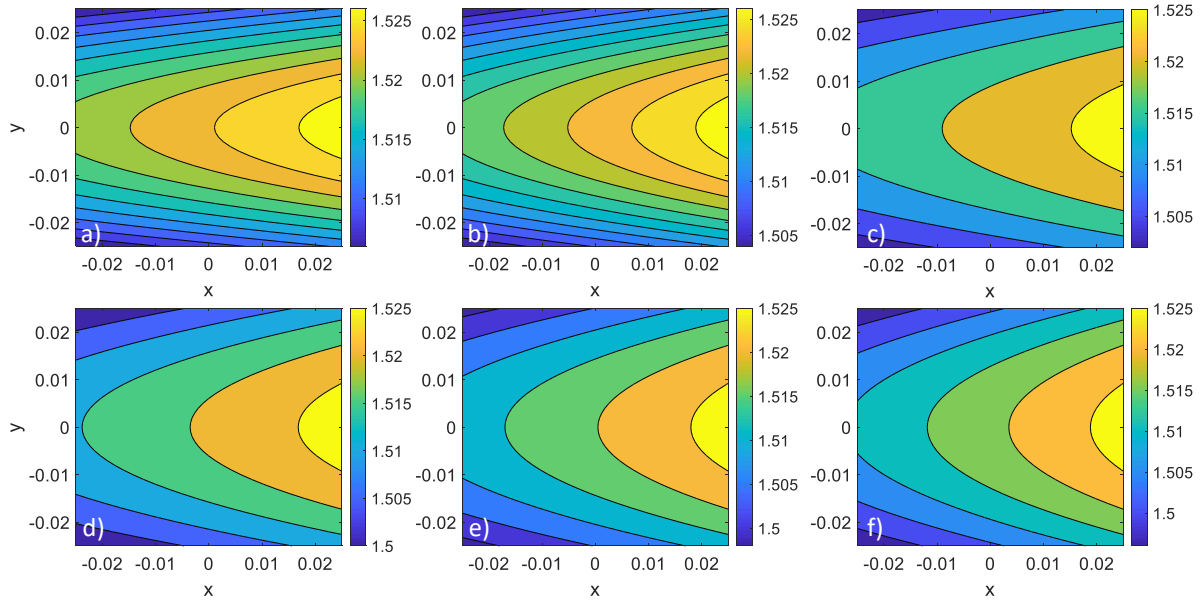
Figure 41 Different refractive index profiles of the waveguide core, RI changes in x direction linearly with a step value of 0.002. These six patterns are employed as waveguide RI profile during the simulation.

During the simulation, 50 μm MMF was employed as the input launch, and the resulting bending losses from different RI profiles are shown in Figure 42. The figure shows that profiles that change in the x direction have an obvious effect on the bending loss performance of the waveguide. Linear decay of RI in the x direction causes a linear upward shift of bending loss curves, which means more losses. This is reasonable as a smaller RI difference (core and cladding) will have less ability to confine the light. However, the curve shape remains similar for different RI profiles. All the curves show a similar slope. The RI profile changes in the x direction do not change the waveguide bending performance over small bends as compared to large bends.
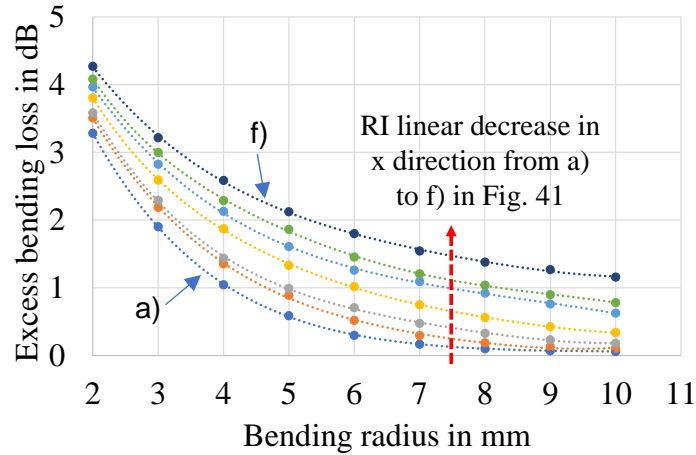
Figure 42 Simulated bending loss performance of waveguides for different RI profiles under 50 μm MMF, RI changes in a linear decay in the x-direction. 'pattern a' results in the best loss performance while 'pattern f' results in the worst.

Next, the RI profile in x direction was set to remain fixed, and the parabolic shape was changed from a small curvature (sharp) to a large curvature (flat). The resulting patterns are shown in Figure 43. Pattern 1 has the smallest radius of curvature for the parabolic curve while pattern 5 is flat in the y direction. The simulation was done by using each of the RI pattern profiles below.
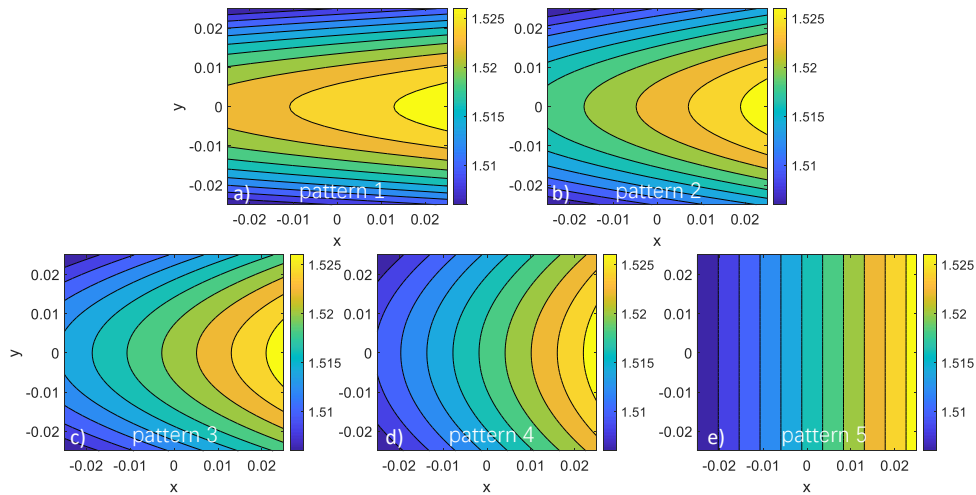
Figure 43 Different refractive index profiles of waveguide core, with parabolic shape changes in y-direction.

All the system parameters were the same as the previous simulation except for the RI profiles. The resulting bending loss curves are given in Figure 44. The resulting curves are quite different to the previous ones. RI changes in the y direction change the ability of the waveguide to confine power at different bending radii. The pattern 5 RI profile resultant in the lowest bending loss while

pattern 1 showed the worst performance of the waveguide. Pattern 5 had the highest average refractive index difference between the core and cladding boundary while pattern 1 had the lowest. During the simulation, the scattering effect is not considered, thus, for an ideal waveguide (0 surface roughness), the simulation indicated that the RI difference is much more important than the RI distribution for affecting the bending loss performance of the waveguide. In the meantime, the simulation also indicated that using the graded-index profile for the polymer waveguide is probably not the best way to reduce bending losses alone.
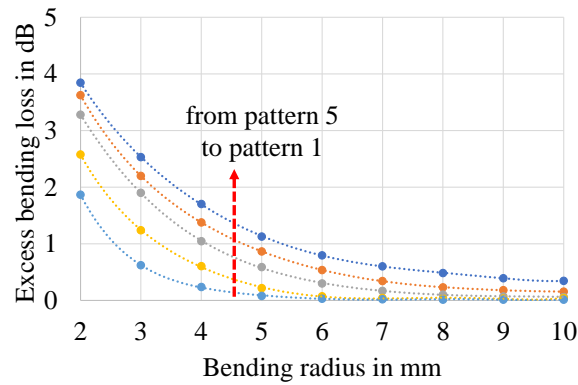
Figure 44 Simulated bending loss performance of waveguides for different RI profiles under 50 μm MMF, with RI changes in the y-direction (parabolic shape is changed).

A similar simulation was also carried out under a 4 μm SMF launch condition and the resulting bending losses are given in Figure 45. The results indicated a similar trend as shown under the 50 μm MMF launch. However, the difference here was quite small, at a maximum of around 0.1 dB. Changing the RI profiles does indeed have an influence on the waveguide performance, but it will have much lesser effect when the waveguide is under restricted launch conditions.
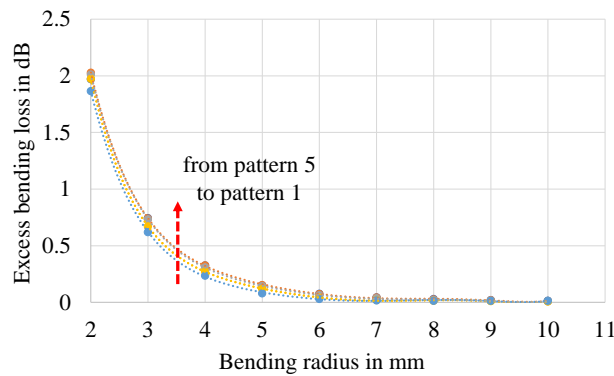
Figure 45 Simulated bending loss performance of waveguides for different RI profiles under SMF launch.

3.3.3 Simulation of transition effects

Transition loss is caused by to the mode distribution mismatch between a straight waveguide and a bent waveguide. The transition loss can be calculated directly from mode profiles based on the mode coupling equation. This section builds a link from the incident angle to the transition loss based on the ray tracing method. This method is quite simple and fast and could help in determining the best transition area to minimise bending losses. The simulation mode is shown in Figure 46, where it should be noted that there is no gap in the simulation between the straight and bent waveguides. The gap is shown in the figure in order to show this method clearly. A single ray source is used during the simulation, and the position p and ray angle θ are changed each time, as shown in the figure. When the ray hits the boundary of the waveguide, the resulting angle β is measured and stored. A relationship between ray angles in the straight waveguide and bent waveguide can thus be built.
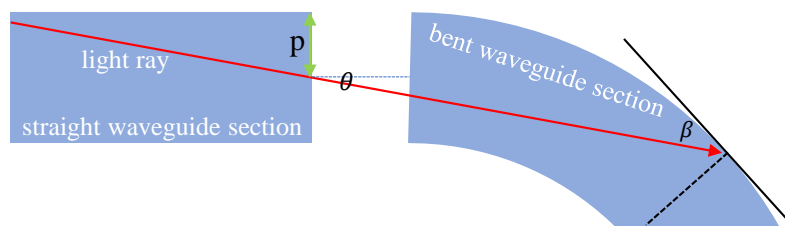
Figure 46 Schematic of transition loss. The change of ray angle from straight waveguide section to bent waveguide section was simulated based on the ray tracing method. The gap between straight and bent waveguide sections is only for the illustration and there is no gap between these two sections in simulation.

The results are given in Figure 47, where bending radius was set to be 2 mm and waveguide core width was 50 μm. In the first figure (Figure 47 a), y-axis is the distance of the light ray position from the top (outer), and the distance is indicated by point p in Figure 46, and the x-axis is the ray angle in the straight waveguide section, which is θ in Figure 46. The colour represents the value of the same ray angle in the bent waveguide section, which is β in Figure 46. The colour in the second figure (Figure 47 b) shows the angle difference of the same ray in different waveguide sections ($\beta - \theta$). The simulation results show that all ray angles are increased, and this angle change is simply due to the geometry difference in the bending area. Some previous light lies within the total internal reflection (TIR) angle in the straight section but is then bigger than the TIR angle after coming into the bending area. As a result, those rays leak out of waveguide causing transition loss.

Another conclusion can be drawn from the second plot. The angle increment is much smaller when the ray position is located near 0, which means that if the rays are more concentrated on the top area (outer) of the waveguide, the angle increment is smaller, or in other words, the resulting transition loss is smaller. This method provides useful information for designing real waveguides. If the waveguide bends in only one direction, we can design and put the high RI region of the core much closer to the outer (bend) area of the waveguide. However, this conclusion is drawn based on the fact that the straight and bent sections of waveguides are in a step-index profile.
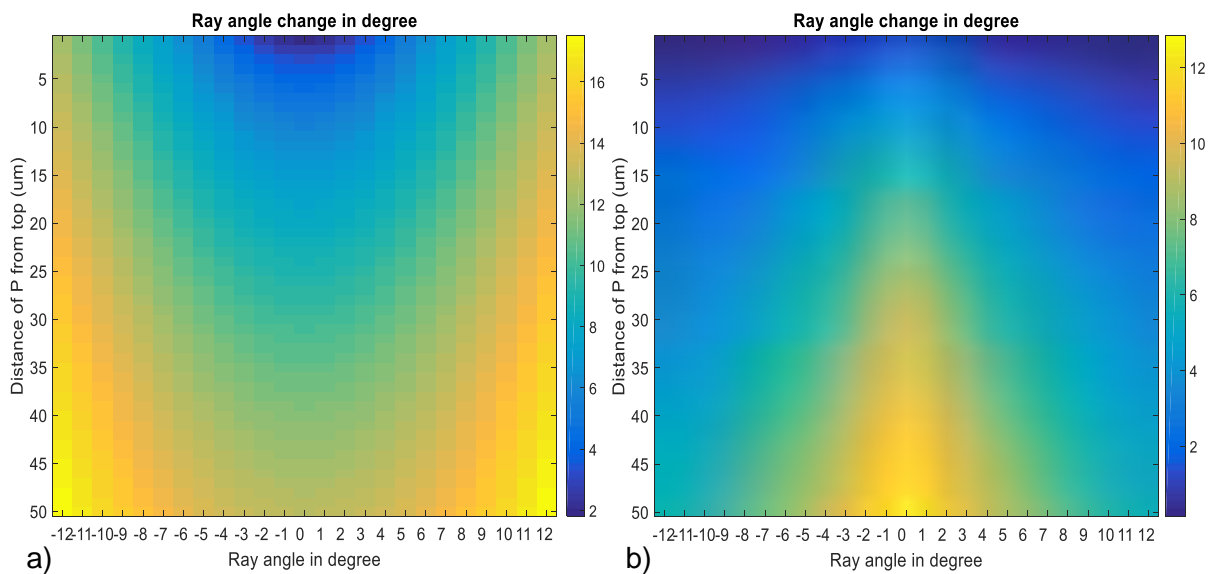
Figure 47 a) Ray angle generated in the bent waveguide section as a function of ray angle and ray position in straight waveguide section. b) ray angle difference of the same ray measured in straight waveguide and in bent waveguide as a function of ray position and ray angle.

3.3.4 Bending loss improvement

Based on previous studies, we know that when the waveguide is bent, power will leak out of the waveguide causing bending loss. A graded-index waveguide performs better than a step-index waveguide. However, this bending loss is still a little bit high, especially for a small bending radius. Reducing excess bending loss for a small bending radius would be an exciting work as sometimes tight bending is needed in the real world. Previous simulation has shown that even for a graded-index waveguide, the RI difference between the core and cladding is much more important than the profile distribution itself. Thus, increasing the RI difference is a promising way to reduce the bending loss by quite a lot. Fortunately, some work has been done in [133] that has experimentally proven this

concept. The best way to increase the RI difference is to remove the top cladding material in the bending area, as the RI of air is 1. As a result, the waveguide is surrounded by air and the refractive index difference is around 0.52 in the bending area. Bottom cladding remains to support the waveguide core. Thus, some light can leak out of the waveguide via the bottom boundary after hitting the outer side wall of the waveguide. The simulation model was also built in ZEMAX, and the model structure is shown in Figure 48.
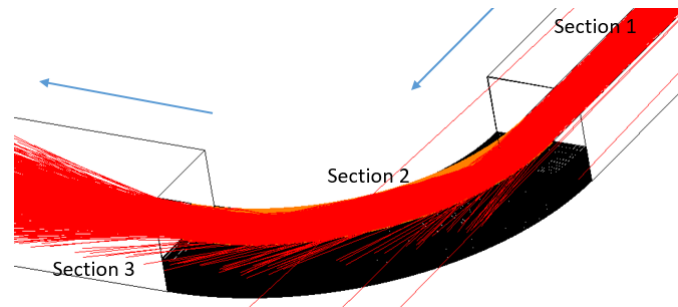
Figure 48 Waveguide structure in simulation of air-exposed waveguide model based on ZEMAX software. Section 1 and

section 3 are straight waveguide sections and section 2 is bent waveguide section without top cladding. In section 2,

waveguide core is directly exposed into the air.

The model consists of three sections: two straight parts, and one 90° degree bending part. As can be seen, the top cladding is removed in the bending area and bottom cladding remains to support the waveguide core. The structure indication shows that some light rays leak out of the waveguide via the bottom cladding. Three different input launch conditions were employed in this simulation: VCSEL, 50 μm MMF, and uniform input. VCSEL and 50 μm MMF are commonly used in the real world, and uniform input was employed to simulate the worst performance case of a waveguide. The simulated results are given in Figure 49.
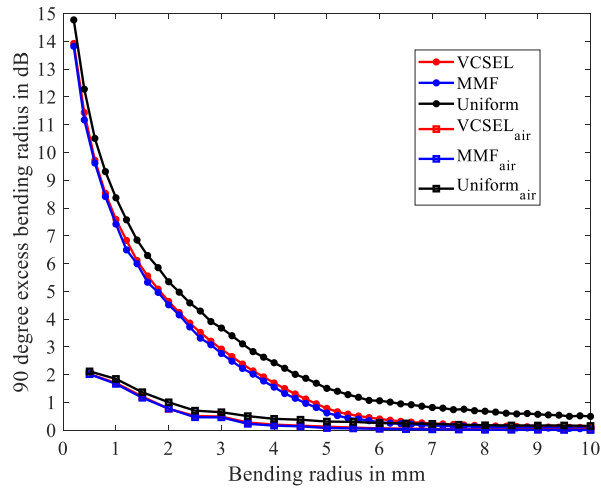
Figure 49 90° bending loss of normal waveguide structure and air-exposed structure under different launch conditions

based on ZEMAX software.

The circular markers are the results of 90° bending loss of a normal graded-index waveguide while the squared markers are the results of the new air-exposed waveguide. The bending losses were carried out under three inputs. The results showed a significant improvement in reducing bending loss by employing the air-exposed structure no matter which input launch condition was used. For a small bending radius, for example, at a 1 mm bending radius, the new air-exposed structure had a 10 dB improvement compared to a traditional waveguide, and its performance was still quite good even under uniform input launch. One drawback of this new structure is that the waveguide core is unprotected. It can be easily contaminated or damaged by the outside world. Section 4.9 introduces a new design layout of waveguide. It has great waveguide bending performance while the waveguide core remains fully protected.

Chapter 4 Flexure effects of polymer waveguides on flexible substrates

This chapter introduces a detailed study of flexible polymer waveguides. First, the parameters of polymer waveguides are given and then mode excitation studies are carried out. It is well known that the performance of polymer waveguides is highly reliant on the mode excitation at the beginning of the transmission. Thus, the mode excitation of different input launch conditions needs to be studied and controlled. Bending and twisting performance are then investigated regarding losses and crosstalk performance under different bending radii and numbers of twisting turns. Next, the dynamic behaviour measurement results of flexible polymer waveguide reveal that polymer waveguide links are stable and robust. Finally, a new layout for a bend-insensitive waveguide structure is proposed, and the experimental results indicate that it has a significant improvement in bending loss performance.

4.1 Profiles of flexible polymer waveguides

The polymer waveguides employed in this work were fabricated from siloxane materials developed by Dow Corning Corporation for use in PCB board level integration and optical backplanes for server racks in data centres. Details of the siloxane materials can be found in Chapter 2. These materials, known as WG-1020 for the waveguide core and WG-1023 for the waveguide cladding, can be deposited on various substrates and show very low losses, at around 0.04 dB/cm at the datacommunication wavelength of 850 nm. They can also withstand the high temperatures in excess of 350°C which make them suitable for traditional solder reflow and board lamination process and give them long-term stability [36]. All the waveguides used in this work were made using the same fabrication process, which means all the waveguide samples show similar refractive index profiles and similar behaviour. Those waveguides were fabricated on 125 μm thick Polyimide substrates using conventional photolithography. They have a cross section of around $50 \times 50 \, um^2$ as this is comparable to the core diameter of standard 50 μm MMF and offer a 1 dB alignment tolerance of $\pm 10 \, \mu m$ which can be readily achieved with conventional pick-and-place tools [20]. The refractive index difference between the core and cladding material is around 0.02 at 850 nm, yielding a

numerical aperture (NA) of ~0.25 for the waveguides. NA defines the maximum acceptance incident angle of the waveguide, and its formula is given below:

$$NA = n \cdot sin(\theta_{max}) = \sqrt{n_{core}^2 - n_{clad}^2}$$ (66)

Samples of different lengths were produced, including spiral flexible polymer waveguides, see Figure 50. In all experimental work, the waveguide facets are exposed with a dicing saw and no polishing steps are undertaken to improve the quality of the facets produced. Each flexible polymer waveguide sample contained an array of 12 waveguides with a pitch of 250 μm. This matches the standard pitch of multimode fibre ribbons and VCSEL arrays. The samples could be bent down to a 1 mm radius during experiments without any racking or delamination.
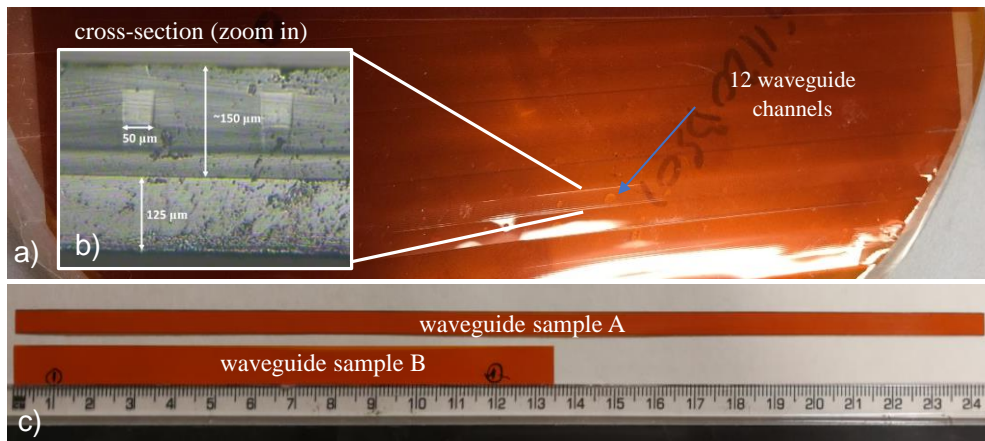
Figure 50 a) Flexible polymer waveguide samples used in this work, provided by Dow Corning company. b) cross-section

view of the flexible polymer waveguides, facet is not polished. c) two flexible polymer waveguide samples with different

lengths and widths.

The refractive index distribution of the samples is given in Figure 51 a), and all the waveguides have very similar RI distribution. This RI pattern was engineered to show this specific distribution and details of the engineering process can be found in [134]. Figure 51 b) shows the captured near-field image of the waveguide cross-section using an 850 nm VCSEL. It shows the power distribution and indicates that the majority of power concentrates at the bottom area of the waveguide core in the high RI region.
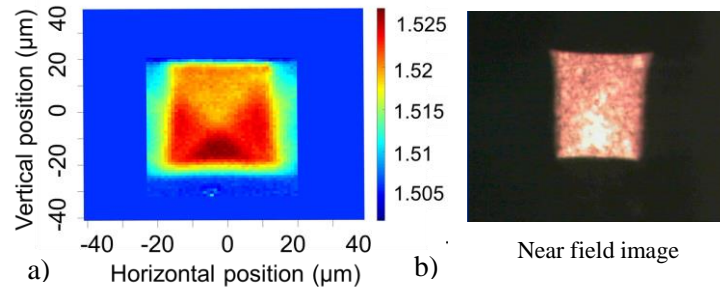
Figure 51 a) Measured refractive index profile of the real waveguide sample and b) its near-field image of the waveguide

output facet (illuminated by 850 nm laser light)

4.2 Mode excitation from different inputs

Due to the highly multimodal nature of these waveguides, the waveguide performance was investigated under different launch conditions. In this work three different input launch conditions ranging from restricted to relatively overfilled were employed: a 4/125 μm SMF (NA of 0.13), a 50/125 μm MMF (NA of 0.2) and a 100/140 μm MMF (NA of 0.29) input with a mode mixer (MM, Newport FM-1). The 4/125 µm SMF input excited the lowest number of modes inside the waveguide, while the 100/140 μm MMF input with a mode mixer excited the largest, which represents a 'worst-case' excitation with respect to bending loss as a larger percentage of power is coupled to the higher order modes which are more susceptible to bending loss at the waveguide input. The 50/125 μm MMF input consists of a launch that is between these two extremes (4 μm SMF and 100 μm MMF) and represents a common multimode fibre. The following figure shows the system setup for measuring the far-field profile of these three different fibre inputs. Two VCSELs were used as laser sources. For SMF input, the VCSEL light was coupled into an 8.3 µm SMF patch-cord via two × 10 lenses and the fibre patch-cord was connected to another 4/125 μm SMF. For the 50 μm MMF and 100 μm MMF inputs, the VCSEL light was coupled into a 50 μm MMF first and then went into their respective fibres. An additional mode mixer which could generate micro bends was introduced on the 100 μm MMF input to make output distribution much more uniform. At the receiver side, a broad-area photodetector (PD) was used, placed on a horizontal moveable stage. There was a metal mask in front of the PD with a 1 mm wide slot in the centre. During the experiments, the distance

between the fibre output and PD was set. In order to measure the far-field instead of the near-field, the distance should be larger than a certain value which can be calculated by:

$$d \gg \frac{2D^2}{\lambda} \qquad (67)$$

Taking the 100 μm MMF input, for example, the distance between the fibre output and PD should be larger than $\frac{2 \times 100 \ \mu m^2}{0.85 \ \mu m} \sim = 23.5 \ mm$ so that the far-field can be measured. By measuring the shifting distance of PD Δx and its corresponding power, we could get the output distribution of each input. The shifting distance relating to far-field angle is given below:

$$\theta = arctan(\Delta x/d) \qquad (68)$$
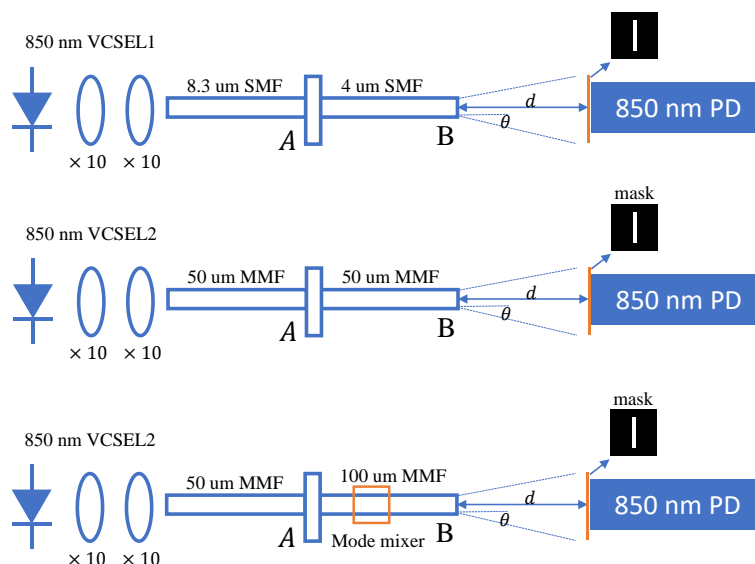
Figure 52 System setup for measuring far-field distribution of fibres. Laser light was coupled into the fibre first via a pair of ×10 lenses. A mask with a 1 mm wide slot in the centre is placed in front of the broad-area photodetector (PD).

The results are given in Figure 53. The 5% far-field intensity angle (FFA) of each input was found from the measured normalised far-field profile (-13 dB points) and was used to characterise the launch condition by comparing it with the acceptance angle (AAwg ~14.5°) of the waveguide. The 5% half FFAs of the three input fibres used in the experiments were found to be 7.1°, 10.9° and 16° for the SMF, 50 μm MMF and 100 μm MMF input, respectively, while the respective calculated values using the fibre NA were 7.5°, 11.5° and 16.8° for the SMF, 50 μm MMF and 100 μm MMF input, respectively. The measured FFA values were in good agreement with the theoretical values and

confirmed the characterisation of the SMF input as restricted launch (FFA < AAwg), the 50 µm MMF as typical (FFA ~ AAwg) and the 100 µm MMF input as relatively overfilled (FFA > AAwg).
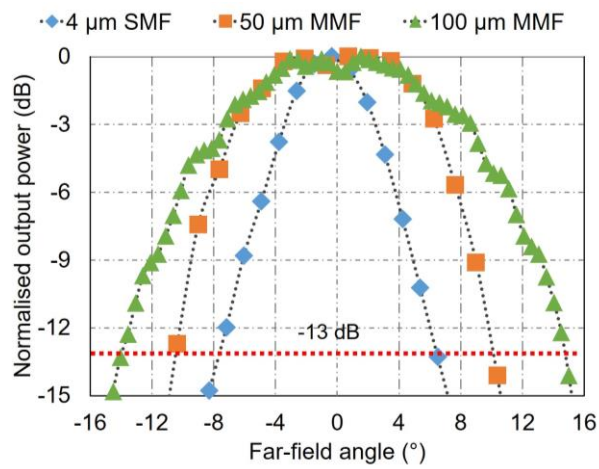
Figure 53 Far-field intensity profiles of three different launch conditions. Intersection points between intensity profiles and the horizontal red line (-13 dB) are corresponding to the 5% far-field angles. 4 µm SMF is used to simulate restricted launch condition, 50 µm MMF is used to simulate most common launch condition and 100 µm MMF is employed to simulate overfilled launch condition.

Near-field images of the three fibres were also carried out. The system setup was similar to the far-field one. On the receiver side, the photodetector was removed and replaced by a camera which could catch 850 NM light. At the end of the fibre output, another × 16 lens was employed to concentrate the divergent output lights, followed by an attenuator which was used to reduce the saturation of the captured images.
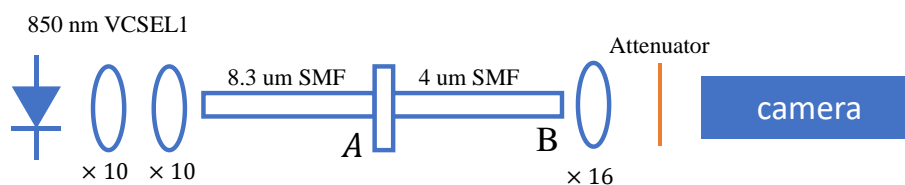
Figure 54 System setup for measuring the near-field image of input fibres. Laser light from 850 nm VCSEL is coupled into an 8.3 µm SMF first via a pair of ×10 lenses. Then, laser light is focused on a CCD camera via a ×16 lens. An attenuator is employed here to adjust the brightness of the light spot.

The near-field images are shown in Figure 55. As is clearly shown in the figure, the near field has a clear and pure circle shape due to the single mode nature of the 4 µm SMF. The 50 µm MMF is a

rough circular shape with the majority of its power concentrated in the centre, while the power distribution for the 100 μm MMF tended to be uniform across the whole section.
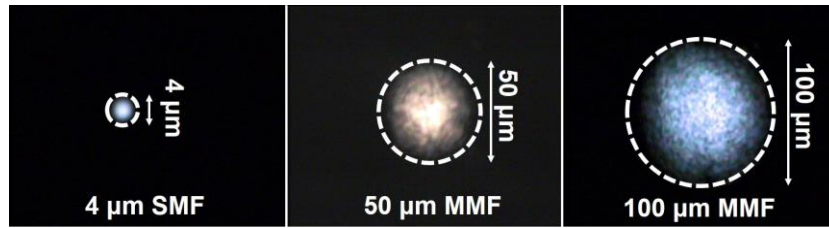
Figure 55 Near-field images of the cleaved input fibre end for three launch conditions.

From the section above, we can see that different launch conditions have different output distributions and near-field images. This difference will have a large influence on the performance of the waveguides due to the excitation of different modes. However, from the near-field images, we can see that these three different fibres have different diameters which could result in a geometry mismatch when aligning with the waveguide sample. This geometry mismatch will cause extra coupling loss, especially for the 100 μm MMF. This part briefly discusses coupling losses caused by this geometry mismatch.
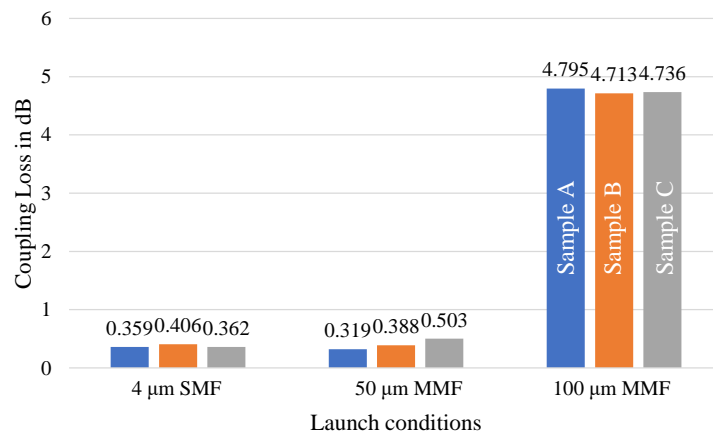
Figure 56 Coupling losses for different waveguide samples under three input launch conditions.

Figure 56 shows the measured coupling losses of three different waveguide samples under different launch conditions. Index matching gel was applied on the end facet of waveguide to minimise both its scattering loss and Fresnel loss caused by RI difference. From the results, the coupling losses under 4 μm SMF and 50 μm MMF were quite small, both being around 0.4 dB. For

the 100 μm MMF with mode mixer, the coupling loss went up to ~4.7 dB, which is quite big as compared to the other two input launches. There are two main reasons. The first one is the geometry mismatch between 100 μm MMF and 50 μm squared waveguide, shown in Figure 57. The 100 μm MMF has a larger diameter than the waveguide, and thus a large percentage of power is lost when coupling into the waveguide. A rough estimation of this geometry mismatch loss can be gained by calculating the ratio of the areas which is $-10\log(50 \times 50/(\pi \times 50 \times 50)) = 4.97$ dB. The second reason is due to the large number of modes that the 100 μm MMF input carries. Such a highly multimodal fibre will result a large divergence angle. When coupling into the waveguide, some light will leak out of the waveguide, causing losses. We notice from the first reason, that geometry mismatch will result in 4.97 dB loss, however, the measured coupling loss is around 4.7 dB which is below the theoretical value. In addition, adding up the mode loss due to the large divergence angle, the measured coupling loss should be bigger than 4.97 dB. The for this lower measured coupling loss is due to the non-uniform distribution of the output power. Although the 100 μm MMF is used to simulate a uniform distribution, it is not strictly uniform input, which can also be confirmed from its far-field distribution in Figure 53.
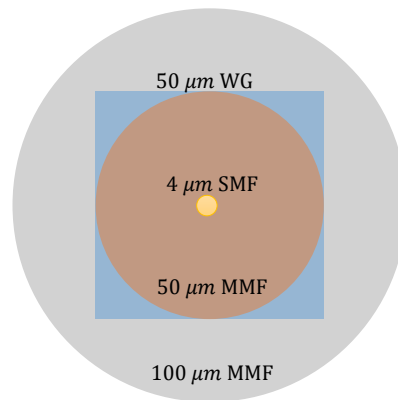
Figure 57 Mathematic illustration of the geometry mismatch between the waveguide and different fibre inputs.

4.3 Effect of bending radius

Bends play an important role in flexible polymer waveguides as they are normally involved when the waveguides flex. Thus, exploring the bending effects and especially bending losses is promising work for flexible polymer waveguides. This section explores the bending loss performance under different launch conditions. The system setup is shown in Figure 58. An 850 nm wavelength

vertical-cavity surface-emitting laser (VCSEL) was used as the input source and the emitted light was coupled into fibre patch-cord via a pair of $\times 10$ microscope objectives with a NA of 0.25. A second fibre patch-cord of the same type with a cleaved end was used to couple the light into the waveguides. The flexible polymer waveguide was 13.5 cm long and was bent around a cylindrical mandrel for a given specific angle of curvature. At the end of the waveguide sample, a $\times 10$ microscope objective with NA of 0.32 was used to collect the transmitted light and focus it onto an optical power meter. All the NAs of the objectives was ensured to be larger than the NA of the waveguide, ensuring that all the light was transmitted and collected via the whole system.
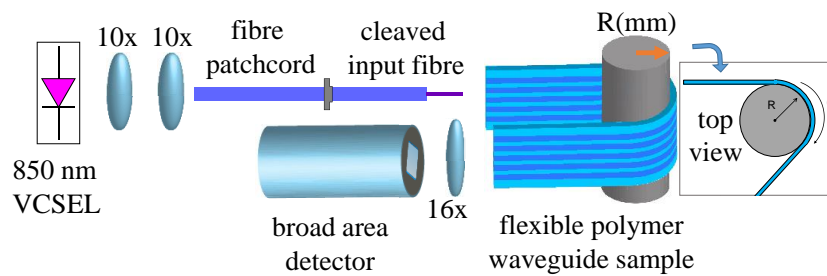
Figure 58 Experimental system setup for bending loss studies. An 850 VCSEL is used as the input source. Laser light is coupled into fibre patch-cord first and next coupled into the bent waveguide. The waveguide sample was bent at 180°. At the receiver side, a broad-area PD is used to collect the power via a ×16 lens.

Index matching gel was applied at the waveguide input to minimise the Fresnel loss and scattering loss due to the rough surface roughness. Mandrels with different radii of curvature between 2 and 15 mm were used during the work. The bending angle was set to be 180° and a straight waveguide was also used as a reference. An image of the bent waveguide sample under illumination with red light is given in Figure 59, in which FLW indicates the flexible waveguide. For each measurement and launch condition study, the insertion loss of all twelve of the waveguides in the sample was obtained and the average value was calculated. In order to obtain the excess loss due to waveguide bending, the insertion losses of waveguides were measured for all different launch conditions when no flexure was applied. The average insertion losses for the straight waveguides were found to be ~1.4, 1.5, and 5.9 dB for the 4 μm SMF, 50 μm MMF, and 100 μm MMF launches, respectively.
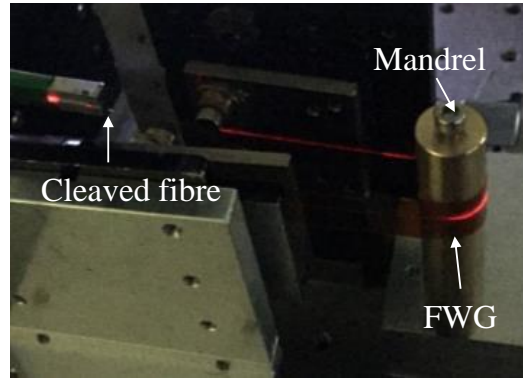
Figure 59 Image of the bent waveguide sample illuminated with red light.

The measured excess bending losses (indicated by markers) for all launch conditions are given in Figure 61. As expected, the use of the 100 µm MMF input resultant in a large excess bending loss due to the excitation of higher order modes at the waveguide input. For the less overfilled launches, however, a good bending loss performance was recorded. The minimum radii to achieve 1 dB bending loss were found to be 3 mm and 6 mm for the SMF and 50 µm MMF inputs, respectively. Ray tracing simulations were carried out with ZEMAX to validate the observed results. The refractive index (RI) profile of the waveguide was assumed to have a gradient profile similar to the profile obtained from waveguide samples fabricated on rigid substrates, as shown in Figure 60. Details of the RI pattern effect can be found in Chapter 3.3.
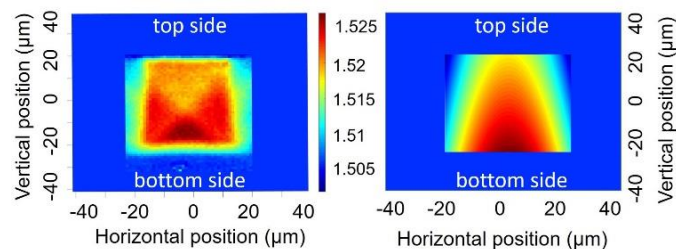
Figure 60 Measured refractive index of the waveguide sample and simulated profile in ZEMAX for flexible waveguide studies. The simulated profile has roughly the same RI distribution as the real waveguide sample.

The different launch conditions used in the experiments were implemented in the simulations by matching the angular profile of the ray source at the waveguide input to the far-field profile of the respective fibre input (Figure 53). The excess bending loss was once more obtained by subtracting the insertion loss of the waveguides when no flexure was applied (straight waveguides). The obtained

simulation results are plotted in Figure 61 with solid lines. Good agreement was achieved between the simulated and experimental curves. Simulations were done to assess the effect of the graded-index (GI) shape in the RI profile on the loss performance of these flexible waveguides in comparison with the case of the step-index (SI) shape. It was assumed that the waveguides had the same RI difference between the core and cladding, and the same dimensions but with a uniform RI profile over their cross section. The obtained results are also plotted in Figure 61 for a SMF and a 50 µm MMF input. As expected, the graded-index profile provided an improved bending loss performance due to the increased mode confinement within the waveguide core.
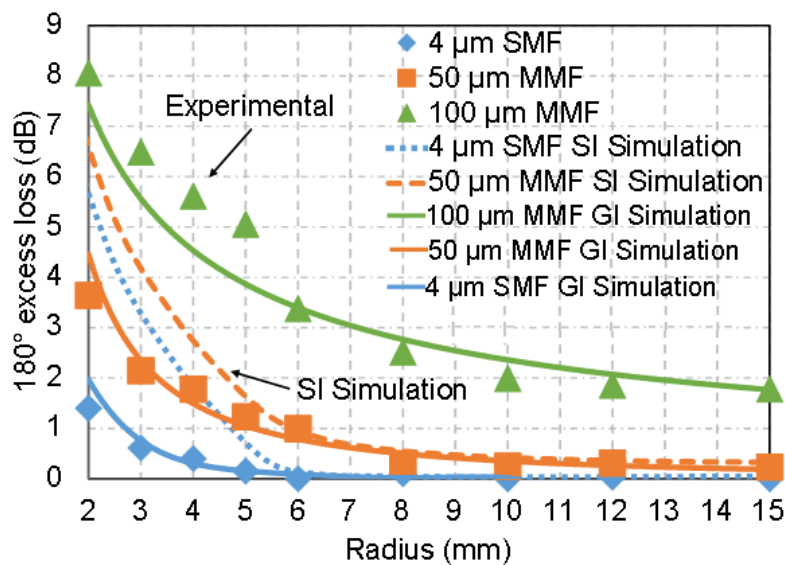
Figure 61 Excess bending loss for different bending radii under three launch conditions: experimental results (markers), simulation results with GI profiles (solid lines) and simulation results by employing SI profiles (dash lines).

Near-field images of the waveguide output were also captured and stored under different bending radii and different launch conditions. For the same waveguide, the captured near-field image pattern became smaller and smaller as the bending radius decreased, which proves that there is a suppression effect of the higher order modes for all inputs due to the tight bends. For small radius bends, the higher order modes easily leak out of the waveguide while lower order modes can still propagate.
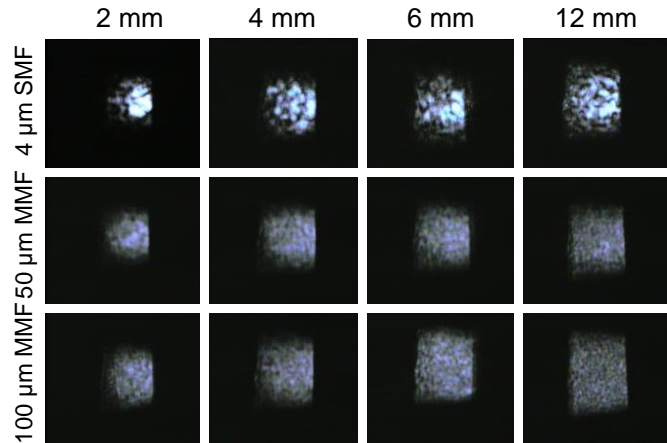
Figure 62 Near-field images of the waveguide output for different bending radii under different inputs. Bending radii were chosen to be 2 mm, 4 mm, 6 mm and 12 mm.

4.4 Effect of bending angle

The bending loss of the waveguide was also recorded when the angle of curvature varied between 0° and 180° for a fixed radius of curvature. The system setup is shown in Figure 63. All the setups were the same as for the previous bending radius test. Once the bending radius was set, the bending angle varied every 30°. This section studies how light leaks out of the waveguide along bending sections.
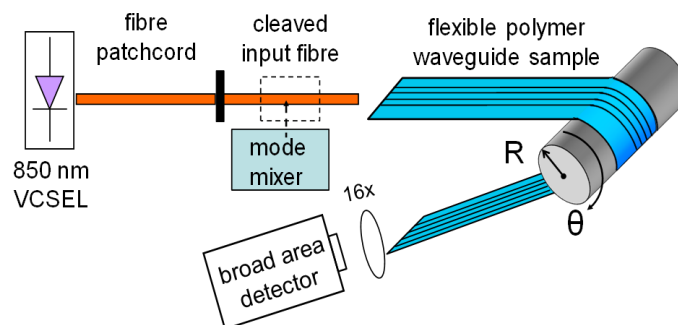
Figure 63 Experimental setup for the bending angle effect. Flexible polymer waveguide sample was bent on a mandrel with different bending angles from 0° to 180°.

The results are given in Figure 64. It can be observed that the excess bending loss curve exhibited a decreasing gradient with increasing bending angle. Similar behaviour was observed in multimode waveguide crossings [135], and can be explained by the fact that the majority of the power in the

higher order modes is lost in the initial parts of the bends, with the remaining lower order modes, that exhibit lower bending loss, left to propagate along the remaining length. The effect is more pronounced for the 100 µm MMF input as a higher percentage of power is coupled to the higher order modes which are more susceptible to bending loss.
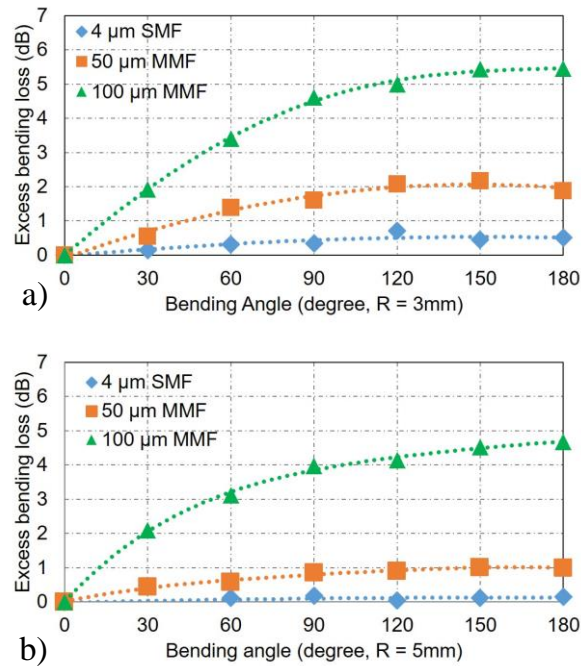
Figure 64 Excess bending loss as a function of bending angle for (a) 3 mm and (b) 5 mm radius for the three launch conditions studied.

Near-field images of the waveguide output were recorded for the different angles of curvature when a 3 mm radius was used, see Figure 65. The images confirm the above observations, clearly showing the suppression of the higher order modes for the 100 µm launch as the bending angle increased. Alternatively, for the SMF input, the light was well confined in the waveguide bottom centre (region of higher RI) with the relative intensity over the waveguide core not changing significantly.
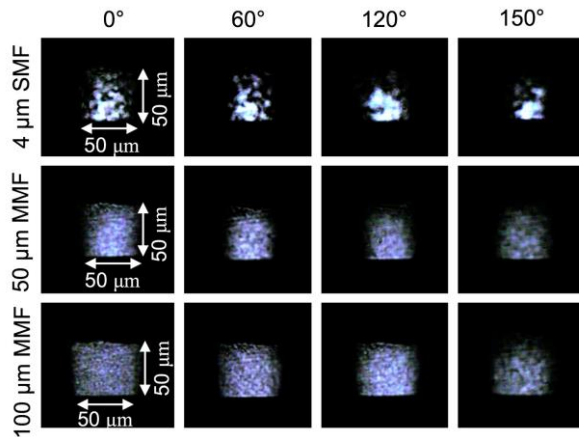
Figure 65 Near-field images of the waveguide output for different bending angles for a 3-mm bending radius under three

launch conditions. 0° means waveguide sample is in straight condition.

4.5 Effect of bending direction

Due to the asymmetry in the RI profile of the waveguides, the bending loss was expected to be different when the same sample was bent in two opposite out-of-plane directions as shown in Figure 66: upwards (with the top side located in the inside part of the bend) and downwards (with the bottom side located in the inside part of the bend). For upwards bending, the substrate lay in the outer layer of the bend, resulting in protection of the waveguide. The polyimide substrate was stretched, and the polymer waveguide layers were squeezed. Thus, the waveguide was hard to break. However, in downwards bending, the waveguide lay in the outer layer and was stretched. The sample was easier to break under this bending direction at a small bending radius of curvature (1 mm).
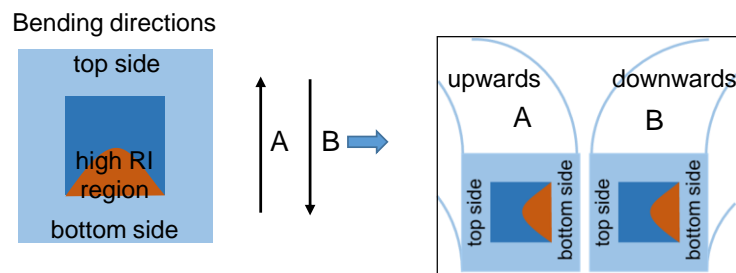
Figure 66 Schematic illustration of the two out-of-plane bending directions. Due to the asymmetric RI profile, different

bending directions will generate different configurations (A and B).

Measurements were carried out to quantify the bending direction effect on a 24 cm long sample when the sample was bent in these two directions using the setup shown in Figure 58. It was expected that the upward bending (type A) should result in a larger excess loss as the region of higher RI was positioned towards the outer side of the bend, resulting in worse mode confinement, while the difference in performance was expected to be much larger for tighter bends (smaller radii) and more overfilled inputs. Figure 67 shows the difference in obtained excess bending loss between the upward (type A) and downward (type B) bends for 3- and 5-mm radius.
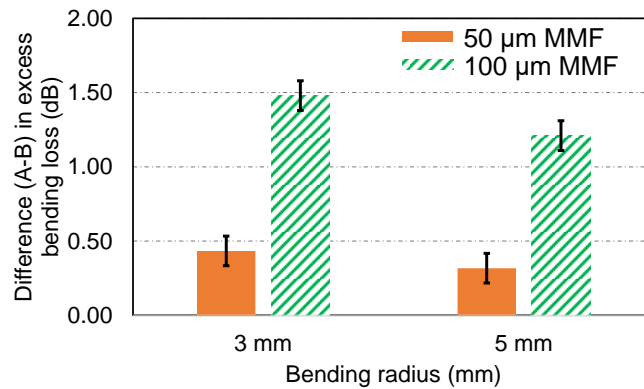
Figure 67 Difference in excess bending loss between directions A and B when the sample is bent 180° with a 3- and 5-mm radius, respectively. Positive values mean that the bending loss in A configuration is higher than the bending loss in B configuration.

The obtained results were in agreement with the expected performance. The 100 µm MMF input resultant in a 1.5 dB difference in loss between the two bending directions for the smaller 3 mm radius, whilst the 50 µm MMF input yielded a much smaller difference of ~0.4 dB for the same bending radius. Overall, the obtained results indicated a small difference in bending losses between the two opposite bending directions.

4.6 Effect of twisting

Twisting is another important behaviour of flexible polymer waveguides, and during the experiment, the loss performance of the flexible sample was also investigated under in-plane twist using same launch conditions. The main system setup is shown in Figure 68.
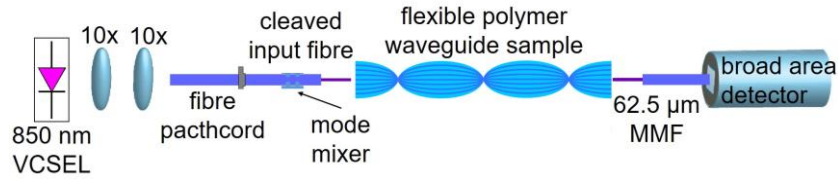
Figure 68 System setup for the twisting loss experiment. 850 nm VCSEL was employed as laser source. Waveguide was twisted by different number of twisting turns.

Twisting is a quite complex action, especially for an elastic polymer material. The thickness, applied force, waveguide width and number of twisting turns will all have an effect on the shape of the waveguide, with different effects on performance [136]. Thus, in this work, three different waveguide samples were employed for measuring the twisting performance of the waveguide. The first flexible polymer waveguide sample had a length of 10 cm, width of 1 cm, and a thickness of 0.02 cm. The resulting twisting patterns are given in Figure 69. Due to the tension of the polymer material, the sample generated a twisting node (indicated on figure) when two or and more twisting turns were applied. This twisting node was in a spiral shape and had similar performance to the bending circle. As for twisting turns equal to or less than 1, the light path was more likely to be a straight line.
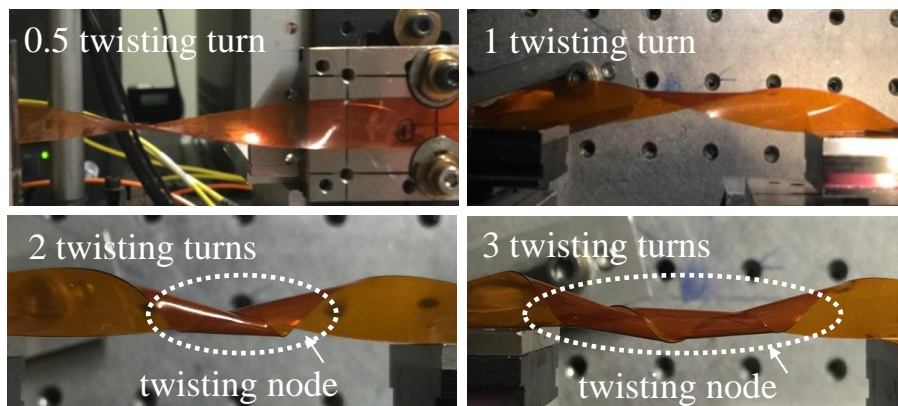
Figure 69 Twisting patterns of a flexible polymer waveguide sample for different numbers of twisting turns. When twisting turn is bigger than 1, twisting nodes are generated. Waveguide sample is 10-cm long and 1-cm wide.

The measured excess twisting losses vs the number of twisting turns is given in Figure 70, where 1 full twisting turn indicates 360° twists. Obviously, the results can be divided into 2 parts. For the first three twisting losses, there is no twisting node involved, and the resulting excess twisting loss is near 0. The waveguide sample has 0.5 dB excess loss only under 100 µm launch. However, for the

last three results, the excess twisting loss increased a lot due to the existence of a twisting node, especially under 100 µm launch. Once a twisting node has been generated, the excess twisting loss will be relatively stable. As mentioned in the bending angle loss performance study, the majority of the power was lost in the first 90° of bends. The following loss increased slowly when the bending degree increased further. Due to the small length and large width of the waveguide sample, a large force needed to be applied to generate two or more twisting turns. Thus, the measured loss for the last three twisting patterns resultant in a large fluctuation.
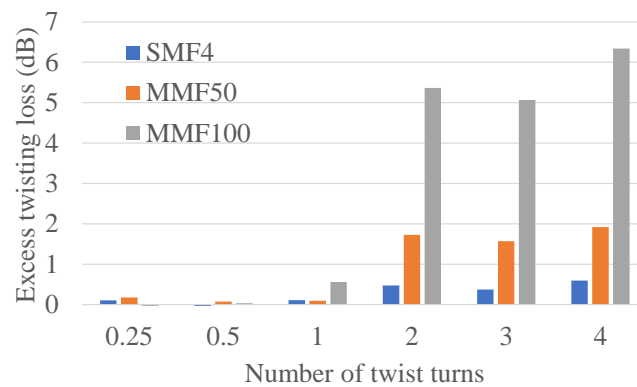
Figure 70 Average excess twisting loss for the 10 cm flexible polymer waveguide sample as a function of twisting numbers. When number of twist turns is bigger than 1, twisting nodes are generated, which results in bigger loss. Three different input launches are employed.

In order to reduce the fluctuation and get rid of the twisting node effect, the second and third waveguides (named as sample A and sample B) were chosen to be 24 cm long and 0.6 cm wide. The average insertion loss of the waveguides was measured when no twist was applied, and this was found to be ~3.2, 3.6, and 9 dB for the 4 µm SMF, 50 µm MMF, and 100 µm MMF inputs, respectively. The waveguide samples used in this section their twisted images are shown in Figure 71. The waveguide sample was stretched in order to ensure that the length of the twisted sample was similar to that when no twist was applied (straight samples), and was then clamped. In order to minimise the effect of lateral tension on the samples, the third sample width was reduced from 6 mm to 2mm (Sample B).
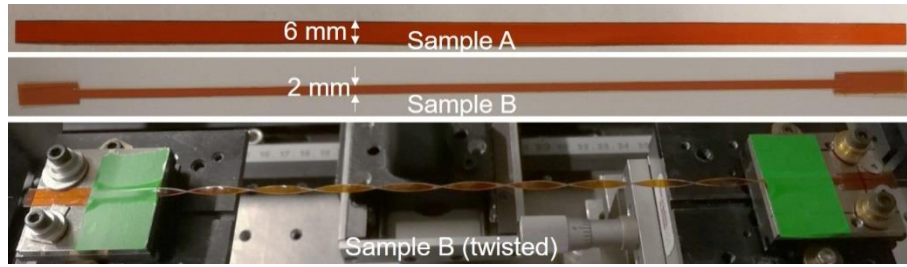
Figure 71 Flexible polymer waveguide samples used in twisting loss measurements: (a) sample A 24 cm long with 6 mm width and (b) sample B 24 cm long with 2 mm width, and (c) image of twisted sample B under 5 full (360°) twist turns.

The obtained excess twisting losses for both 24 cm long samples are shown in Figure 72. For the sample with reduced width (sample B), only 4 waveguides were operational, and these were used to determine the average insertion loss for each number of turns. The twisting losses of sample A are plotted in unfilled bars while the losses for the width-reduced waveguide are plotted in filled bars. For all launch conditions and for both samples, the excess twisting loss was below 0.8 dB even for four full 360° turns. For the SMF and 50 µm MMF input, the excess twisting loss for up to four full turns for sample A was below 0.3 dB. The reduction of the sample width in sample B minimised the lateral tension induced in the sample, resulting therefore in an improved twisting loss performance for all launches. A negligible excess loss of 0.1 dB was obtained for sample B for the SMF and 50 µm MMF inputs for up to four full twisting turns.
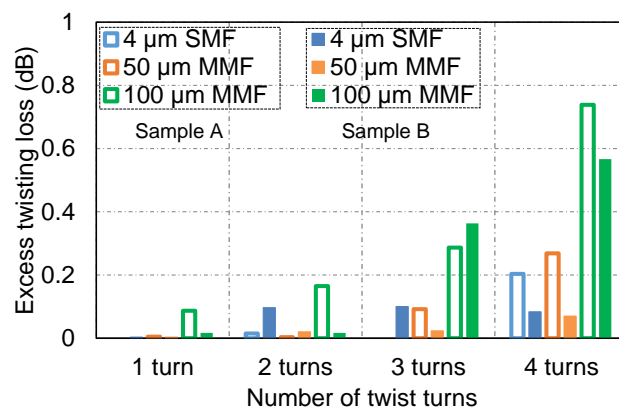
Figure 72 Average twisting excess loss for samples A and B as a function of the number of full 360° twists for the different launch conditions. Unfilled bars are the results of sample A and filled bars are the results of sample B.

From the twisting loss results, it can be seen that a pure twisting effect has only a small influence on the waveguide performance unless twisting node is involved. Details of helicoids, wrinkles and loops in twisted ribbons have been studied in [136-138]. The different shapes of the resulting twisted ribbon and their phase (twisted angle) diagram are given in the figure below.
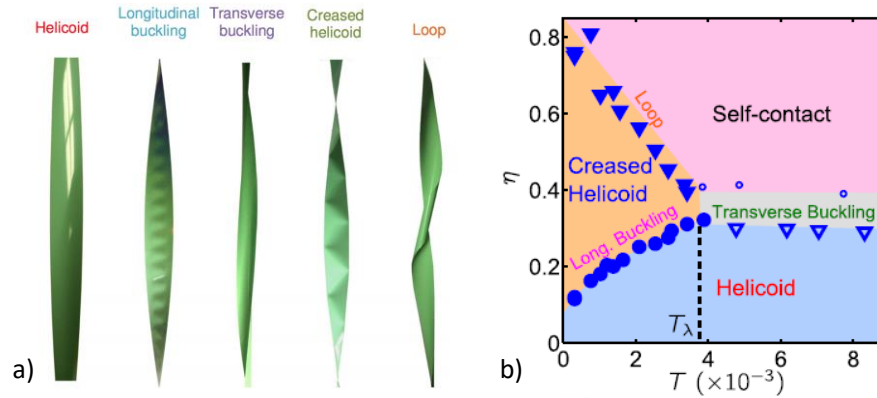
Figure 73 a) Buckling modes of twisted ribbon, there are five patterns: helicoid, longitudinal buckling, transverse buckling, creased helicoid and loop, b) experimental phase diagram in the tension-twist plane [137]

The figure above shows that many twisted patterns can be generated when twisting an elastic ribbon, especially in the last loop pattern. It was observed when we twisted the 10 cm long waveguide over one twisting turn (see Figure 69), a twisting node (loop) was generated, causing a much higher twisting loss. Using the equations provided in [137], phase diagrams were plotted based on the parameters of flexible polymer waveguide samples, which are given in Figure 74. Depending on the material, Young's modulus was found to be 2.77 Gpa for all three samples. Details of the parameters for each sample are listed on their plots, respectively. The x-axis is the force, and the y-axis is the number of full twisting (360°) turns. Although the plot is divided into three parts, we only concentrated on two parts: the self-contact part and the helicoid part. Above the red line, the twisted waveguide sample will be in self-contact, generating a loop (twisting node), or below the red line, showing only a helicoid shape.

From the results below, the 10 cm long waveguide sample went into self-contact when there was more than one full twisting turn, which occurred in the real world during the measurements. For waveguide sample A, the maximum twisting turns obtained for the helicoid shape during the measurement was six full turns, which also agreed with the plot. And for waveguide sample B, the

theory predicted that it could be twisted up to around 45 full twisting turns without generating any loop. However, during the measurement, only up to six twisting turns were applied and the sample could be very easily twisted into a helicoid shape. Based on this mode, when a twisted polymer waveguide needs to be designed, the waveguide length and width and the number of twisting turns can be therefore calculated to avoid any loops developing, thereby achieving a very low twisting loss.
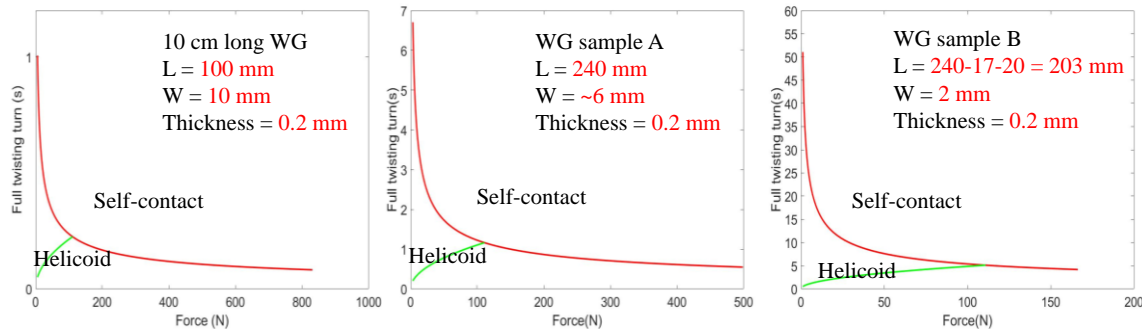
Figure 74 Phase diagrams of all three twisted flexible polymer waveguide samples. The maximum number of twist turns can be therefore obtained from the plots.

4.7 Crosstalk performance under flexure

The crosstalk performance analysis of polymer waveguides was also carried out. From previous studies, [139] has shown that the crosstalk of a straight polymer waveguide is below -40 dB, which is good enough for use in the real world. However, due to the flexure involved, more power will leak out of the waveguide core. That leakage power is likely to couple back to an adjacent waveguide resulting in a high crosstalk value. Therefore, in order to better determine the crosstalk performance, crosstalk measurements and simulations of flexible polymer waveguides under flexure must be performed.

4.7.1 Simulation of crosstalk performance

Simulation of waveguide crosstalk performance was carried out first. The simulated 50 μm MMF input was set to have the same angular profile as the real 50 μm MMF input, and also to have the same beam size. The following figure shows the input and output side of the simulation setup. It can be seen that three waveguides were built with a pitch value of 250 μm. During the simulation, the position of the input fibre was shifted horizontally from the left to right, and at the receiver side, a photodetector was set to measure the power inside the middle waveguide. The whole waveguide

structure was surrounded by air that has a refractive index of 1.0. As the input launch moved, the received power of the middle waveguide output was recorded.
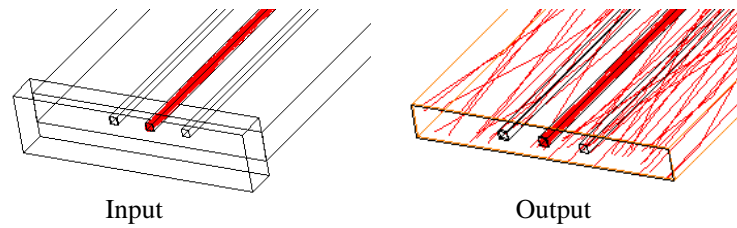
Input   Output

Figure 75 Input and output side of the simulation setup for crosstalk measurement in ZEMAX. Three waveguides are designed with a pitch value of 250 μm. At input side, laser light was coupled into middle waveguide and at output side, the power in adjacent waveguide was measured.

The results of the simulated crosstalk performance of the polymer waveguide are given in Figure 76. A 180° bend was introduced in the middle of the waveguide structure and different bending radii were applied, ranging from 1 mm to 10 mm in steps of 1 mm. The x-axis is the position of the input fibre where 0 means that input fibre was well aligned to middle waveguide, and the y-axis is the normalised received power of the middle waveguide at the output side. The three waveguide positions are indicated on the graph by red dashed lines. It can be seen from the results that the crosstalk values under 50 μm MMF input were less than -30 dB when the bending radius was larger than 4 mm. Further reducing the bending radius resultant in much greater bending loss. The lost power remained in the cladding and would re-couple back to adjacent waveguides. Thus, the crosstalk value for small bends is quite high and can go up to -15 dB for a 1 mm or 2 mm bending radius.
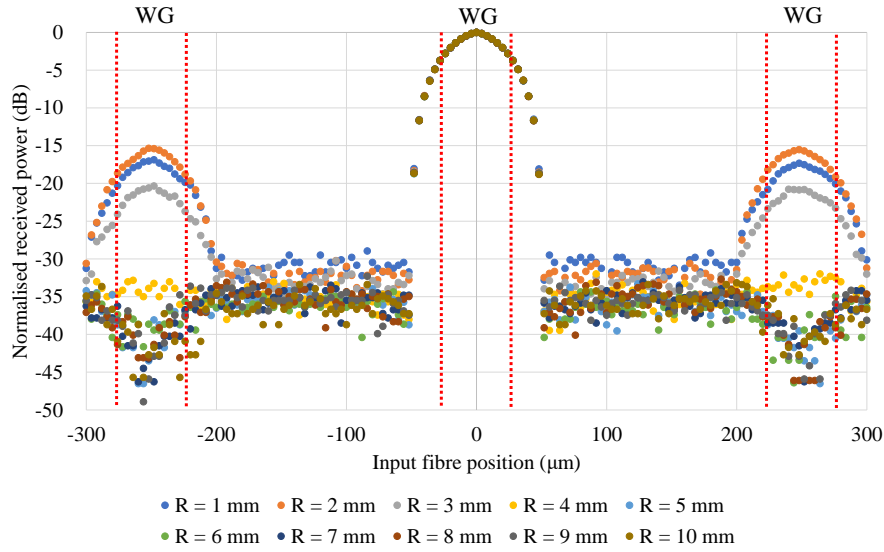
Figure 76 Simulation of the normalised received power at the waveguide output as a function of the input source position for different bending radii for the 50 μm MMF input. Waveguide positions are indicated by red dash lines.

4.7.2 Experimental results of crosstalk performance of bends

The crosstalk performance of the 24 cm long sample under a flexure 180° bend was also investigated. The system setup employed was similar to that used in the bending loss measurements, as shown in Figure 77. On the receiver side, the lens was replaced by a 62.5/125 μm graded index MMF. The use of the fibre was preferred for these measurements as it minimised the collection of stray background light at the waveguide output, while the size and NA of the 62.5/125 μm graded index MMF used ensured the collection of the majority of the power received at the waveguide output. Similar to the simulation, the output fibre was aligned with one of the waveguides, while the position of the input fibre was offset between the two adjacent waveguides. The optical power received for each input position was recorded and the crosstalk was derived by comparing the output recorded when the input was well aligned with each of the adjacent waveguides. The measurement was repeated for the different launch conditions and for different bending radii. Index matching gel was applied to both the input and output waveguide facets to minimise additional loss and crosstalk due to facet roughness.

85
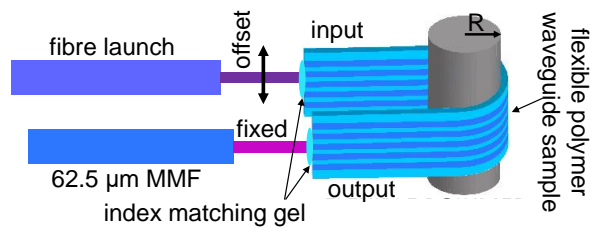
Figure 77 Schematic of crosstalk measurement of the bent waveguide sample. Fibre launch was employed at input side with adjustable position. Output side, a 62.5 μm MMF with fixed position was used to collect the power. Index matching gel was applied on both side of couplings.

Figure 78 shows the normalised received power at the waveguide output as a function of the position of the input fibre for the 4 μm SMF launch for different bending radii. The small peaks observed in the figure occur when the SMF input was positioned at the waveguide edges (left/right sidewall) and are due to the additional scattering induced by the core-cladding boundary. This effect was observed in all measurements (straight and bent waveguides) but became less pronounced as larger and more overfilled inputs were employed. Similar measurements were also carried out under 50 μm MMF and 100 μm MMF inputs as well, and their crosstalk behaviour is shown in Figure 79. When the position of the input fibre was placed to the cladding area (between two slab waveguides), the resulting crosstalk was less than the value obtained when the fibre was placed to adjacent waveguide. This phenomenon occurred in all three launch conditions. When the fibre input was placed at the cladding area, all the light power was injected into the cladding and is confined in the planar waveguide formed by the cladding and air. After the bending area, only a small portion of the power was coupled back to the waveguide again, resulting in a low crosstalk value. However, when the fibre input was placed at the centre of the adjacent waveguide, all the power was confined inside the waveguide and propagated until reaching the bending area. In the bending area, some power will leak, and that leakage power more easily couples back to the adjacent waveguide, causing higher crosstalk.

86
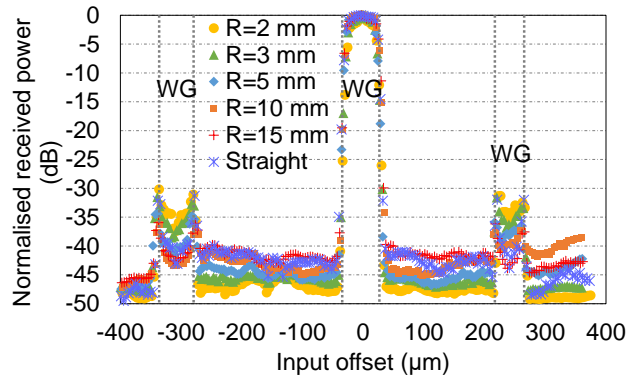
Figure 78 Normalised received power at the waveguide output as a function of the input position for different bending radii

for the 4 µm SMF input.
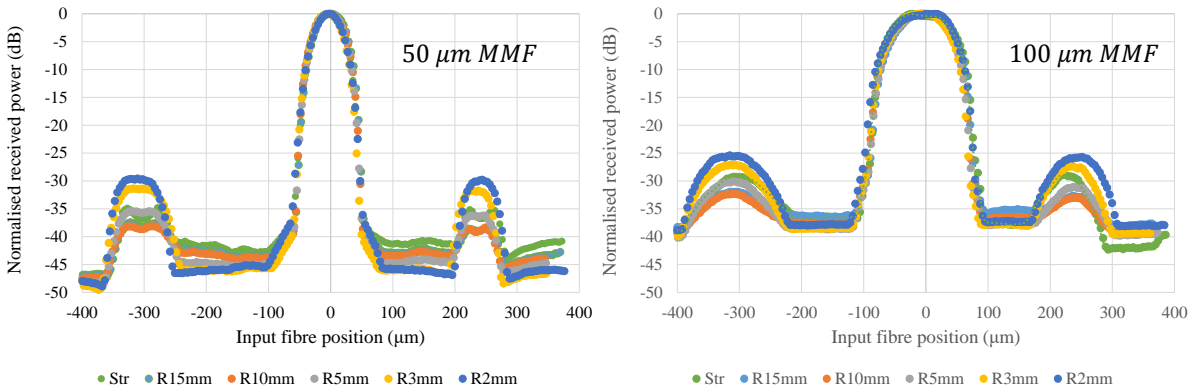
Figure 79 Normalised received power at the waveguide output as a function of the input position for different bending radii

for the 50 µm MMF input (left) and 100 µm MMF input (right), respectively.

A summary of the obtained crosstalk values as a function of bending radius for the different launch conditions is given in Figure 80. The crosstalk was found to increase slightly with decreasing bending radius, with the worst-case values of -36, -30 and -26 recorded for the SMF, 50 µm MMF and 100 µm MMF inputs, respectively, under the 2 mm bend. In all cases, the obtained crosstalk values were below -25 dB for all launches and all bending radii, indicating good performance even under tight bends and relatively overfilled launches.
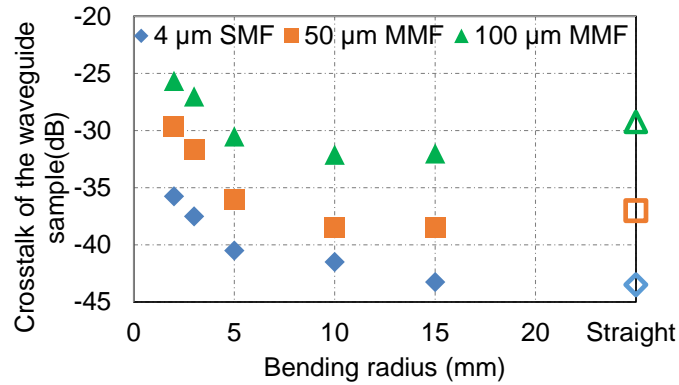
Figure 80 Crosstalk performance of the flexible waveguide sample when bending at different radii under different launch conditions. Results when waveguide sample was in straight condition are also indicated by unfilled markers.

The length effect on bent waveguide crosstalk performance also has been done. The shorter waveguides show similar behaviour to longer waveguides.

4.7.3 Experimental results of crosstalk performance of twists

The crosstalk performance of the twisted sample was also investigated using the same experimental setup. The obtained crosstalk values under three inputs are shown in Figure 81. Unlike the bends, the resulting curves for different numbers of full twisting turns were almost the same. The results indicated that twists do not have an obvious effect on the crosstalk performance of the waveguide. One reason for this is that long twisted waveguides have an excess twisting loss near 0, as mentioned in the twisting loss performance section. There is no loop involved and the light path is likely to be a straight line. All power is confined inside the waveguide and no extra power can be used to couple into adjacent waveguides. Therefore, the resulting twisted crosstalk performance is much better than bent waveguides. Figure 81 d) summarises the crosstalk values as a function of the number of full twisting turns for the different launch conditions studied. No significant difference in crosstalk performance was observed due to the waveguide twist with recorded crosstalk values ~ -40 dB for a well-aligned SMF and 50 μm MMF inputs and -30 dB for the 100 μm MMF input.
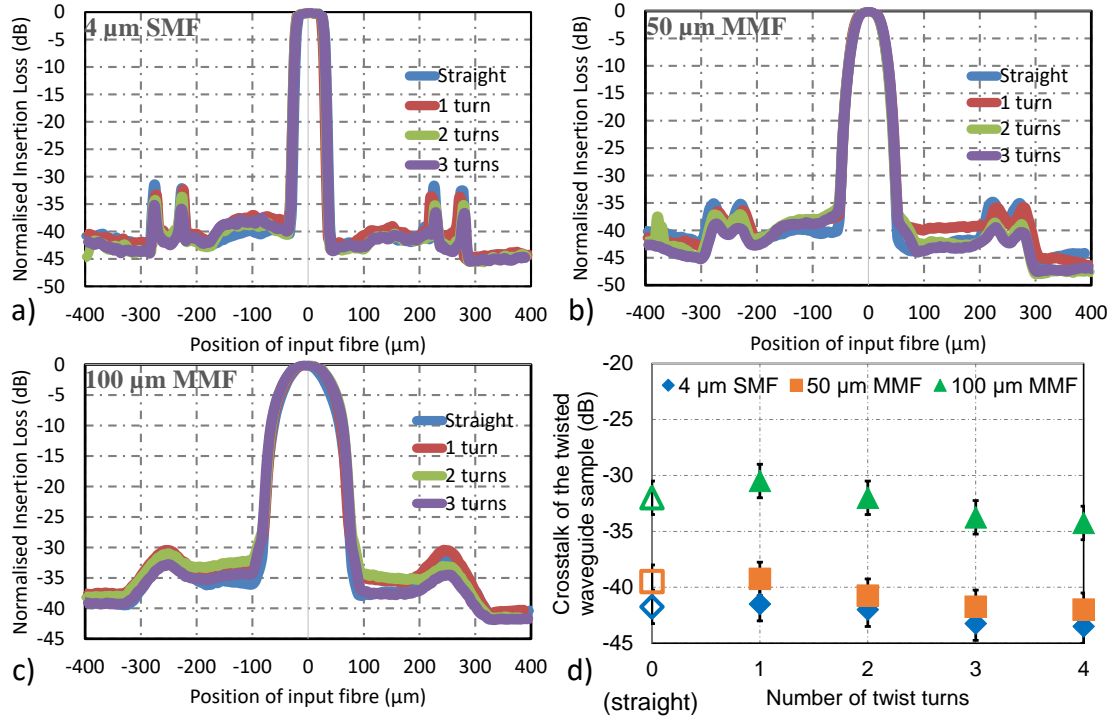
Figure 81 Normalised received power at the waveguide output as a function of the input position for different bending radii

a) SMF; b) 50 μm MMF input; and c) 100 μm MMF input. d) Summary of the crosstalk of a twisted sample for different

numbers of full twisting turns and the different launch conditions.

In conclusion, for bent waveguides the crosstalk values increased slightly with reduced bending radii, for twisted waveguides the crosstalk values mainly remained at the same level no matter the number of twisting turns applied. The measured results show that even under the worst performance case: at 2 mm bending under 100 MMF input, the crosstalk value was still below -25 dB, which is good enough for use in the real world.

4.8 Effect of dynamic bending of flexible polymer waveguide

Much previous work has been done on flexible polymer waveguides regarding bending, twisting and crosstalk performance. However, all experiments done have been based on flexible polymer waveguides in a static state, which means that waveguide sample is fixed at its position, and then measurements are carried out. In the real world, some waveguides need to work under a dynamic bending environment, providing a robust performance. Thus, in this section, experimental

measurements were taken in real time when flexible polymer waveguides were bending. The bending loss performance and bit error rates were obtained as a function of the stage moving speed. In addition, the standard deviation of the power fluctuation was also extracted based on the measured results.

4.8.1 System setup and moving path profiles

The system setup for measuring dynamic bending is shown in Figure 82. The 850 nm VCSEL was directly modulated using a pattern generator (Anritsu MP1800A) of 256 bits. Then the laser light was coupled into a 50 μm MMF input via a pair of $\times 16$ objectives. A free space variable optical attenuation (VOA) was placed in between objectives to change the input power as indicated in the figure. Similar to previous experiments, a cleaved fibre was used to do the end-butt coupling to the waveguide sample. In order to reduce the Fresnel loss and scattering loss due to surface roughness, index matching gel was applied at both ends of the fibre. On the output side, another 50 μm cleaved MMF was employed to collect the received power. In addition, in order to obtain the bit error rate and eye diagram, the oscilloscope, pattern analyser, and related units were also employed at the receiver end.
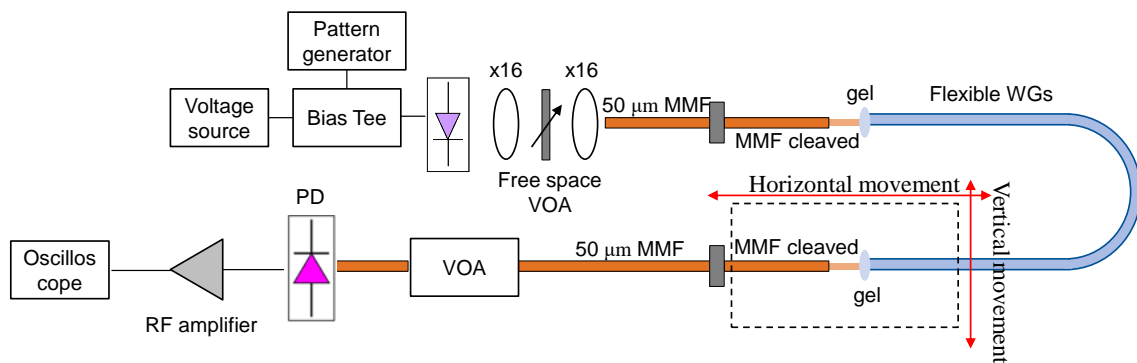
Figure 82 System setup for dynamic bending performance measurement. An 850 nm VCSEL was modulated by data via a bias tee. Then modulated laser light was coupled into flexible waveguides via a cleaved MMF. At the output side, the dashed sections were placed on a movable stage which can move horizontally and vertically. The corresponding power, bit error rate and eye diagrams were recorded.

The input section of system was fixed and did not move during the whole experiment, while the output section indicated by the dashed rectangle was placed on a movable stage and could move in the horizontal and vertical directions. A 24 cm long, 6 mm wide flexible waveguide was used and was

confined between two metal pads, see Figure 83. The confined waveguide sample shows a bent shape. By moving the output metal pad horizontally and vertically, the bending position and bending curvature could be changed, respectively.
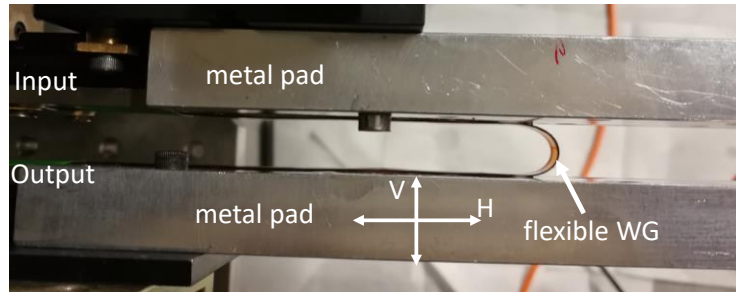
Figure 83 Image of flexible polymer waveguide confined by two metal pads in dynamic system setup. Pads employed here to confine the shape of bent waveguide sample.

There were two different moving path profiles, as shown in Figure 84. Path 1 scanned the horizontal direction first including forward and backward, and then reduced the vertical distance, repeating these steps until the bending radius reached its minimum allowed value. Path 1 investigated the effect of bending position when bending radius was fixed for each horizontal scan and only the position of the bends changed. Path 2 scanned the vertical direction first, including forward and backward as well, and then moved forward to a different bending position, repeating the same steps. There was no minimum bending radius limitation, and as a result, path 2 could run for dozens of cycles. Path 2 was employed to measure the dynamic bending loss caused due to bending radius.
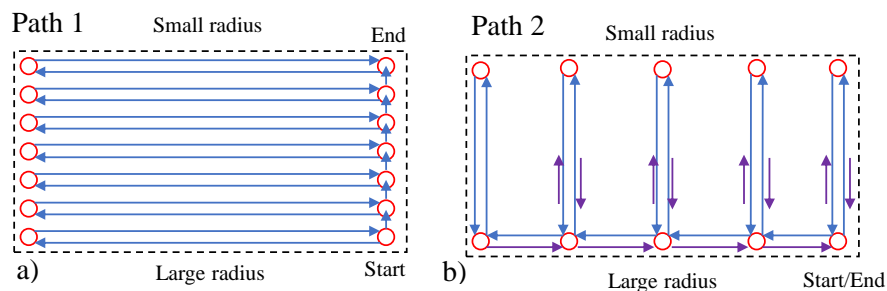
Figure 84 Stage moving paths for dynamic measurements. a): move horizontally first (bend position) and then move vertically (bend radius). b) move vertically first (bend radius) and then move horizontally (bend position).

The output power was collected in real time with the movement of the stage. The recorded normalised bending losses are plotted in Figure 85 based on their path profile. As can be seen, the power fluctuation was big when path 1 profile is used and there were very few high jumps during the measurements. However, aside from the results in the last column (smallest radius), almost all the excess bending loss values were less than 1 dB. In the path-2 profile, the resulting loss change was quite smooth and stable. It can be clearly observed that excess bending loss goes up with reduced radius and remains stable with the change of bending position.
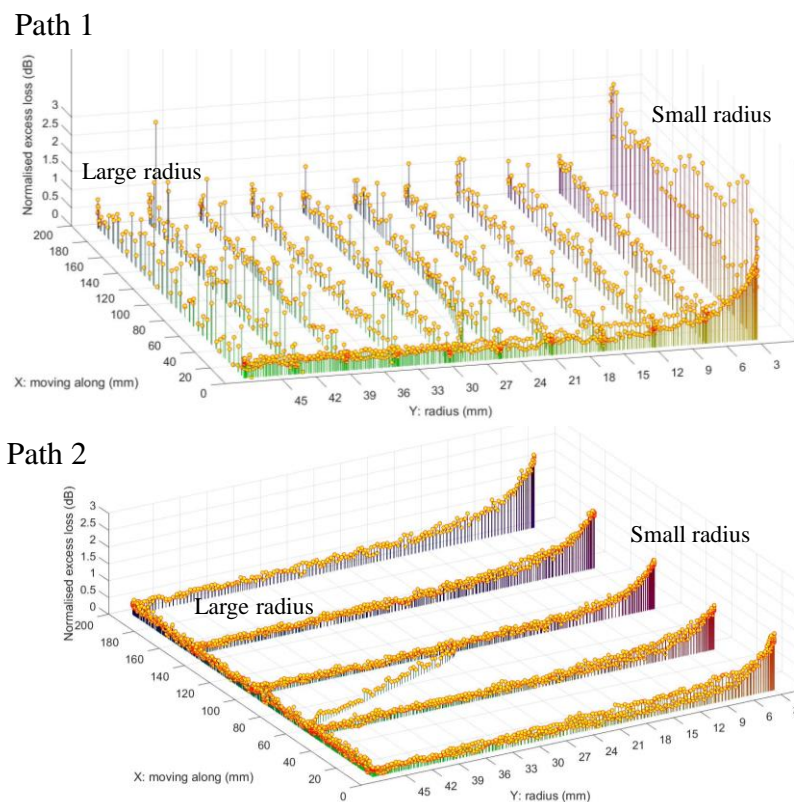
Figure 85 Normalised received power as a function of moving path profiles (path 1 and path 2).

4.8.2 Horizontal movement

Next, bending radius was set to be fixed and the stage only moved horizontally but at different speeds. During the experiments, the bending radius was set at 5 mm and the moving speed ranged from 0.5 mm/s to 16 mm/s. The received power was recorded for a large number of repetitions and normalised to its mean value. The corresponding histograms are also plotted to show their fluctuation, as shown in Figure 86.

92
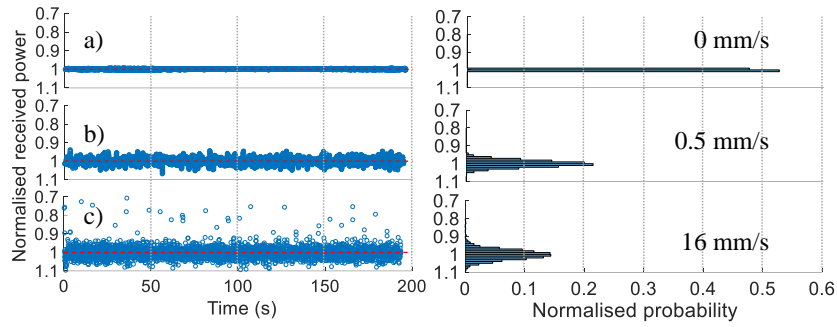
Figure 86 Normalised received power at the waveguide output over time and the corresponding histogram when (a) there is

no movement, (b) a slow (0.5 mm/sec) and (c) a fast (16 mm/sec) dynamic movement applied.

For reference measurement in a), when the waveguide had no movement, the received power was quite stable, and its histogram is very narrow. When the waveguide output side moved at 0.5 mm/s, the output power tended to fluctuate, which also can be observed from its histogram. As for 16 mm/s moving speed, the normalised received power became much more fluctuating and there were some peaks out of the normal range. Its histogram shows the worst power concentration. For each type of movement, the standard deviation σ of the output power variation was extracted and compared with the case when no movement was applied, and the results are shown in Figure 87. The fluctuation of power remained stable, and for all types of movements studied, robust operation was demonstrated with σ-values below 4% recorded in all cases.
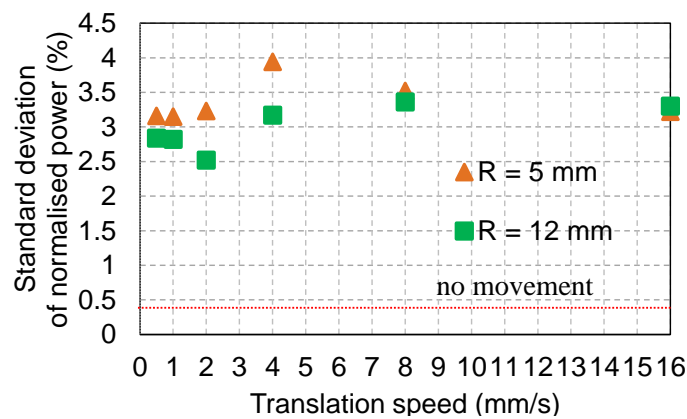
Figure 87 Obtained standard deviation values as a percentage of the mean value of the received power for different bending

radii and translation speeds.

4.8.3 Vertical movement

The bending position was set to be fixed, and the bending radius was changed repeatedly (vertical movement). A long-time (cycles > 200) measurement was carried out to test its robust performance. The results indicated that the flexible polymer waveguide performed very well after a long-time flexing. The recorded values are given in Figure 88. The left figure records the received output power in mW, the middle figure is the normalised received power, and the right figure shows the corresponding histogram. The results show that the power fluctuations for both low and high speeds were very similar, and there are some abnormal values in the high-speed movement, which is a similar result to that of horizontal movement.
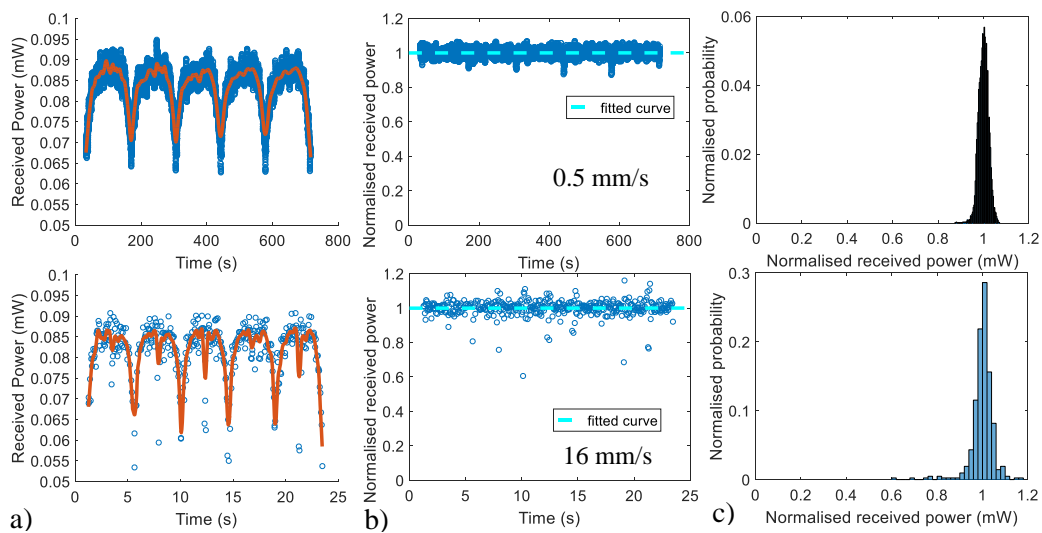
Figure 88 Vertical movement of dynamic bending measurement, a): received output power in mW, b): normalised output

power based on mean value and c): corresponding histogram.

The received power changed along with the change of bending radius, resulting in an "m" shaped curve, as shown in the figure above. The orange solid lines were fitted based on the average value. However, from previous experiments, the bending loss increases exponentially with a reduction in radius. Therefore, an exponential curve should be used to fit the curve. Figure 89 shows an exponential curve that fits the output power for periodic measurement.

94
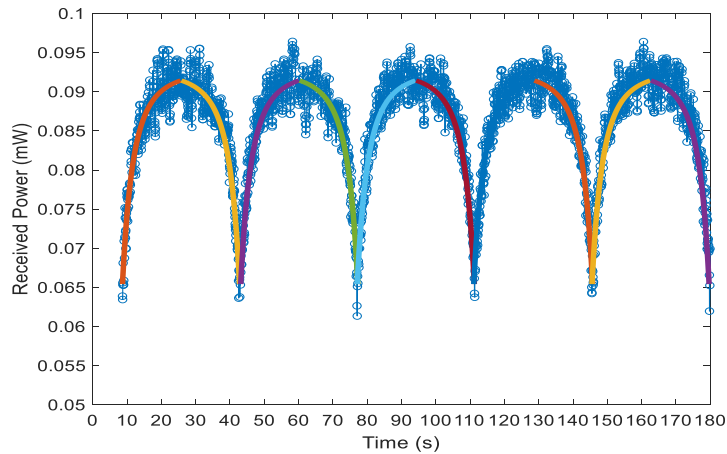
Figure 89 Vertical movement of dynamic measurement based on path 2, received power (markers) fitted using exponential

curves (colour solid lines).

The results can be well-fitted using exponential curves, and the fluctuation range is within 0.01 mW. Based on the new fitted curves, the standard deviation of the normalised output power was extracted for different moving speeds and is given in Figure 90. The standard deviation indicates an upward trend with increased moving speed. However, the σ-value is still below 3.5% under the speed of 16 mm/s.

Both horizontal and vertical measurement indicated that the power fluctuation inside the flexible polymer waveguides is small (<4%) under dynamic bending. In addition, the long-time measurements and flexing did not degrade the performance of waveguides, which also shows that flexible polymer waveguides are quite robust for use in the real world.
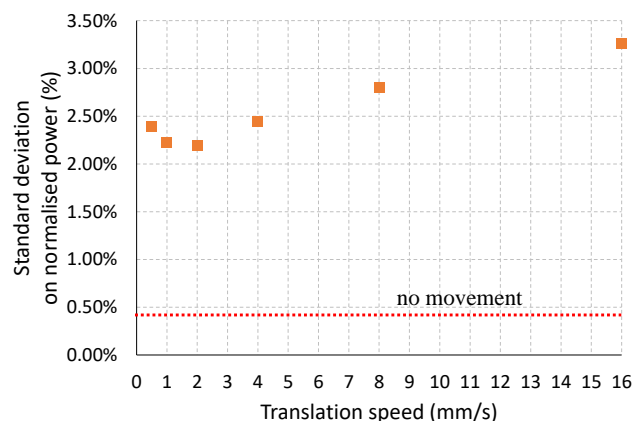
Figure 90 Obtained standard deviation values as a percentage of the mean value of the received power for different

translation speeds for vertical movement.

95

4.8.4 Bit error rate performance under dynamic bending

The bit error rate performance as a function of received power was also investigated under dynamic bending measurement. The transmission data rate was 25 Gbps based on the non-return-to-zero (NRZ) scheme, and the obtained results are plotted in Figure 91. For each measurement, the output received power was controlled to be the desired value: -0.5, -5.5 and -8 dBm using VOA. On the receiver side, both the power and bit error rate (BER) were recorded in real time.

Figure 91 a) shows that the initial received power set to be around -0.5 dBm and an error-free (error rate $< 10^{-12}$) rate for 25 Gbps transmission was achieved (Figure 91 a.2). Although, the power fluctuated during the dynamic bending, there was no influence on the error rate performance. Then, the received power was adjusted to around -8 dBm, and the corresponding BER was around 10^{-7}. Meanwhile, the BER change was quite symmetric with the received power change. In conclusion, dynamic bending does not change the BER performance as long as the received power is over a certain value, and a free error rate can be obtained. When the received power falls below the threshold, the BER increases linearly with the reduced received power and dynamic bending may result in a worse BER performance due to power fluctuation. Similar results will be discussed in Chapter 6.
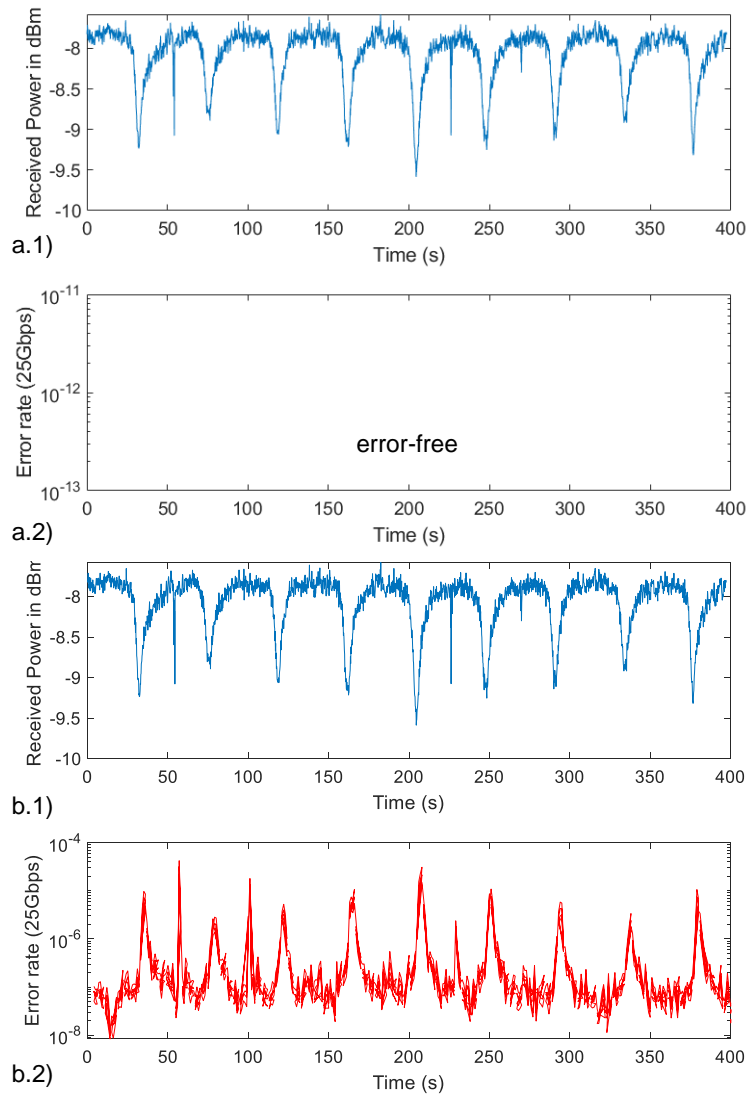
Figure 91 Bit error rate performance as a function of received power under dynamic bending measurement for 25 Gbps

transmission, a) received power was set to be -0.5 dBm and b) received power was set to be -8 dBm.

4.9 New proposed bend-insensitive polymer waveguides

A lot of work has been done on flexible polymer waveguides in terms of bending, twisting, crosstalk performance, and dynamic bending behaviour. As we can see bends play a very important role in the performance of flexible polymer waveguides. The last section noted that as long as there is enough output power at the output side, a high data transmission rate can be obtained easily with an error-free rate. Based on these previous studies, this section, proposes a new layout of

97

bend-insensitive flexible polymer waveguide. The result indicates that the excess bending loss is less than 1 dB under 50 μm MMF at a 2 mm bending radius, which is a great improvement.

4.9.1 Fabrication of bend-insensitive waveguides

The simulation of the air-exposed bend structure in Chapter 3.3.4, showed that the resulting excess bending loss was quite low due to the large refractive index difference between the core and the cladding material. However, there was no protection of the waveguide core for the air-exposed structure, meaning that the core channel can be easily contaminated by dust in the air or damaged by the outside environment. Thus, the best solution would be covering the core by a layer of cladding on top with a low refractive index material. However, the material with lowest RI is air. One alternative method is that the thickness of the top cladding could be reduced to few micrometres, so the waveguide core can still be protected. Meanwhile, due to the low thickness of the top cladding, the bending loss is still determined by the difference in RI of the waveguide core and air. Figure 92 compares this new layout of bend-insensitive structure with the traditional waveguide structure. Another bottom layer of waveguide is added to reduce the bending loss in case of different bending direction, and this bottom layer uses polydimethylsiloxane (PDMS) material that has a refractive index of ~1.41 at 850 nm.
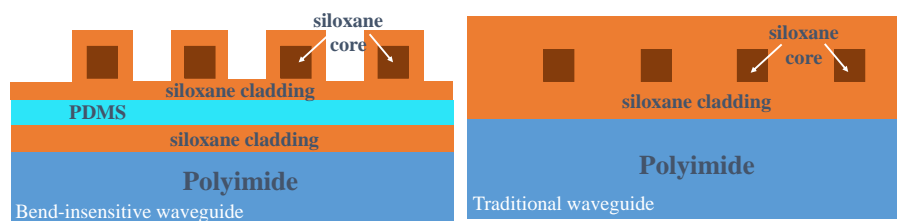
Figure 92 New proposed bend-insensitive structure of polymer waveguide as a comparison with traditional flexible polymer waveguides. New proposed waveguide has one extra layer (PDMS layer) and also has thinner top cladding.

The detailed steps for fabricating this new bend-insensitive waveguide are shown in Figure 93.

Step 1: The siloxane material is spin-coated on the surface of the polyimide substrate. The thickness of the siloxane cladding is fabricated to be ~ 5 μm and the substrate thickness is around 125 μm.

98

Step 2: After baking, the commercially available PDMS material (sylgard 184) is spin-coated (2500 rpm for 60 sec) on the top of the bottom cladding. Experiments have shown that PDMS material can be coated on the surface of siloxane material with a good adhesion. The thickness is ~20 μm. The sample is then baked for 10 minutes.

Step 3: During fabrication, the siloxane material can be spin-coated on the surface of PDMS layer but with poor adhesion. As a result, oxygen plasma is taken first on the surface of PDMS to increase its adhesion as oxygen plasma can deeply clean the top surface of PDMS. Then, siloxane material is spin-coated (3000 rpm for 60 sec) on top of the PDMS and the sample is baked for 3 minutes at 110 °C.

Step 4: Siloxane core material is spin-coated at 600 rpm for 60 seconds, to a thickness of 50 μm.

Step 5: Waveguide mask is put on the top of the waveguide core material.

Step 6: The whole sample is exposed to UV light and the waveguide core is cured.

Step 7: Using acetone to wash out the uncured core material, an air-exposed flexible polymer waveguide sample is made. The whole sample is baked to evaporate the acetone and IPA.

Step 8: Siloxane cladding material is spin coated on top of the waveguide core. The spin speed is set to be 2000 rpm for 60 seconds to get a very thin cladding protection layer. The new proposed bend-insensitive flexible polymer waveguide sample is then complete.

Compared to the traditional waveguide fabrication process, this new fabrication process only needs two more spin coating steps.
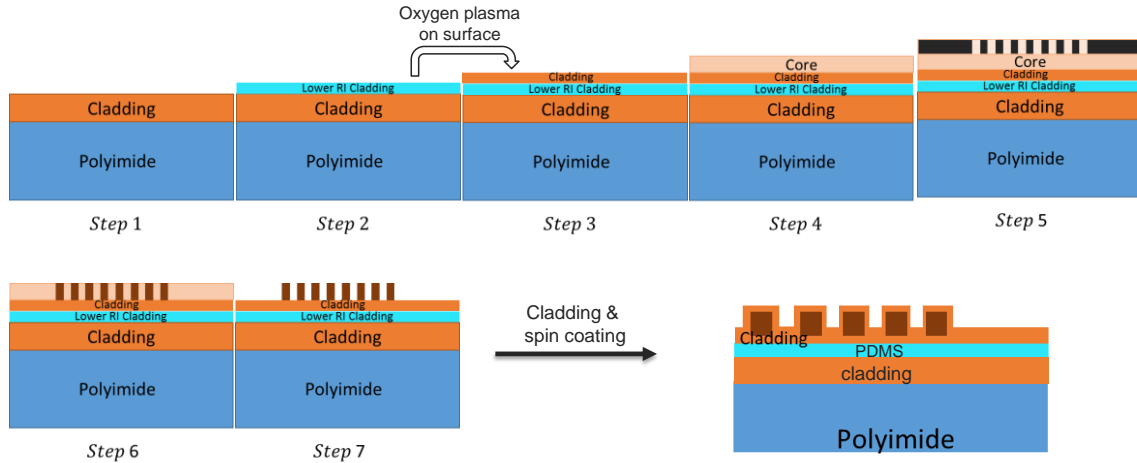
Figure 93 Fabrication steps of flexible polymer waveguides for the new proposed bend-insensitive structure.

Figure 94 shows the top and cross-section views of the fabricated new bend-insensitive waveguide. The waveguide is measured to be ~50 μm and the PDMS layer is ~ 20 μm. It is hard to observe the bottom siloxane cladding layer as it is covered by PDMS due to the dicing process. Obvious siloxane cladding tails are observed beside the waveguide core due to the fast spin-coating process. In the final step, after the fast spin-coating process, a very thin cladding layer is generated covering the waveguide core. However, due to the gravity effect, the un-baked liquid cladding material tends to accumulate at the bottom side, resulting in these cladding tails. Currently, there are no other good methods to remove these tails. However, the experimental results indicate that these tails do not degrade the bending performance of the waveguide.
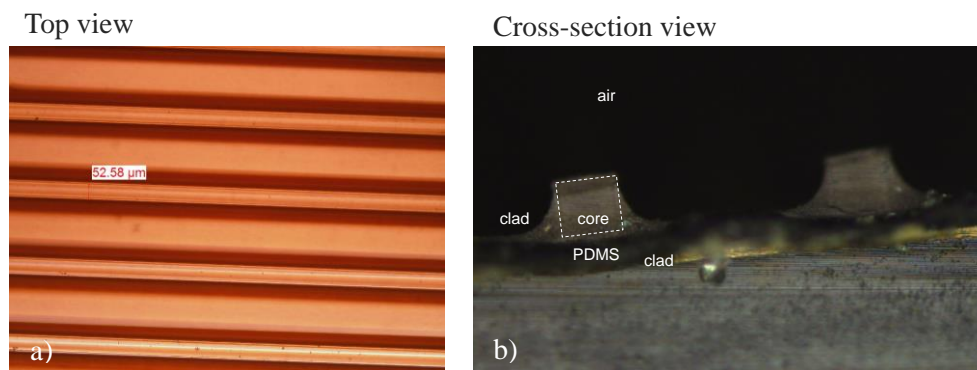
Figure 94 Top and cross-section views of bend-insensitive waveguide sample. a): top view, measured waveguide width is

52.58 μm. b): cross-section view, waveguide core is surrounded by a thin top cladding layer.

4.9.2 Performance analysis of bend-insensitive waveguides

Near-field images of the bend-insensitive waveguide facet were recorded, and they are shown in Figure 95 under different launch conditions at 850 nm wavelength. As can be seen, below 50 μm MMF input, the laser light was confined inside the waveguide core due to the existence of the siloxane cladding, while for the 100 μm MMF launch, the majority of the power propagated in the waveguide core with the rest confined to the siloxane cladding areas. Because the diameter of the 100 μm MMF was larger than the waveguide core, some power was injected into the cladding. Due to the air coating outside, another waveguide (siloxane cladding and air) channel was formed.
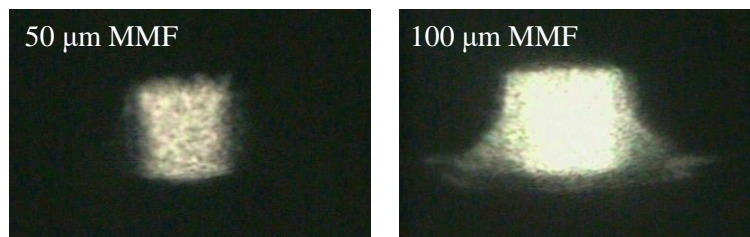
Figure 95 Near-field image of the bend-insensitive waveguide facet under 50 μm MMF and 100 μm MMF input launches.

Bending loss measurement was taken for the new waveguide. Due to the asymmetry of the waveguide structure, different bending directions were applied. The excess bending loss results for different bending directions were compared with a traditional waveguide and are given in Figure 96 under 50 μm MMF input. The results of the traditional waveguide are plotted in triangle markers and the new results are shown using filled and unfilled square markers. When the polyimide substrate (PDMS) faces the outer direction of the bent waveguide, this resulting bending structure is named as structure 2 (MMF50_PDMS). and vice versa for structure 3 where the air cladding is the outer layer of the bent waveguide.
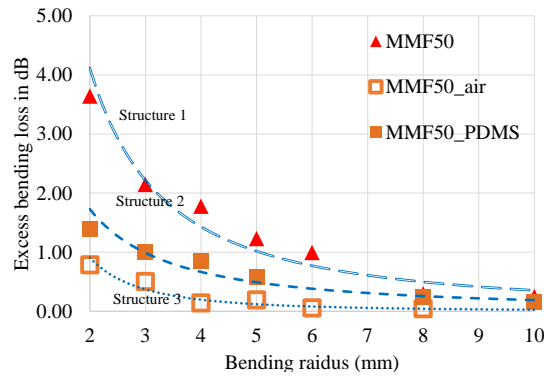
Figure 96 Excess bending losses of bend-insensitive waveguide facing different directions in comparison with traditional waveguide. Loss performance of tradition waveguide is indicated by triangle markers. MMF50_air (unfilled rectangular markers) means that thin top cladding layer facing outside when bending the waveguide while MMF50_PDMS (filled rectangular markers) means that thin top cladding layer facing inside during bending.

The results show that excess losses of the traditional waveguide are much higher than the new waveguide, especially compared with the unfilled markers. When the new waveguide was bent towards the PDMS layer, the excess losses lie between the other two curves. This is a great improvement for the new bend-insensitive structure of the waveguides. The measured excess bending loss was less than 1 dB even when bending at 2 mm under 50 μm MMF launch. The rest of the results for bending losses under 4 μm SMF and 100 μm MMF input were also carried out and are given in Figure 97.
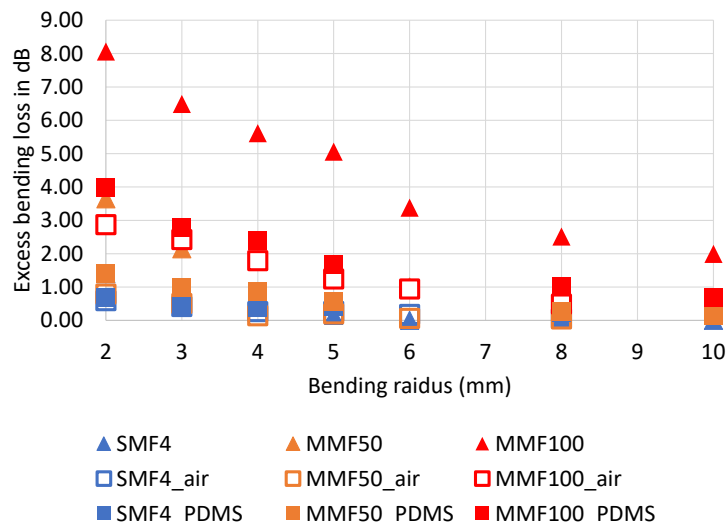
Figure 97 Excess bending losses of the bend-insensitive waveguide for different bending directions in comparison with a traditional waveguide under all three input launch conditions.

102

In conclusion, below 100 μm MMF input, a great decrease in bending loss was observed for the new waveguide. As for 50 μm MMF, the resulting losses were still much better than traditional waveguides. For the restricted launch (4 μm SMF), this improvement was not obvious as the resulting bending losses of both waveguide samples were quite small and can be neglected.

Chapter 5 Analysis of mode coupling in flexible polymer waveguides

The waveguide performance obtained relies on both the mode excitation at the waveguide input and the evolution of the mode power distribution along the length of the waveguide. The latter contains two behaviours: mode loss (coupling to radiation modes) and mode mixing (coupling to other guided modes). In the experiments, the excess loss (the difference in insertion loss from the reference measurement) indicates the amount of additional mode loss induced in the waveguides, while the 5% far-field angle (FFA) characterises the output beam divergence angle and indicates the amount of power coupled to higher order modes at the waveguide output (mode mixing). In this chapter, both excess loss and 5% FFAs are measured to analyse the mode changes inside the waveguide. Mode coupling effects caused by the existence of small bends and micro bends are studied. Surface roughness scattering, the main factor dominating the mode mixing scheme for the straight waveguide, is then investigated. Waveguide samples used in this chapter are provided by Dow Corning company which were shown in Figure 50 (not the new proposed bend-insensitive polymer waveguide samples).

5.1 Mode coupling effect due to small bends

As shown in previous investigation, bends indicate the potential suppression of higher order modes inside the waveguides. However, a 180° bend cannot show an obvious effect. In this section, several full bending turns ($N \times 360°$) are applied to the flexible waveguide and both power losses and far-field distribution are recorded. The system setup is shown in Figure 98, which is the same that used for bending loss measurements. The flexible polymer waveguide was wrapped around a mandrel for different numbers of turns and the far-field measurement is taken at the output side. The setup can be found in Figure 52. Figure 99 shows an image of the wrapped waveguide setup in the experiment. The flexible polymer waveguide is illuminated with red light and several bending turns can be clearly observed.
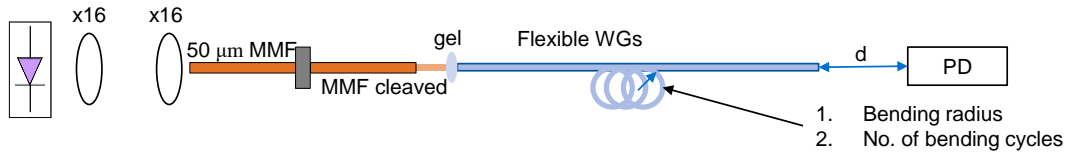
Figure 98 System setup for the small bends effect on flexible polymer waveguides. Waveguide sample was bent by several number of turns.
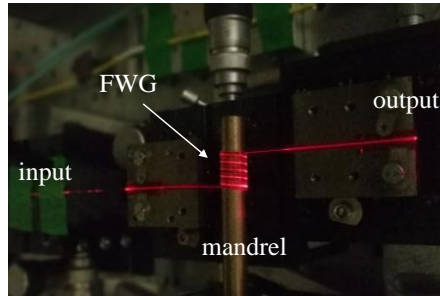
Figure 99 Experimental setup for the small bends effect on a flexible polymer waveguide which is illuminated with red laser light. Here, waveguide sample was bent by 5 turns.

The waveguide used in this work were 24 cm long and 2 mm wide. Three mandrels with different radii of curvature were employed (5, 6 and 8 mm) and tests were carried out using a varying number of full turns around the mandrel (0 to 3, 360° each). Three input launch conditions: 4 μm SMF, 50 μm MMF, and 100 μm MMF with mode mixer were employed as well. The excess bending losses are indicated in Figure 100. Due to the limitation of waveguide length, it was not possible to test three bending turns on an 8 mm radius mandrel.
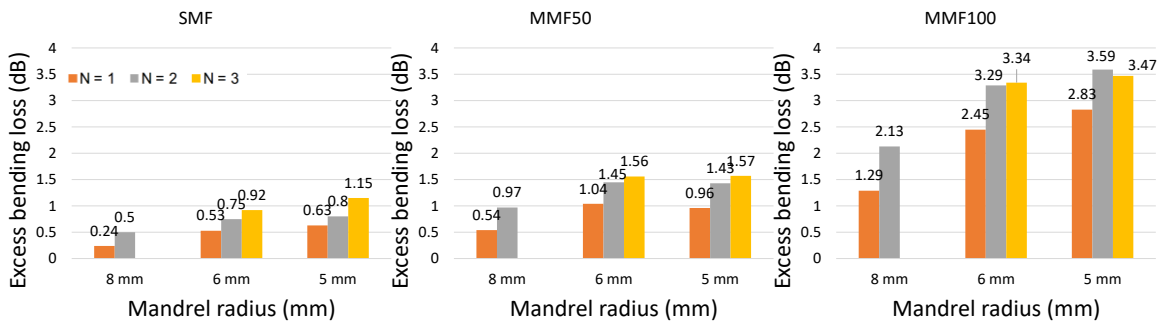
Figure 100 Excess bending losses of a flexible polymer waveguide for the small bending effect under three different input conditions. Mandrel radius is set to be 5 mm, 6mm and 8 mm. Bending turns is chosen from 1 to 3.

From the results, as expected, excess bending losses increased with the number of turns applied and the smaller radius employed. Details of the bending loss effect can be found in Chapter 4. These losses in waveguide power are caused due to the mode losses (radiation modes) inside the waveguide. However, how the mode mixing behaves inside the waveguide due to small bends cannot be obtained from these excess loss results. Thus, the 5% far-field angles (FFAs) were measured and recorded at the same time, as shown in Figure 101.
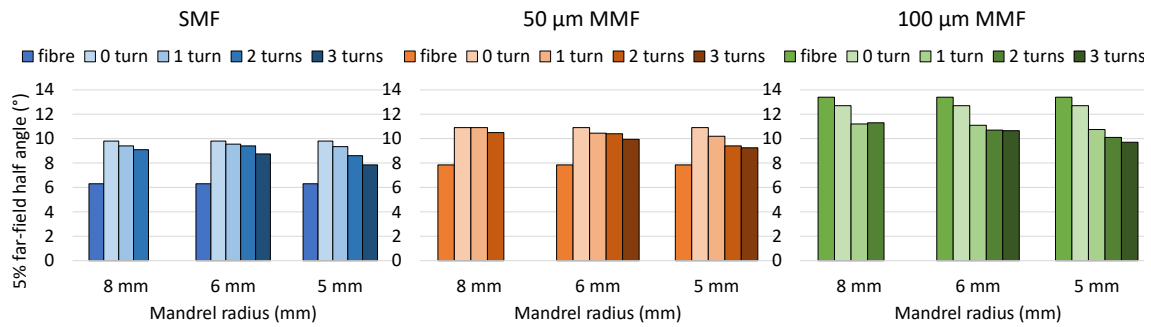
Figure 101 5% FFAs of the emitted beam at the waveguide output under different bending radii and turns and different input launch conditions.

The first bar in each plot shows the 5% FFA of the input fibre. As can be noticed, the number of modes significantly increases under the 4 μm SMF and 50 μm MMF inputs when the fibre modes launch into polymer waveguide exciting waveguide modes for the straight waveguide. As for 100 μm MMF input, the number of modes in the fibre with mode mixer is much larger than that of the waveguide accommodated modes, therefore, a decrease was observed. In the subsequent wrapping process when the waveguide sample was wrapped in 1, 2, 3 turns, the 5% FFA results show a consistent trend for all inputs. Longer bends (large numbers of turns) result in a reduced far-field profile, which indicates a reduced percentage of power carried by the higher order modes at the waveguide output. This means that the power carried by the higher order modes is suppressed due to the wrapping rather than being enhanced via mode mixing. Similarly, a smaller bending curvature also has the same effect on the waveguide modes. Figure 102 shows that the suppression of higher-order modes means that the output power distribution is narrower than before (reduced modal dispersion), thus a better bandwidth performance could be obtained. However, a small bending curvature and long bending distance will result in a big excess loss, which will degrade the bandwidth

performance as there is not enough output power for the photodetector to detect, see Figure 91 for more details.
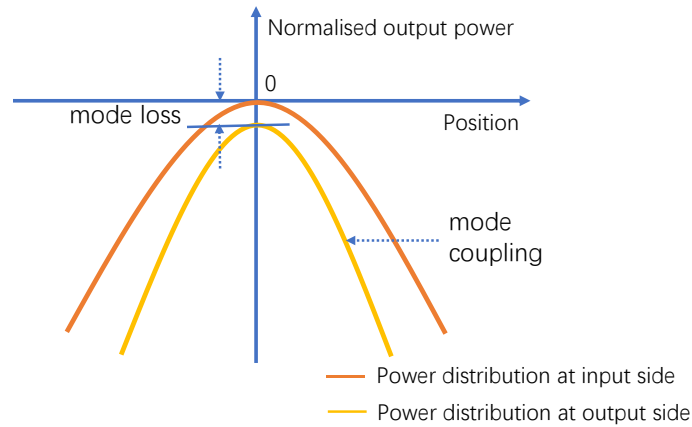
Figure 102 Schematic diagram of mode loss and mode coupling schemes. Mode loss refers to the total power loss while mode coupling refers to the coupling process between different modes. Power reduction for a specific mode is consist of mode loss and mode coupling.

5.2 Mode coupling effects due to micro-bends

A similar experiment was done to investigate the micro-bends effect on the flexible polymer waveguide. A commercially available fibre mode scrambler (Newport F-1) was introduced here to squeeze the waveguide. It has a pair of corrugated surfaces ("teeth") to apply a micro-indentation to the fibre core. Details of the mode scrambler and an image of the real scrambler are shown in Figure 103. The teeth period was 1.1 mm [140]. During the experiment, the middle part of the waveguide sample was inserted into the mode scrambler, and the separation distance Δx was adjusted as indicated on the figure.
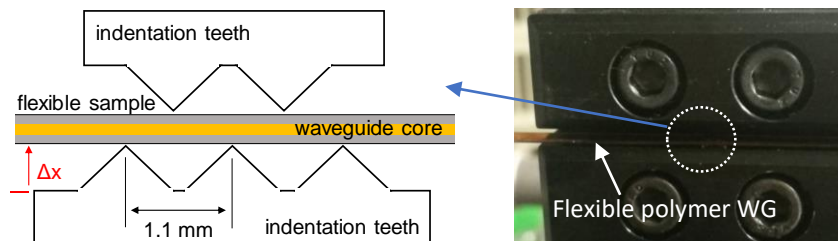
Figure 103 Schematic diagram of mode scrambler and an image of the system setup for micro-bend measurement. Force is applied on the waveguide due to the squeeze of teeth, generating micro-bends.

The measurement began when the teeth just touched the waveguide surface, and this separation distance value was defined as 0. It should be expected that there is an optimum tooth separation that promotes mode mixing, as a large separation has little effect on the light propagation in the waveguides while a small separation will cause significant excess loss due mode losses. Both excess losses and the 5% FFA were measured under 4 μm SMF and 50 μm MMF launch conditions, and the corresponding results are shown in Figure 104.
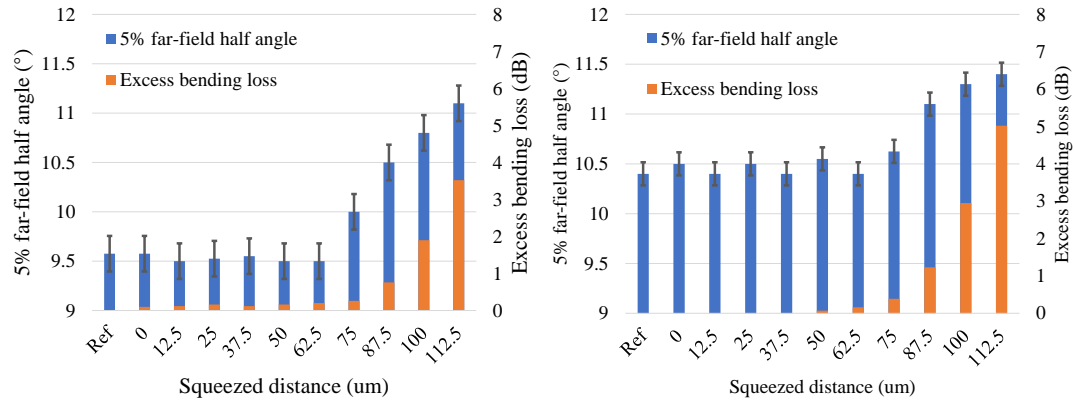
Figure 104 Obtained 5% FFAs and excess losses for the 24 cm long waveguide as a function of the reduction in separation distance between the indentation teeth under 4 μm SMF (left) and 50 μm MMF inputs (right)

The values obtained from the waveguides when the mode scrambler was not used are also shown for comparison, named as "Ref" value. The figure shows that reducing the tooth separation results in an increase in the 5% FFA and excess losses for both launches, which indicates that both mode mixing and mode loss are promoted due to the micro-bending. A reduction of 75 μm in the tooth separation resultant in an increase in the far-field beam divergence with a small increase in insertion loss of ~0.2 dB and ~0.3 dB for the SMF and MMF inputs, respectively. Separation values Δx above 87.5 μm resultant in even larger output beam profiles but also in larger excess losses above 1 dB for the MMF input. The obtained results indicate that micro-bending is more efficient in promoting mode mixing in such waveguide systems, and can be used in real-systems to ensure a more uniform power distribution at the waveguide output. This can be beneficial for avoiding modal noise in such systems [141, 142] or for ensuring uniform splitting at Y-splitters and couplers [20, 135, 143].

Near-field images under both input launches were also recorded during the experiments and those figures are given in Figure 105. Mode losses can be roughly estimated from the brightness of

the images. The near-field pattern tended to vanish when separation distance was over 87.5 μm. The mode coupling during propagation can also be estimated from the change of light concentration at the waveguide output side. An obvious mode coupling effect due to micro-bends could be observed when the 50 μm MMF input launch was employed. When there was no micro-bend applied (Ref or 0), the majority of power concentrated at the bottom area of the waveguide. However, after squeezing the mode scrambler by 100 μm (introducing micro-bends), the distribution of power inside the waveguide seemed to be quite uniform, which indicates that light power located in the bottom area (lower order modes) was coupled into the outer core area of the waveguide (higher order modes).
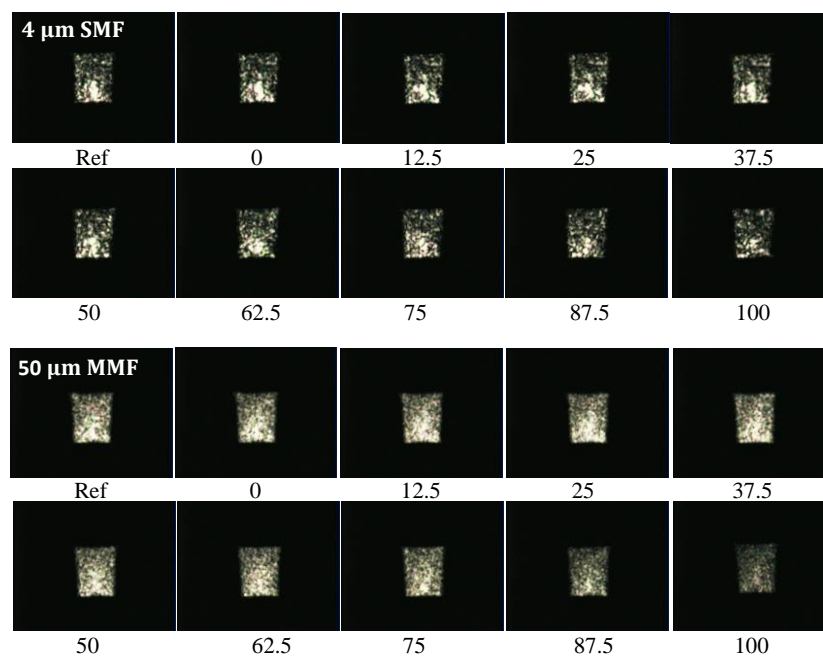
Figure 105 Near-field images of flexible polymer waveguide outputs as function of different squeezing distances under SMF and MMF inputs.

Compared to small radii bends, both micro-bends and small bends result in mode losses during the propagation inside the waveguide. As for mode coupling, small bends have a suppression effect on higher order modes along the waveguide propagation. A longer length and a smaller radius of curvature will enhance this mode filtering effect. Micro-bends cause mode mixing during light propagation, as higher order modes are excited when lower order modes encounter micro bends during propagation.

5.3 Surface roughness effect

The waveguide surface roughness effect is mainly dominated by the sidewalls, and it is characterised by its root-mean squared (rms) value σ_{rms}. [144] indicates that the sidewall roughness of multimode waveguides fabricated using the same siloxane materials is measured to be around 40 nm in σ_{rms}, which satisfies low loss propagation ($< \lambda/10$). This section discusses in detail the surface roughness effect, including power loss and the mode mixing effect.

5.3.1 Propagation losses due to surface roughness

A simulation model was developed using ZEMAX software to simulate propagation losses. The system setup is shown in Figure 106. A 50 μm MMF input was used as a simulated light source and 1 million rays were set during the simulation.

50 μm MMF input   photodetector

Figure 106 Simulation of propagation loss due to surface roughness, waveguide core sidewalls were set to be rough. Power at input and output sides are recorded.

The surface roughness was set to be from 10 nm to 50 nm in ZEMAX, and the waveguide length ranged from 1 cm to 7 cm. Due to the nature of the simulation software, all the walls of waveguide core were set to be rough. The simulation results are plotted in Figure 107. The split function is on in the right figure, which means that one single ray will scatter into five reflected rays after hitting the rough surface and those five reflected rays will generate 25 rays for next hit in total. On the left figure, only one main reflected ray is collected and as a result, there is a slightly higher propagation loss.
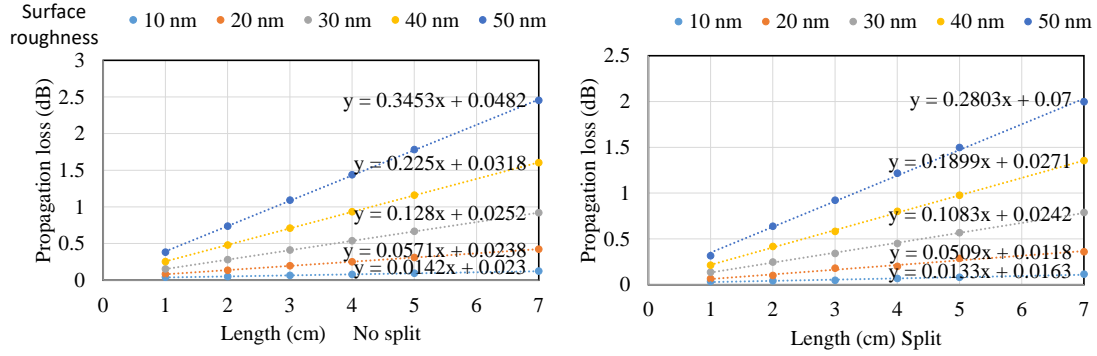
Figure 107 Simulation of propagation losses as a function of waveguide length due to different surface roughness. Slope

values are the propagation losses and inception values are coupling losses (almost 0).

The slope values are the propagation losses per centimetre of the waveguide for different surface roughness, assuming that all the waveguide walls are rough. A rougher surface will result in a bigger loss, and the incremental loss also increases. From the results, if 40 nm σ_{rms} is set, the resultant propagation loss is ~0.11 dB/cm which is bigger than the real waveguide sample (~ 0.04 dB/cm). The reason is due to the rest of scattering rays not being collected and some light rays below the minimum threshold values not being traced in the software.

5.3.2 Single ray response of waveguide rough surface

The ABg scattering model in ZEMAX was employed to describe the ray scattering at each reflection on the core-cladding boundary [145-147]. As for the single ray response, a single ray with a designed angle θ_i was injected onto a rough surface and the scattered output rays were recorded and named as the single ray response. The following figure shows the scattering process [148] of a single ray response. The figure does not consider the transmitted plane waves for the total internal reflection in the waveguide.
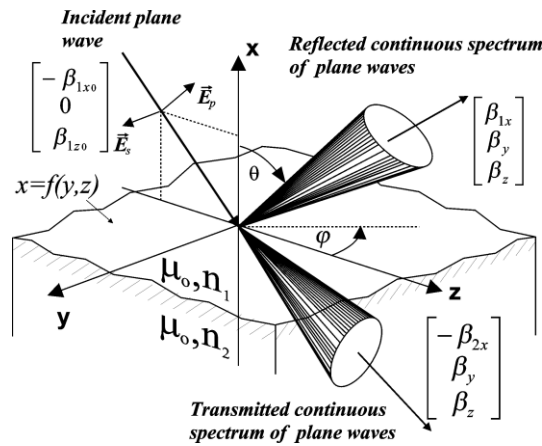
Figure 108 Geometrical arrangement to describe a local scattering event at a rough surface [148]. When ray hits the rough surface, both reflected scattered rays and transmitted scattered rays are generated.

The reflected rays can be divided into two groups: guided rays and radiated rays. All the radiated rays contribute to the waveguide loss (propagation loss) and the guided rays are further traced along the waveguide length to determine the ray power distribution at the waveguide output. The following figure shows a single ray output response, assuming that the incident ray angle is 5°, for an example. As for the output response, the reflected ray with a 5° angle retains the majority of its power (~0.999) and the rest of power is coupled into other rays with different angles, according to the mode coupling. The power level of each coupled ray is around 10^{-5} and the sum of all reflected rays is not 1. The lost power part is the propagation loss (dB/hit). The later calculation can transfer the unit of propagation loss from dB/hit to dB/cm according to the incident ray angle.
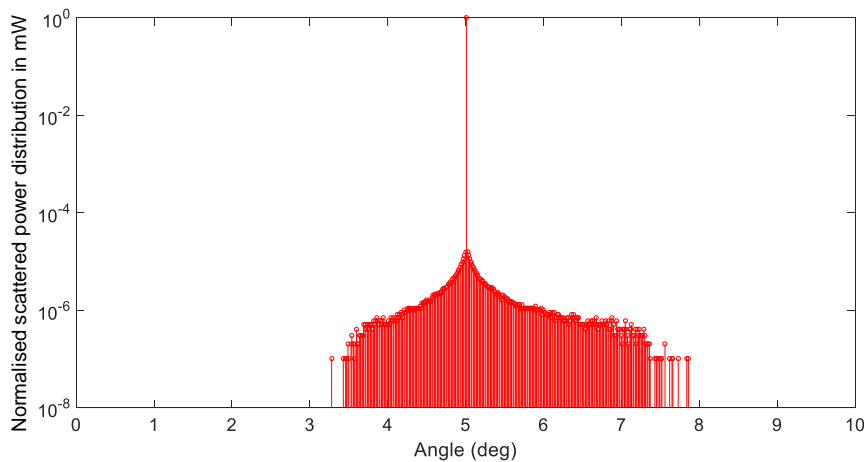
Figure 109 Example of single ray response of scattered ray, incident ray angle of 5°. A single incident ray is scattered into hundreds of sub rays after hitting rough surface.

112

The relation between the *ABg* model parameters and the surface roughness parameters can be found in [149]. For a given surface roughness, the values of the *ABg* model parameters determine the strength and shape of the scattered rays at the reflection boundary (core-cladding boundary). The following figure summarises the effect of each *ABg* parameter to the scattered ray response.
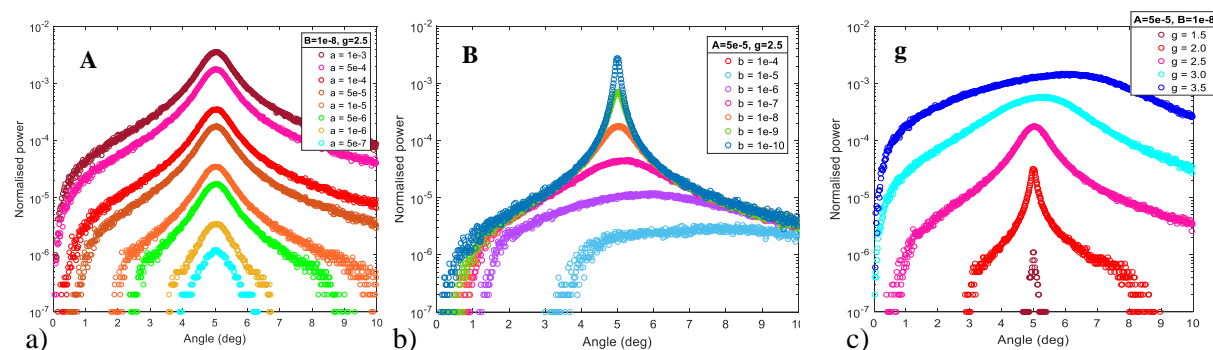
Figure 110 Scattered ray responses due to the change of ABg parameters, a) change of parameter A, b) change of parameter B and c) change of parameter g.

In order to see the mode coupling effect clearly, the main reflected ray with the majority of power is removed from the figure and then y-axis can be scaled to a proper range for the response. It can be noticed that parameter A only changes the level of response, but could not change the shape, which means that the reflected rays have the same distribution profile but at different absolute values. Parameter B changes the response distribution, in that a larger value of B will result in a broader output response (a more uniform response). The power becomes much more concentrated near the input rays with similar angles by employing a smaller value of B. Parameter g has a similar effect as parameter B, but the generated uniform response has a much higher power level. Many simulations have been done to validate this model with realistic values for the surface roughness and loss performance. Finally, the parameters A, B and g are reasonably chosen to be 5.5×10^{-5}, 1×10^{-8}, and 1.8, respectively, to simulate the surface roughness of $\sigma_{rms} = 50\ nm$.

Based on the ABg values above, a step-index RI profile was assumed for the waveguide, and the angle of incident ranged from 0.01° to 8° with a step of 0.01° in order to simplify the analysis. The following figure indicates the ray power loss coefficient (power coupled to radiated rays) and power reduction (power coupled to both guided and radiated rays) as a function of the incident angle of the

guided rays, and an example of the obtained ray coupling coefficients (ray response) for two different single incident rays with θ_0 of 2° and 6°.
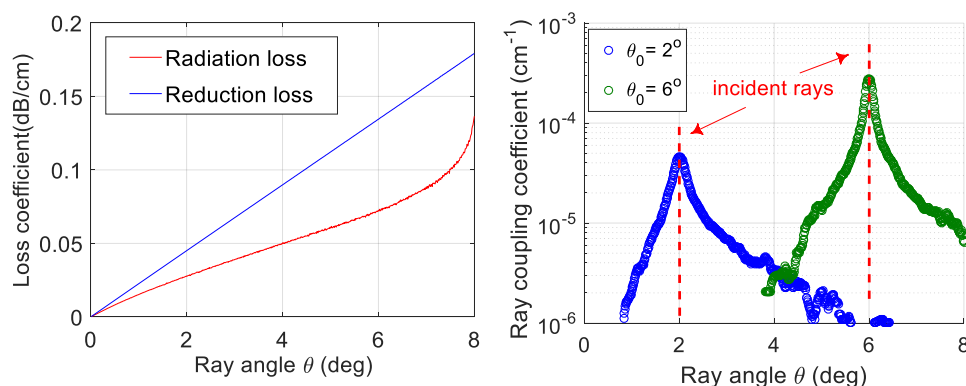
Figure 111 Radiation and reduction loss coefficients as a function of propagation angle θ due to the surface roughness and ray coupling coefficients for the reflection of a single incident ray of unit power at two different θ angles [150].

The ray coupling coefficients can be well fitted with exponential curves (see Figure 112) which is in agreement with the literature and obtained via the electromagnetic theory assuming an exponentially decaying surface roughness correlation function [151, 152].
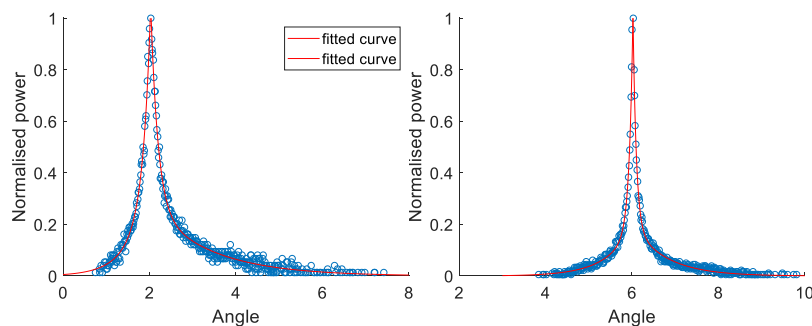
Figure 112 Ray coupling coefficients for the reflection of a single incident ray at two different angles fitted by exponential curves (red lines) in linear scale.

During the simulation, the launch condition was employed by using the same size and the output beam profile as SMF input. The evolution of the ray power distribution (Gaussian profile) along the waveguide length can be characterised by the following equation:

$$\frac{dP_\mu}{dz} = -2\alpha_\mu P_\mu + \sum_{v=1}^{N} h_{\mu v}(P_v - P_\mu)$$

114

where P_μ is the ray power at a specific angle θ_μ, α_μ is the ray power reduction loss (power loss of mode μ itself), $h_{\mu\nu}$ is the ray power coupling coefficient for the ray at angle θ_μ due to the propagation of a ray at an angle θ_ν, and z is the propagation distance. For the single ray response simulation, once we have obtained α_μ and $h_{\mu\nu}$, we can derive the next input light rays after the distance dz. By repeating above two steps, the whole propagation paths and power distribution can be extracted. Figure 113 shows the propagation loss and evolution of the ray power distribution after propagation up to a 100 cm long waveguide when an input beam with Gaussian ray power distribution with a standard deviation of 2.5° is assumed. It can be noted that the ray loss is dominant over ray coupling and the output power distribution shows a decreasing trend along the waveguide length.
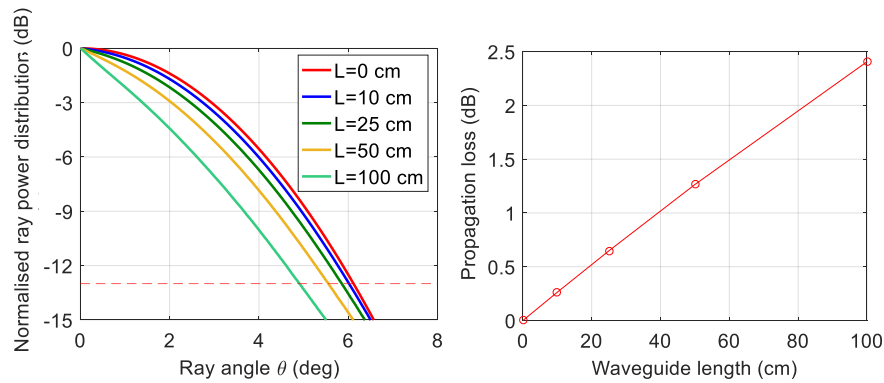
Figure 113 Simulated ray power distribution and propagation loss for different waveguide lengths for a Gaussian ray input

power distribution with a 2.5° standard deviation [150].

The single ray response simulation showed that the strength of mode mixing due to surface roughness is not obvious enough. Mode loss dominates the power distribution along the waveguide length. Higher order modes (rays with large incident angles) experience larger losses than lower order modes (rays with smaller incident angles). Cutback measurements on the 24 cm long waveguides were taken to confirm this observation.

5.3.3 Cutback measurements of the scattering effect on a 24 cm long waveguide

According to the simulation of the single ray response, surface roughness dominates the mode losses along the waveguide length. In this section, an experiment was carried out to observe this phenomenon. The waveguide sample employed was initially 24 cm long and 6 mm wide. The system

setup for far-field measurements was the same as the one used in section 4.2, and a simple schematic is given in Figure 114.
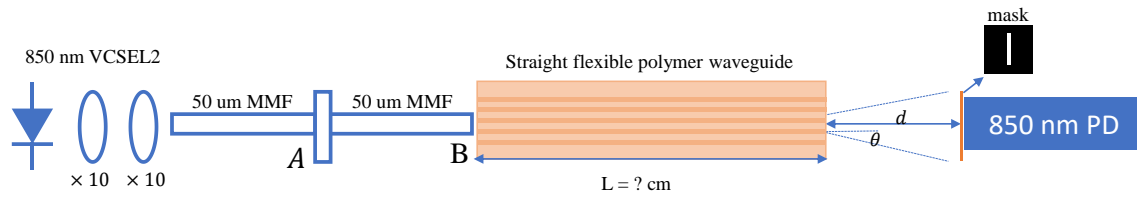
Figure 114 System setup of 5% FFA measurement. Waveguide samples with different lengths were employed. At the output side, far-field distributions were measured.

No polishing step was taken on the facets of the waveguide, but index matching gel was used at the input side during the measurements. The far-field profiles of a 24 cm straight waveguide sample were measured first and then this sample was cut into 2 pieces: 4.9 cm and 15.8 cm. The following far-field profile measurements were carried out based on these three sub-samples. As before, three different input launch conditions were employed to simulate the different excitations of waveguide modes at the input side. At least three waveguide channels were measured, and the averaged values are obtained. The 5% FFAs results of the waveguide samples with different lengths are given in Figure 115.
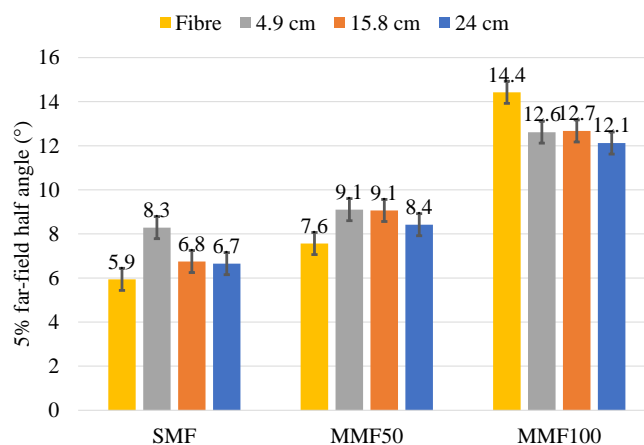
Figure 115 5% FFAs of straight flexible polymer waveguide samples for different lengths under different launch conditions.

The results confirmed the conclusion inform the single ray response simulation. For a longer waveguide, mode loss is dominant over mode coupling as a longer waveguide sample results in a

116

smaller 5% FFA. This conclusion works well no matter which input launch condition is employed. However, the main drawback of using this system setup is that the measured far-field distribution is strongly dependent on the uniformity of the waveguide output facet. A rough facet may have a large variation in the resulting 5% FFA. Therefore, in order to double confirm the conclusion, another method was used to re-measure the far-field profiles of the waveguide outputs: the ISO 11146-1 standard based beam divergent angle measurement.

5.3.4 ISO 11146-1 standard beam divergent angle measurement

In this section, a new far-field measurement was introduced with a smaller error range. Far-field profiles of waveguide output beams for different lengths were measured under different launch conditions. These new measurements were done to double check the mode coupling and mode loss behaviour along the waveguide length caused by surface roughness. The details of the new far-field measurement setup can be found from in the ISO 11146-1 standard [153]. Figure 116 shows a divergent beam. The idea of this method is to capture different images of the output beam at different propagation distances. Then, the divergent angle can be calculated based on the effective diameter and standard deviation of the output beam profile.
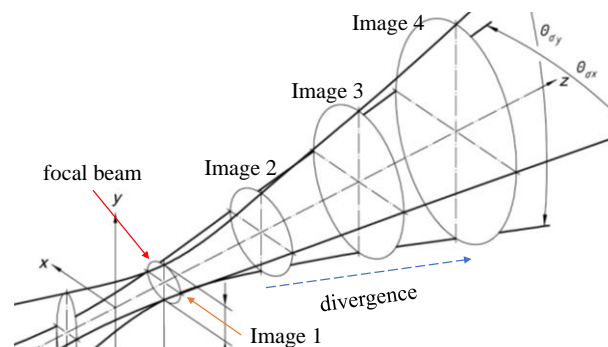
Figure 116 Schematic of a divergent beam [153]. Bean width is the smallest at focal plane.

The system setup is shown in Figure 117. All the setups prior to the waveguide output were the same as the previous FFA measurement setup. On the output side, a $\times 16$ objective was used to focus the output beam onto a CCD camera. The beam images and corresponding propagation distance (Z) were recorded in the computer and propagation distance (Z) was defined as the distance from waveguide focal plane to the position of $\times 16$ objective. For the focal plane, the propagation distance was regarded to be 0, ($Z = 0$). Then both the objective and camera were moved slightly

away. The new divergent image and new position were recorded again. The captured image is the divergent beam profile of the waveguide output. The above steps were followed until ten more images were recorded.
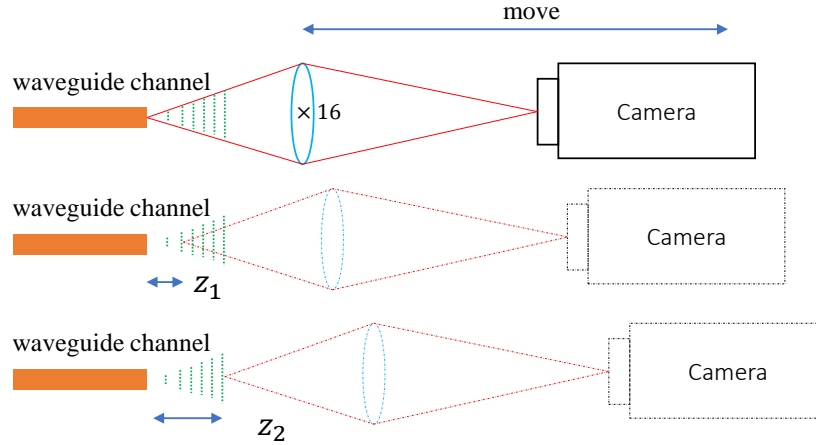
Figure 117 System setup for measuring far-field profile based on ISO 11146-1 standard. Un-focused near-field images at different positions together with focused image at focal plane were recorded.

Some captured output beam profiles along propagation distance are shown in Figure 118 by employing a 50 μm MMF fibre.

Figure 118 Captured images of 50 μm MMF output beam profiles along the propagation distance.

The first and second order moments of a power density distribution are needed to calculate the effective diameter of a capture beam profile, and their equations are given below.

1st order moments:

$$\bar{x}(z) = \frac{\int_{-\infty}^{\infty} \int_{-\infty}^{\infty} E(x,y,z)x \, dxdy}{\int_{-\infty}^{\infty} \int_{-\infty}^{\infty} E(x,y,z) \, dxdy} \qquad (69)$$

$$\bar{y}(z) = \frac{\int_{-\infty}^{\infty} \int_{-\infty}^{\infty} E(x,y,z)y \, dxdy}{\int_{-\infty}^{\infty} \int_{-\infty}^{\infty} E(x,y,z) \, dxdy} \qquad (70)$$

2nd order moments:

$$\sigma_x^2(z) = \frac{\int_{-\infty}^{\infty}\int_{-\infty}^{\infty} E(x,y,z)(x-\bar{x})^2 \, dxdy}{\int_{-\infty}^{\infty}\int_{-\infty}^{\infty} E(x,y,z) \, dxdy} \qquad (71)$$

$$\sigma_y^2(z) = \frac{\int_{-\infty}^{\infty}\int_{-\infty}^{\infty} E(x,y,z)(y-\bar{y})^2 \, dxdy}{\int_{-\infty}^{\infty}\int_{-\infty}^{\infty} E(x,y,z) \, dxdy} \qquad (72)$$

Beam widths in the direction of its principal axes are given:

$$d_{\sigma x}(x) = 2\sqrt{2}\left\{(\sigma_x^2 + \sigma_y^2) + \gamma\left[(\sigma_x^2 - \sigma_y^2)^2 + 4(\sigma_{xy}^2)^2\right]^{\frac{1}{2}}\right\}^{\frac{1}{2}} \qquad (73)$$

$$d_{\sigma y}(x) = 2\sqrt{2}\left\{(\sigma_x^2 + \sigma_y^2) - \gamma\left[(\sigma_x^2 - \sigma_y^2)^2 + 4(\sigma_{xy}^2)^2\right]^{\frac{1}{2}}\right\}^{\frac{1}{2}} \qquad (74)$$

where γ is a sign function which is defined as follows:

$$\gamma = sgn(\sigma_x^2 - \sigma_y^2) = \frac{\sigma_x^2 - \sigma_y^2}{|\sigma_x^2 - \sigma_y^2|} \qquad (75)$$

Based on the equations above, we can calculate the beam diameter in pixels. In addition, the beam width calculation shows that the effective diameter is the angle values when power drops to $1/e^2$ compared to its peak. However, a link needs to be built to transfer the pixels unit into the real μm unit. This could be done by changing the position of waveguide output in μm and measuring the corresponding change of position on computer screen in pixels.

the waveguide output position and recording the change of pixels captured on the computer screen. The results are plotted in Figure 119. The left figure is for the horizontal x-direction while the right figure is for the vertical y-direction. The slopes of these two lines indicate that 2.75 pixels in the x direction and 3.05 pixels in y direction are equal to 1 μm in the x and y directions, respectively.
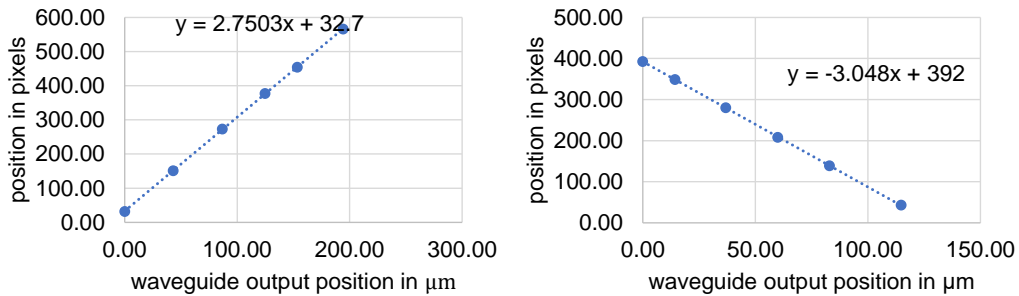
Figure 119 Relationship between distance in pixel values and μm values. Slop values indicate how many pixels can represent

1 μm in real world.

119

The beam width (d_σ) and propagation distance (Z) can then be expressed in μm units and the relation between them can be plotted. The hyperbolic curves can be fitted to the measured beam diameter along the propagation distance:

$$d_\sigma(z) = \sqrt{a + bz + cz^2} \qquad (\,76\,)$$

The far-field angle is defined as the tangent value of the fitted curve when the beam propagates to infinity, which is:

$$\theta_\sigma = \frac{d}{dz}\big(d_\sigma(z)\big) = \frac{2cz}{2\sqrt{a+bz+cz^2}} \xrightarrow{z \to \infty} \sqrt{c} \qquad (\,77\,)$$

It should be noted that θ_σ is the full angle of the far-field profile. The following example shows the far-field measurements carried out using both methods and indicates that they are in good agreement. The blue dotted line is the far-field profile based on previous measurement, and the 5% FFA is around 6°. The same plot shows the new results when power drops to $1/e^2$, and the angle is around 4.3°, as indicated by red dashed circles on the plot. The right figure indicates the beam diameter curves along the propagation distance. The far-field angle could be calculated at around 4.3° using the fitting equations. The results from both the previous and the new far-field measurement show the same FFA values, which proves that both methods work well in measuring far-field profile of the waveguide output beam. However, the new method collects the whole profile image of the beam instead of just collecting the slotted power, and can provide a smaller error range compared to the old method.
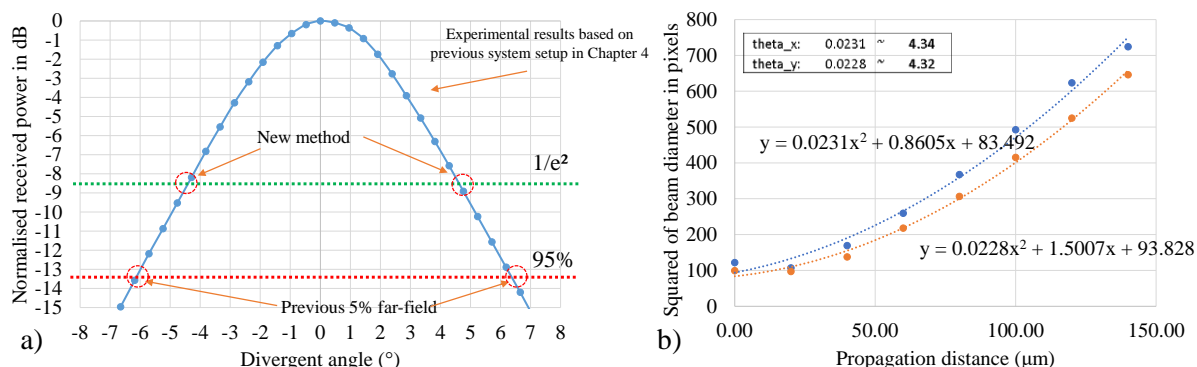
Figure 120 a): Blue dotted line is the far-field power distribution of the SMF output. 5% FFAs are the angle values when its far-field profile intersects with red dash line (-13 dB). Green dash line indicates the new far-field angle results obtained from using ISO-11146 method. b): curve fitting of un-focused beam width. New far-field angle is calculated as square root of first coefficient according to ISO-11146.

Far-field measurements were taken again by employing the new method for the waveguide samples with different lengths: 2.5 cm, 4.9 cm and 15.8 cm. The results are given below in Figure 121.
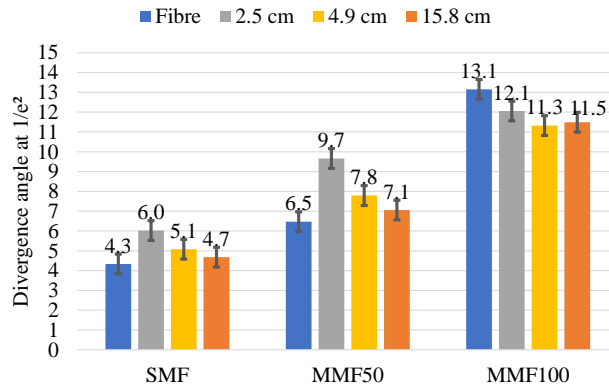
Figure 121 New far-field angles of waveguides in different lengths measured by ISO 11146-1 standard.

As can be seen, the shortest waveguide sample resultant in the highest divergence angle at $1/e^2$ while the longest sample caused the lowest divergence angle under the SMF and 50 μm MMF launches. As for the 100 μm MMF launch, the results also indicate the same trend in general. The same conclusion can be obtained that the mode loss dominates over mode coupling in the longer waveguide. The mode coupling caused by the waveguide side rough surface was not obvious enough to be observed in the experiments. However, the mode loss due to surface roughness can clearly be seen.

Chapter 6 Bandwidth investigation of flexible polymer waveguides

Polymer waveguides are used to achieve high-speed short-reach communications. Bandwidth is the key parameter which defines the maximum data rate that waveguides can support. This chapter introduces an ultra-short pulse system which could be used to estimate the bandwidth of polymer waveguides as well as analyse their accuracy. It is well known that the loss performance of a flexible polymer waveguide is highly reliant on the input mode excitations. This chapter first carries out experimental work to show the bandwidth behaviour under different excitations. Then, the waveguide is bent at different bending radii and the according bandwidths are also measured. These results indicate how bends will affect the bandwidth performance of the waveguide. Finally, 40 Gbps transmission of a flexible polymer waveguide under flexure is successfully demonstrated. Waveguide samples used in this chapter are provided by Dow Corning company which were shown in Figure 50 (not the new proposed bend-insensitive polymer waveguide samples).

6.1 Ultra-short pulse measurement

The bandwidth parameter of a polymer waveguide is quite important as a larger bandwidth can provide high data rate communications on board or board-to-board. Similar waveguides based on siloxane material have demonstrated 40 Gbps transmission over a 1 m long waveguide [32]. Currently, recent research indicates that the maximum operating speed for VCSELs with error-free rate is 57 Gbps, which can increase to 71 Gbps when an equalization technique is employed [154-159]. For optical receivers, 1x12 high-speed photodiode arrays with each diode operating up to 40 Gbps are commercially available at 850 nm [159]. However, these active electronic components are still far from measuring the bandwidth of polymer waveguides, as siloxane-based polymer waveguides have the potential ability to support 100 Gbps transmission under restricted launch conditions [160]. As a result, this thesis introduces an indirect method to estimate the upper bandwidth boundary of flexible polymer waveguides. The main idea for this new measurement is to send an ultra-short laser pulse to the waveguide sample, and to capture and measure the laser pulse at the waveguide output side. By comparing the pulse width of the input and output pulses, modal

dispersion can be obtained. In addition, in the frequency domain, we could extract the maximum frequency that the waveguide can support. The reason for using an ultra-short laser pulse is that it contains a very broad spectrum in the frequency domain.

The system diagram for the short pulse laser is shown in Figure 122. There is no 850 nm femto-second laser in the lab. Therefore, a femto-second erbium-doped mode-locked fibre laser source (TOPTICA FemtoFiber Scientific [161]) was used which operates at ~1550 nm. This femto-second laser can generate laser pulse width (FWHM) ~300 to 400 fs with peak power around +10 dBm. The fibre went through a polarizer and was then injected into a frequency doubling crystal (second harmonic generation, SHG (MSHG1550-0.5-1 [162])). The crystal only accepts one specific direction of polarized laser beam, which is the reason why a polarizer was employed prior to the crystal. The frequency of the output laser pulse was doubled to ~787 nm, collected via an objective. The femto-laser used in this work consisted of all the above components. The average output power of this laser was around 0 dBm to +10 dBm, which is sufficient for use in the following measurements.
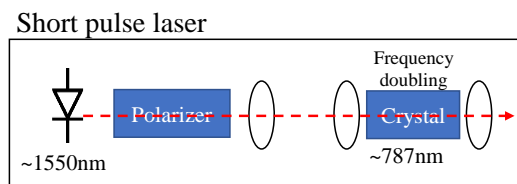
Figure 122 Ultra-short pulse laser used in this bandwidth measurement. Laser light generated from a 1550 nm femto-laser goes through a frequency doubling crystal which can generate second order harmonic of the input light. Frequency is doubled and wavelength is changed into around 787 nm.

On the receiver side, an autocorrelator was employed to detect the laser pulse. The system diagram is given in Figure 123, which is quite complicated. The basic idea of this autocorrelator was that the received laser beam was split into beams via a beam splitter. These two beams were then recombined after an adjustable optical delay was introduced into one beam path. This adjustable optical delay was made by using a mirror mounted on a loudspeaker. The combined beam went through an objective and an optical chopper and then entered another SHG crystal. The chopper and lock-in amplifier are employed to increase the signal to noise ratio. The SHG signal is detected and amplified by a highly sensitive photomultiplier tube (PMT). In the intensity autocorrelator, the input

123

laser pulse is used to measure itself. The field has an intensity that's proportional to the product of the intensities of the two input pulses:

$$I_{sig}^{SHG}(t, \tau) \propto I(t) \times I(t - \tau)$$

Detectors are too slow to resolve this beam in time, so they will measure:

$$I_{AC}(\tau) \propto \int_{-\infty}^{\infty} I(t)I(t - \tau)dt$$

In the experiment, all the response fields superimpose at the plane of detection and the detector does not have spatial resolution. Therefore, the fringes are averaged and there is a background. The signal to background ratio is given in [163] for the nth-order autocorrelation:

$$n!\,(n-1)! \sum_{i_1=0}^{n} \sum_{i_2=0}^{i_1} \dots \sum_{i_{n-1}=0}^{i_{n-2}} \times \left[\frac{1}{(n - i_1)!\,(i_1 - i_2)..\,(i_{n-2} - i_{n-1})!\,(i_{n-1})!} \right]^2 : 1$$

For the SHG, a second-order autocorrelation, this equation yields a ratio of 3:1.
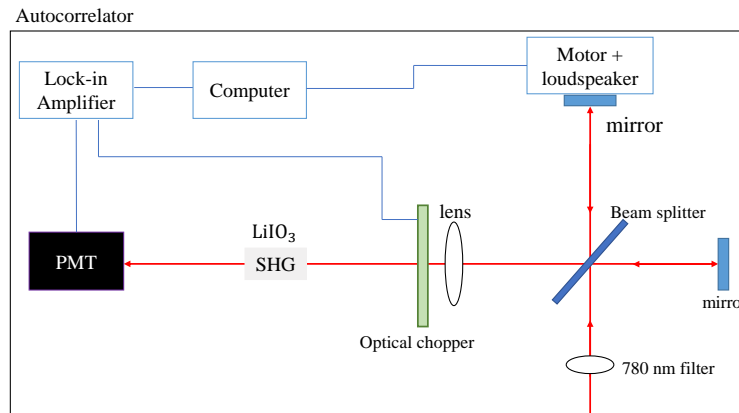
Figure 123 Diagram of the home-made autocorrelator used in this work.

The intensity autocorrelation traces of the laser pulse can be obtained from the autocorrelator. Three common pulse shapes such as Gaussian, Sech², and Lorentzian are used to fit the autocorrelation trace of the received optical pulse. Then, the full width at half maximum (FWHM) of AC pulse can be extracted based on the fitting curves. The conversion from the FWHM AC trace width ($\Delta\tau$) to the FWHM original width (Δt) can be found based on the following figure below [163, 164].

Pulse shape	I(t)	Time-bandwidth Product $\Delta\nu \cdot \Delta t$	$\frac{\Delta\tau}{\Delta t}$
Gaussian	$\exp\left(-\frac{4ln2t^2}{\Delta t^2}\right)$	0.441	$\sqrt{2}$
Secant hyperbolic	$\text{sech}^2\left(\frac{1,76t}{\Delta t}\right)$	0.315	1.55
Lorentz	$1/\left(1+\frac{2t}{\Delta t}\right)^2$	0.221	2

Figure 124 Relationship between the autocorrelation width and pulse width for commonly used pulse shapes, Gaussian,

Secant hyperbolic and Lorentz.

Therefore, based on the fitted AC curves, the original pulse shape and FWHM can be calculated, followed by a Fourier transform. Finally, the spectrum of the femto-second laser pulse can be extracted. Before taking any measurement, a back-to-back measurement needs to be taken for each input launch condition. In this example, 50 μm MMF is employed as the input launch and the output beam is directly focused on the autocorrelator via a $\times 20$ objective.
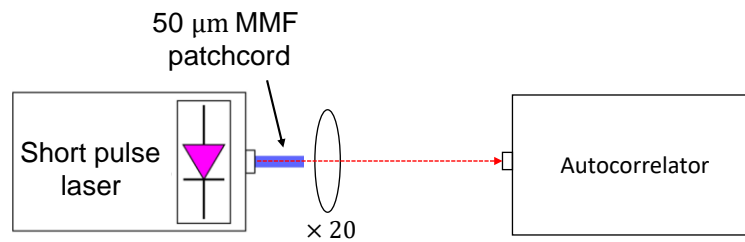
Figure 125 Back-to-back system setup of the ultra-short pulse measurement using 50 μm MMF as the input launch.

Autocorrelator measures the pulse that directly from short pulse laser.

The measured AC laser pulse is indicated by the blue dashed line in Figure 126, and it is fitted by Gaussian, Sech² and Lorentzian curves. It can be seen that the measured AC pulse can be well fitted by a Sech² curve in this case, and the obtained FWHM of AC pulse is 0.64968 ps. Then, the original laser FWHM can be calculated based on Figure 124, which is $0.64968 \text{ ps} \times \frac{1}{1.55} = 0.419 \text{ ps}$.
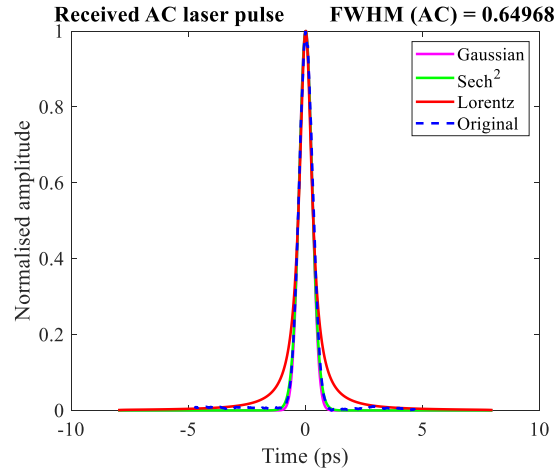
Figure 126 AC laser pulse under the 50 μm MMF input fitted by Gaussian, Sech² and Lorentzian curves. FWHM of AC pulse

is measured to be 0.64968 ps.

Once the original pulse is determined, the frequency spectrum can also be calculated using a Fourier transform, which is given in Figure 127.
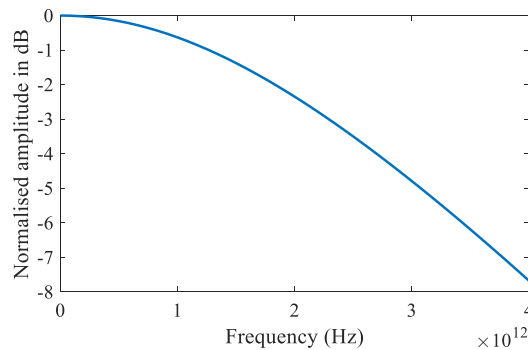
Figure 127 Optical spectrum of a 50 μm MMF input laser pulse based on Sech² curve fitting.

6.2 Mode excitations on bandwidth performance

The performance of a flexible polymer waveguide highly relies on the mode excitation inside the waveguides. From the previous bending performance in Chapter 3, a more uniform input condition will result in a worse bending performance, while a restricted input launch produces a much better performance. In addition, Chapter 4 showed that we get higher order modes are easier to leak out of waveguides resulting in a big scattering loss. As a result, to better study the bandwidth performance of a polymer waveguide, the input mode excitation must be controlled effectively. Thus, four different input launch conditions are introduced here: $\times 10$, $\times 16$, $\times 40$ objectives, and a 50 μm MMF input.

126

The system setup is shown in Figure 128. The laser pulse from the short pulse laser box was injected into a straight flexible waveguide via an objective. To control the mode excitation, different objectives were used here from $\times 10$ to $\times 40$. In addition, the normally used 50 μm MMF input was also employed, as shown in the following figure. At the receiver end, a $\times 20$ objective was used to focus the laser pulse onto the autocorrelator. The previous 24 cm long, 6 mm wide flexible polymer waveguide sample was used in this work.
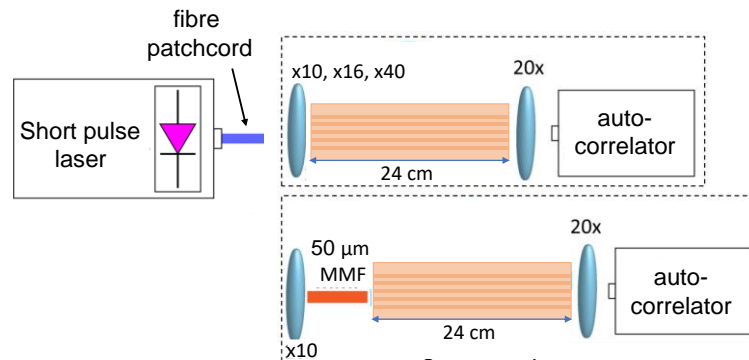
Figure 128 Investigation of mode excitation effects on the bandwidth performance of a flexible polymer waveguide. Short

pulse laser was employed as input source and auto-correlator was used at output side to measure its AC pulse width.

Flexible polymer waveguide was employed in the middle with different input launch conditions.

Before taking the AC pulse measurement, the 5% far-field measurements were taken based on those different input excitations. Those 5% FFA results can help to indicate the mode distribution inside the waveguide. The results are given in Figure 129, where $\times 25$ and $\times 50$ objective inputs were also added during the measurement. Six waveguide channels were measured, and their average values are listed on the chart. The results show that the $\times 10$ objective input is also a restricted input launch and the $\times 40$ objective input has a similar FFA to the 50 μm MMF input. It should be noticed that all those input launches above are still far from uniform launch conditions.
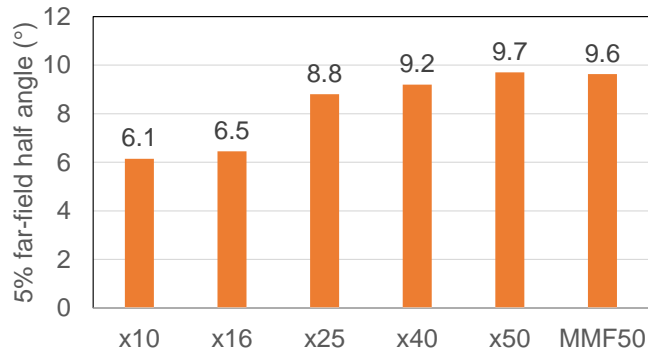
Figure 129 5% FFAs of different input excitations for ultra-short laser pulse measurements. Input launch conditions are chosen from most restricted one: ×10 lens to relatively restricted one: 50 μm MMF. All launches are under-filled.

The calculated bandwidths of the straight waveguide sample under different input launch conditions are shown in Figure 130. The waveguide bandwidth was estimated using pulse broadening measurements and the corresponding bandwidth-length product (BLP) was calculated, which is a common metric used in multimode fibre transmission systems to quantify the induced dispersion. As the main dispersion component in such systems is multimode dispersion [165], its magnitude scales linearly with link length, resulting in a constant BLP value that characterises the fibre performance [166]. A similar approach is taken here for these straight multimode waveguides.
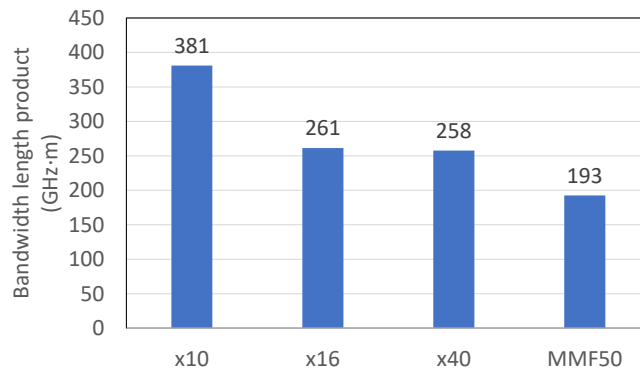
Figure 130 Bandwidth length product (BLP) of a straight polymer waveguide under different launch conditions.

The influence of input mode excitation on the bandwidth performance of the flexible polymer waveguide is clearly seen from the results above. Although, this is an indirect method for measuring the bandwidth of the waveguide, the values still indicate the potential ability to achieve high speed transmission. The results for the $\times 10$ objective input, which is a restricted input launch condition, indicate that the waveguide could support over 300 GHz·m BLP. The 50 μm MMF input, due to the

128

many higher-order modes it excites at the waveguide input side, has the lowest BLP, but is still over 150 GHz·m.

6.3 Bend effects on the bandwidth performance

6.3.1 Bend effects on the bandwidth performance of flexible polymer waveguides

The bandwidth of the flexible polymer waveguides was investigated when a flexure is applied. The system setup was the same as previous one, with the straight flexible polymer waveguide sample being replaced by a flexible one, as shown in Figure 131.
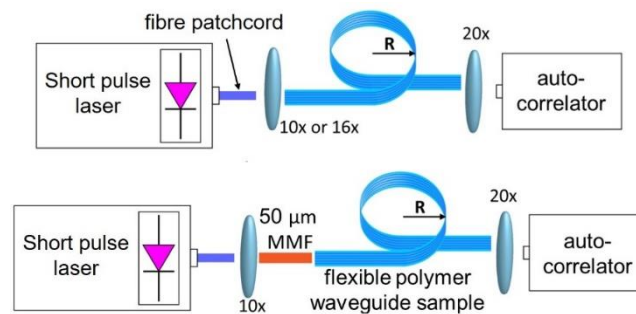
Figure 131 Experimental setup for bandwidth studies using a lens launch and a 50 μm MMF input.

Different launches were employed at the waveguide input implemented with microscope objectives with different magnifications: 10× and 16× and a short 50 μm MMF patch-cord. The flexible sample was wrapped 360° around a cylindrical mandrel of a certain radius of curvature, with the position of the bend being roughly in the middle of the waveguide length. The output light was collected with a 20× microscope objective and delivered to a matching autocorrelator. Typically, restricted launches result in Sech²-shaped output pulses as these types of launches mainly excite lower order modes inside the waveguide that exhibit small differences in their group velocities. On the other hand, more overfilled or offset launches result in output pulses that are better fitted by Lorentzian-shaped pulses due to the excitation of higher order modes at the waveguide input and the larger induced multimode dispersion. The calculated bandwidth length products of the waveguide sample under flexure are shown in Figure 132.
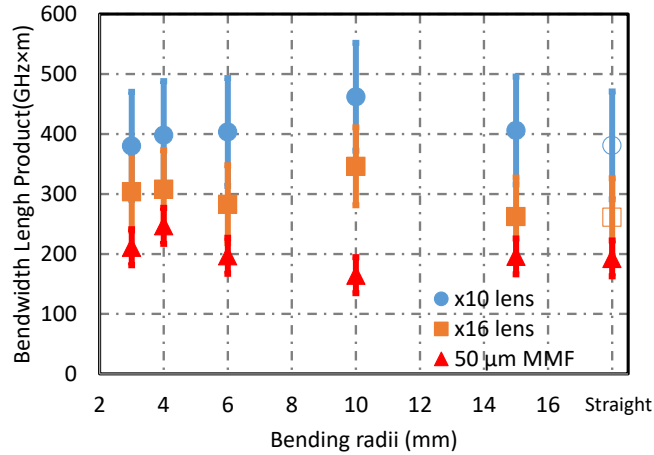
Figure 132 Bandwidth length product (BLP) of the flexible polymer waveguide sample under flexure. Several bending radii were employed and three different launch conditions were used.

BLP values larger than 150 GHz×m were recorded for all the launch conditions studied and the bending radii used. As expected, the use of the 50 μm MMF input resultant in lower bandwidth values due to the excitation of higher-order modes at the waveguide input. The lens input yielded substantially larger BLP values of >250 GHz×m. No significant degradation in bandwidth performance was observed when the waveguides were flexed, with similar BLP values obtained for the straight and bent waveguides down to 3 mm radius. The suppression of higher-order modes cannot be observed from the results above. However, flexing the waveguides is expected to have a beneficial effect with respect to the waveguide bandwidth when compared with the same waveguide without any flexure (straight) under the same launch, as higher order modes are suppressed along the bend therefore reducing multimode dispersion. Similar behaviour has been recorded in in-plane 90° bends [167]. Estimation of the bandwidth using ultra-short pulse measurement is not accurate when multi-waveguide modes are involved. Simply, those waveguide modes can overlap with each other in spatial domain which can severely degrade the measurement of pulse mode autocorrelation. This will be discussed in detail in Section 6.4.

Apart from BLP, 5% far-field half angles were also recorded for the different launch conditions in order to characterize the modal extrication inside the waveguides. Their values are summarized in Figure 133. The figure also indicates the numerical aperture (NA) of the waveguide, showing that all three inputs relatively underfill the modal volume of the waveguides. More overfilled launches were

tested during the experiments, however, the results indicated a very large variation due to the poor fitting of the AC trace.
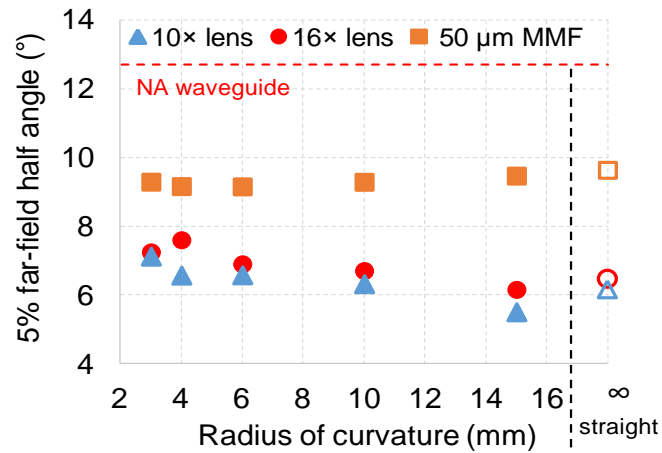
Figure 133 5% far-field half angle of the waveguide output laser beam. Numerical aperture (NA) of the waveguide is indicated by red dash line. All the launches employed during the experiment were under-filled (below red dash line). The 5% FFAs of straight flexible polymer waveguide are also measured as the reference.

The 5% FFA results indicated a similar trend in BLP values. The more waveguide modes are excited, the lower the BLP obtained. Mode mixing can have a significant impact on the performance of multimode waveguide systems, and it can happen during propagation along the waveguide or entering into the bending area of the waveguide. The BLP values show that the mode mixing effect on the waveguide bandwidth performance caused due to bends does not have an obvious impact. By contrast, input modal excitation at the waveguide input side can significantly influence the bandwidth performance of the waveguide.

6.3.2 High-speed data transmission on flexed polymer waveguides

Some demonstrations of high-speed data transmission of polymer waveguides have been successful. For example, record non-return-to-zero (NRZ) 40 Gb/s and 4-level pulse-amplitude modulation (PAM-4) 56 Gb/s data transmission have been achieved over a 1 m long polymer multimode waveguide on a rigid substrate [168, 169]. Although data transmission at rates up to 25 Gb/s has been reported over flexible polymer multimode waveguides [29, 139, 165], these demonstrations only involved straight waveguides with short lengths of ≤ 20 cm, and no particular studies have been carried out on their performance under flexure. This section demonstrates

high-speed data transmission up to 40 Gbps when a waveguide sample is under flexure under different input conditions.

The flexible polymer waveguide sample was fabricated from siloxane material provided by Dow Corning company. The waveguide channel was 1 m long in a spiral shape and deposited on 6-inch 125 μm thick Polyimide substrate. Figure 134 indicates the spiral waveguide sample illuminated by red light. Similar to previous experiments, the input and output facets were exposed using a dicing saw and no polishing steps were taken.
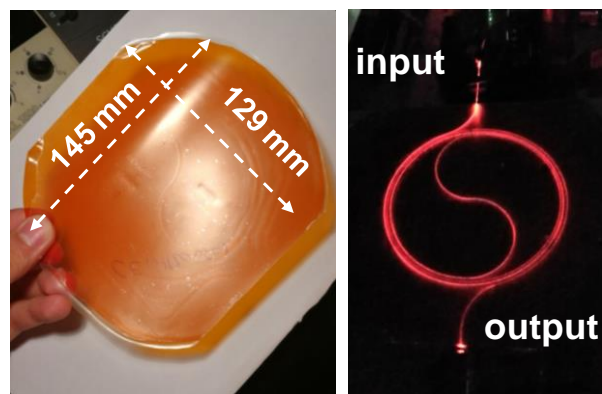
Figure 134 Image of flexible waveguide sample with size noted and a 1 m long spiral waveguide illuminated with red light. Waveguide sample was provided by Dow Corning.

Figure 135 shows the experimental setup of this work. The top diagram indicates the system with a 1 m flex spiral waveguide sample involved, and the bottom system shows the back-to-back test. A VCSEL with a bandwidth of 25 GHz and a 30 GHz fibre-coupled (VIS D30-859M) photodetector were employed as the transmitter and receiver, respectively. Two pairs of $\times 16$ objectives were used as input and output sides to couple in and out the laser light. A free space VOA was also introduced between the microscope objectives to adjust the received optical power. The VCSEL was directly modulated via a high-speed bias tee, and at the receiver side, a 38 GHz RF amplifier (SHF 810) was used to amplify the received signal to a suitable power level for bit error rate (BER) measurements. A wide-bandwidth digital sampling oscilloscope (Agilent 86100A) was used to observe the electrical waveforms and a BER test set (Anritsu MP1800A) was used to record the eye diagrams for each link. A short $2^7 - 1$ pseudo-random binary sequence was used as the data signal as it emulates the short pattern lengths typically employed in datacommunication protocols. First, the whole system without

employing waveguide sample was measured, see Figure 135 b), the measured results are used for the reference, which is also known as back-to-back (b2b) results. Then, the spiral waveguide sample was introduced into the system and the whole system was measured again under the same launch condition. The latter results are used to compare with previous b2b results and the pure performance of polymer waveguide sample can be therefore obtained.
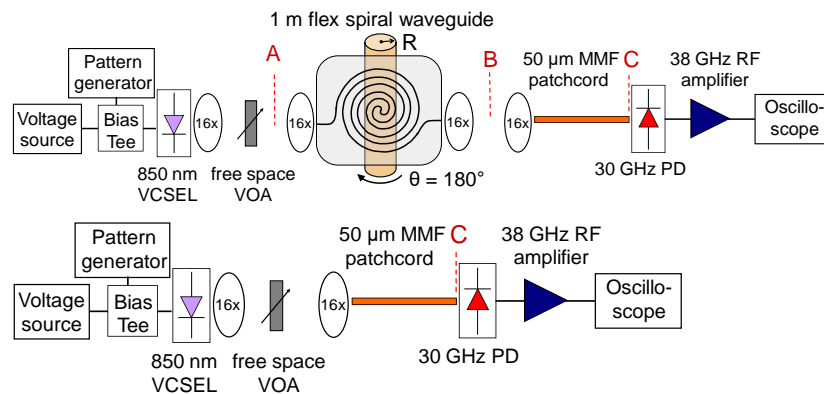
Figure 135 Experimental setup for the data transmission tests, back-to-back system was measured first as the reference

results and then 1 m flexible spiral waveguide sample was employed into the system [170].

Figure 136 shows images of the 1 m spiral waveguide sample being wrapped around a mandrel and illuminated with red light under a dark environment. Two metal pads were used to ensure the sample was wrapped tight around the mandrel.
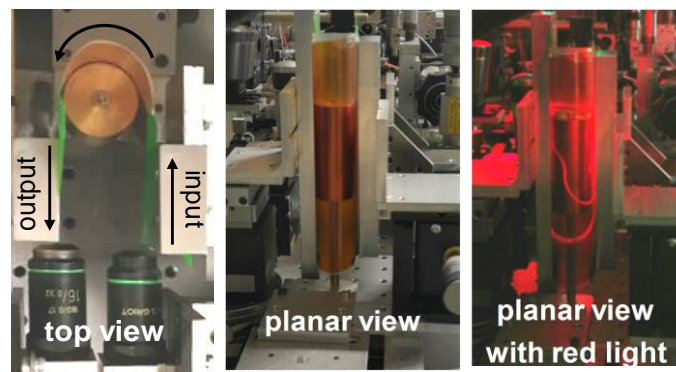
Figure 136 Images of the sample wrapping around the mandrel of 12 mm radius and illuminated with red light.

The insertion losses of the system setup were also recorded, and were found to be 6.9, 7.0, 7.6, and 8.7 dB for straight, 12 mm, 8 mm, and 4 mm radius of the bent waveguide sample, respectively. The excess losses were 0 dB, 0.1 dB, 0.7 dB, and 1.8 dB, respectively. The following figure shows the

corresponding near-field images of the waveguide output under flexure and some expected suppression of higher-order modes for a smaller radius of bending were observed as the intensity of waveguide edges was reduced.
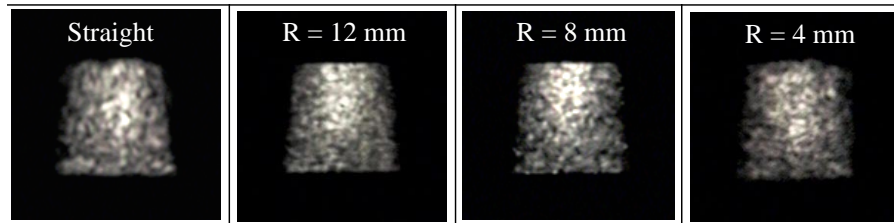
Figure 137 Near-field images of a 1 m spiral waveguide output under flexure. Employed source wavelength is 850 nm.

The recorded eye diagrams of different data transmission speeds, including 25 Gbps, 36 Gbps and 40 Gbps when the waveguide sample was flexed are shown in Figure 138. Measurements of the back-to-back and flat sample were also taken for comparison.
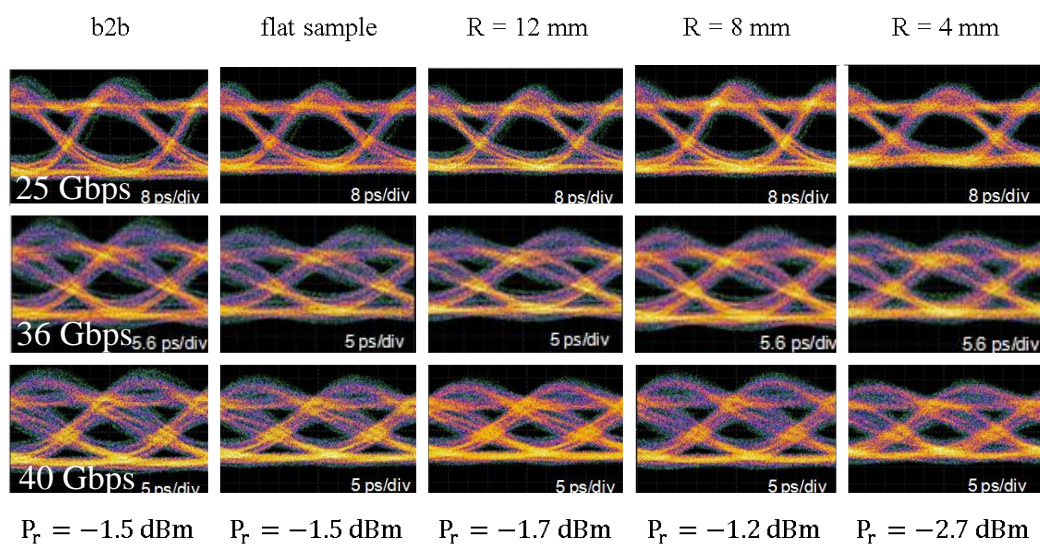
Figure 138 Received eye diagrams at different transmission speeds for the b2b and waveguide links for the different radii

applied to the 1 m spiral waveguide sample.

Open eye diagrams were obtained at 40 Gbps transmission under all bending radii. Compared to the b2b result, the additional noise and distortion introduced by the 1 m flexible polymer waveguide were quite small. If the devices had higher bandwidth, over 40 Gbps could be successfully demonstrated. Bit error rates as a function of the received optical power were also studied. The following figure below shows the BER curves for all data rates and radii of curvature down to 4 mm.
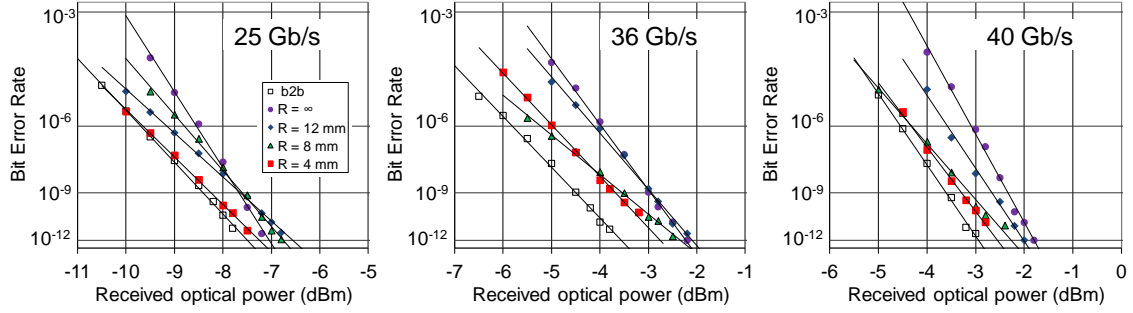
Figure 139 BER plots at 25 Gbps, 36 Gbps, and 40 Gbps for the b2b and waveguide links for the different radii applied to

the 1 m spiral waveguide sample [170].

The error free rate (BER $< 10^{-12}$) that can be achieved for the 40 Gbps data rate and the minimum required received optical power was less than -1.7 dBm. It should be noticed that, the required received optical power for 4 mm bending of the sample was much less than for the flat sample, which can be attributed to the suppression of the higher order modes along the waveguide bends. The obtained results were in agreement with the results obtained from bandwidth studies on multimode waveguide bends on rigid substrates [167]. The mode mixing (mode loss) effect was observed in this demonstration and it proves that small bends introduced into a waveguide link could improve the bandwidth performance of the waveguides. By contrast, in previous ultra-short pulse measurement, we could only reach the conclusion that bends do not degrade the bandwidth performance of the waveguides.

6.4 Current limitations and further improvement

6.4.1 Limitation of ultra-short laser pulse measurement

The system works very well if only a single mode is involved during the measurement. However, the flexible polymer waveguides are highly multimodal waveguides. If a single laser pulse is injected into the waveguide, the output pulse may not be a single pulse due to modal dispersion or scattering effects inside the waveguide. The output pulse may have a post-pulse in the time domain and the resulting AC trace might not be simply fitted by Gaussian, Sech² or Lorentzian curves. The following figure illustrates this property. As can be seen, the resulting AC pulse has two additional sub-peaks on the sides. However, in reality there are hundreds of post-pulses in the time domain. The resulting AC

135

pulse becomes much wider than expected, and the post-pulses also beat with each other, resulting in a higher background level.
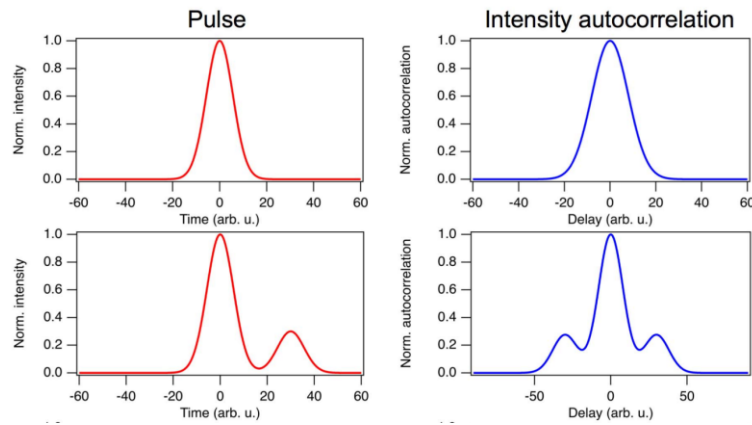
Figure 140 Laser pulses with post-sub peaks and their resultant AC traces [171].

During the measurement, the waveguide was excited by two different input conditions and the corresponding AC pulses were recorded, as shown in Figure 141. The left figure is the AC trace when a 50 μm MMF input was employed. The sub-peaks can be clearly observed due to the multimode nature of the input launch. However, the AC traces can still be fitted if those sub-peaks are ignored and FWHM can be estimated within a small error range. After the input fibre is offset to generate a more uniform input launch condition, the resulting AC trace is given in the right figure. Due to the separation of hundreds of modes in the time domain, the resulting AC trace is much wider than the real one. In addition, the ratio in the right figure is much less than 3, due to the higher background level. Different modes have different speeds when propagating in the waveguide and at the output side, those waveguide modes overlap with each other. When measuring the pulse modal dispersion, overlap parts are also measured and counted into AC pulse width. We can see the obtained FWHM of AC trace is 2.66 ps which is almost four times wider than the left AC trace. Poor fitting was obtained from this AC trace, and as a result the bandwidth length produced based on the poor fitting would be very inaccurate. This is also the reason why, during the experiments, we kept the input launch conditions far away from the waveguide NA to avoid overfilled excitation.
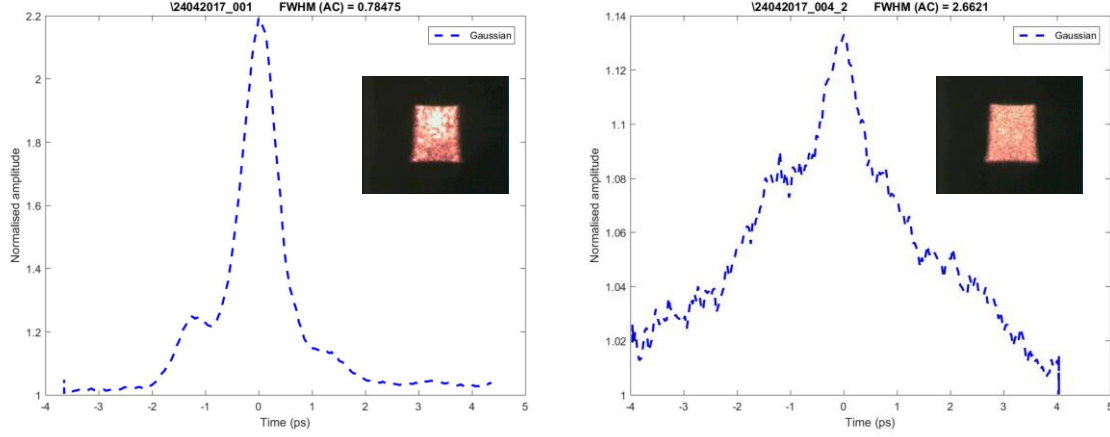
Figure 141 AC traces of waveguide output pulses under two different launch conditions. Restricted launch condition results in a better and clearer curve while over-filled launch generates a bad curve and poor fitting.

6.4.2 Calculation of error range

We have seen that higher-order modes involved in the system would cause the results to be very inaccurate. As for the previous results in Section 6.3, it is better to calculate their error ranges to make sure the values are meaningful and can be used as a guide in the real world. First, according to the theory, bandwidth (BW) is proportional to $1/\tau$, where τ is the pulse broadening and can be calculated as:

$$\tau = \sqrt{\tau_{out}^2 - \tau_{in}^2}$$

(78)

where τ_{out} and τ_{in} are the pulse widths of the output and input, respectively, and can be obtained from the measurement. According to the propagation of error formula $\Delta\tau$ can be calculated:

$$\Delta\tau = \sqrt{\left(\frac{\partial\tau}{\partial\tau_{out}}\Delta\tau_{out}\right)^2 + \left(\frac{\partial\tau}{\partial\tau_{in}}\Delta\tau_{in}\right)^2} = \sqrt{\left(\frac{\tau_{out}}{\tau}\Delta\tau_{out}\right)^2 + \left(\frac{\tau_{in}}{\tau}\Delta\tau_{in}\right)^2}$$

(79)

If it is assumed that $\Delta\tau_{out} = \Delta\tau_{in}$, $\Delta\tau$ could be simplified as:

$$\Delta\tau = \Delta\tau_{out}\sqrt{\frac{\tau_{out}^2 + \tau_{in}^2}{\tau^2}} = \Delta\tau_{out}\sqrt{\frac{\tau^2 + 2\tau_{in}^2}{\tau^2}}$$

(80)

The equation $BW = \frac{a}{\tau + b}$ was used to fit the results in Figure 133, where a and b are fitting parameters to be determined. The fitted results are given in Figure 142. From the results, we can see that the bandwidth measurements carried under 50 μm MMF input launch show a very good fit. All

137

the results lie on the fitted curve line. However, the values obtained by employing $\times 10$ lens input have the worst fit and the results are scattered.
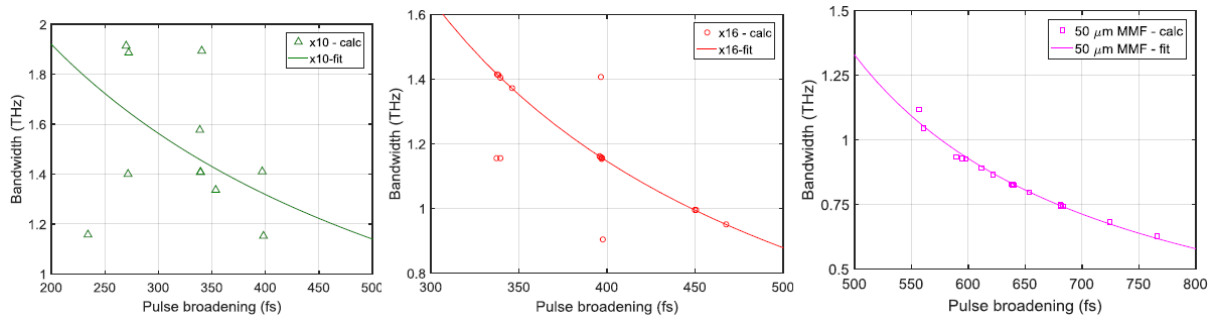
Figure 142 Bandwidth values as a function of pulse broadening.

Assuming that $\Delta\tau_{in}$ has an error of 20 fs in the bandwidth measurement, the error of the bandwidth could be determined, where a, b, $\Delta\tau$ and τ are known from the above calculations as shown in Figure 143.

$$\Delta BW = \Delta\left(\frac{a}{\tau+b}\right) = -\frac{a}{(\tau+b)^2}\Delta\tau \qquad (81)$$
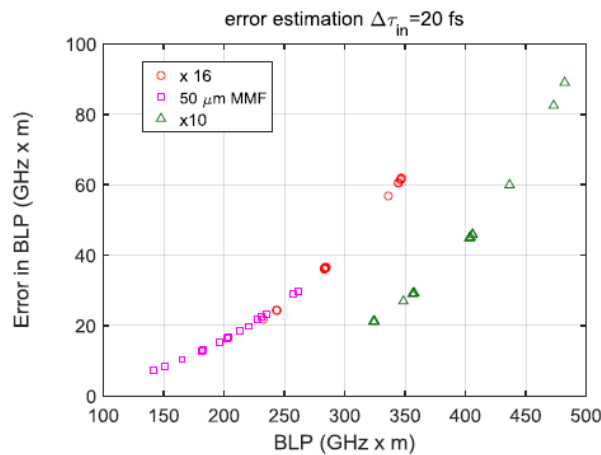
Figure 143 Bandwidth error calculation in BLP measurement under different launch conditions.

The error bar range of each BLP value could be obtained from this plot. The maximum error is around 90 GHz $\times$ m under $\times 10$ input, however, the measured BLP under this launch is over 450 GHz $\times$ m. This error could not generate great uncertainty in the measurement. The error range for the common 50 μm MMF input is around 20 GHz $\times$ m, which is relatively small compared to its measured BLP values. Thanks are due to Dr. Nikos for the help with the calculations.

6.4.3 Further improvement of ultra-short pulse measurement

The multimodal nature of waveguides limits the accuracy of ultra-short pulse measurement. The post-pulses caused by higher-order modes in the time domain will beat with each other in the AC trace and the resulting AC traces are thus much wider and in worse shape. The calculated bandwidth based on the poor fitting is far away from the real values.

Currently, there is no excellent method to solve this problem, and the way we chose to solve it in the lab was to avoid introducing many modes inside the waveguide. At the waveguide output side, far-field measurements were taken to estimate the mode distribution inside the waveguide to ensure that the mode number was not too high and thus remained far away from the uniform input.

There is a complex technique called frequency-resolved optical gating (FROG) which can be used to completely characterise ultra-short pulses [172, 173]. FROG is simply a spectrally resolved autocorrelation, which allows the use of a phase-retrieval algorithm to retrieve the previous pulse intensity and phase vs. time. Currently, FROG is a standard technique for measuring ultra-short laser pulses and is beginning to replace the old autocorrelation method which only gives a rough estimation for the pulse length. There are many variants of FROG and details of these system setups can be found in [174, 175].

Chapter 7 Conclusions and future research directions

This chapter summarises all my PhD research work. Important findings and improvements are recapitulated in the first section. Many things still need to be done in this flexible polymer waveguide field. Therefore, in the second part, I will present some future work which I think is worth doing.

7.1 Summary of work

Optics play an important role in achieving high-speed communications. In the past, optical fibres have replaced copper links in long-haul communications. Optical fibres are currently installed everywhere in our buildings, providing high data transmission to satisfy our data demands. It is believed that optics will replace copper links for board-to-board level or on-board level communications. Flexible polymer waveguides are regarded as promising candidates, which can achieve high speed communication and at the same time provide low-cost solutions. Much research work has been done on polymer waveguides, references for which are given in Chapter 1 and Chapter 2. However, no detailed work has been done on flexible polymer waveguides.

Chapter 1 of this thesis summarised the challenges and motivations for developing flexible polymer waveguides. Those waveguides can be employed to support high data transmission in data centres, autonomous cars, and airplanes. There are variety of polymer materials that can be used, and discussion and comparison of their properties was involved in Chapter 2. After comparison, Siloxane is chosen to be the waveguide material used for this thesis as it exhibits excellent mechanical and optical properties. For example, it can withstand temperatures over 350°C and thus can survive the solder reflow process, and it shows a very low material loss of ~0.04 dB/cm at 850 nm. A fabricated waveguide polymer waveguide can be bent down to 2 mm without any cracks. After the discussion of polymer materials, a literature review of polymer waveguide technology was given in this chapter, including polymer waveguide fabrication, waveguide coupling schemes, and basic loss analysis. Before doing experiments, the methodology studies and all the simulation work were carried out first in Chapter 3. The methodology introduced three different methods to simulate waveguide modes and

trace light rays. Both straight waveguide modes and bent waveguide modes were simulated. The results showed that the bent waveguide modes are not symmetrical and tend to drift to the outer area of the waveguide. Meanwhile, the evanescent field in the outer cladding is no longer a power decay. Power is lost continuously via this outer cladding region, causing radiation loss. There are many parameters affecting the bending loss performance of the waveguide, such as refractive index distribution inside the waveguide, input source distribution, and the refractive index difference between the core and the cladding. In Chapter 3, simulation work was done to evaluate those effects. The simulation results showed that the performance of graded-index waveguides is better than step-index waveguides in terms of bending loss. Chapter 3 also discussed how different graded-index distributions also generate different bending losses. From the transition loss simulation, the results indicated that the change in ray angle is the smallest when the ray is located to the outer region of the waveguide core. Careful design of the waveguide structure or input source can minimise the transition loss based on this simulation result. Next, there is an existing air-exposed waveguide structure which can dramatically reduce the bending loss. A simulation carried out on this air-exposed waveguide shows that the excess loss can drop to ~2 dB from the previous ~8 dB. However, since there is no protection of the waveguide core, this structure can be easily contaminated by dust in the air or damaged by the outside world. After simulation, experimental work was carried out.

A detailed study was made of flexible polymer waveguides including launch conditions, the bending effect, the twisting effect, crosstalk performance and dynamic-robust behaviours. The first parts introduced the three different input launch conditions and indicated how much difference they may have on the waveguide performance. In the following sections, the bending loss, twisting loss and crosstalk performance of flexible waveguide samples were studied when the samples were bent down to 2 mm radius and twisted up to four full turns, and when different launch conditions are employed at the waveguide input. The obtained results demonstrated very good performance and reliable operation even under tight bends and multiple twists. Bending down to 3 mm with relatively low loss and small crosstalk degradation was achieved, while showing that twisting had a negligible effect on the loss and crosstalk performance of the samples as long as lateral tension in the samples was minimised. The flexible polymer waveguide was tested under a dynamic moving state, and the results showed that the power fluctuation remains within 4% for all moving speeds. Last, based on the

ideas explored in Chapter 3, a new layout structure for a flexible polymer waveguide was fabricated and tested. The resulting bending loss was around 1 dB compared to the ~4 dB achieved by traditional waveguides, which is a great improvement.

Chapter 5investigated the mode behaviour inside the waveguide. The mode mixing effects due to two common waveguide structures (micro-bend and small bend) were studied. The experimental results indicated that micro-bends increase the mode coupling while small bends result in mode loss, though both cause power losses inside the waveguide. The excess losses and 5% far-field angles were measured. The fundamental mechanism of propagation loss was then studied. Propagation loss is caused mainly by the rough surface of the waveguide sidewalls. The single ray response was then introduced to simulate the scattered rays after a single incident ray with specific angle hits the core—cladding boundary. Mode coupling effects can be retrieved based on the single ray response. In the last Chapter, the bandwidth performance of the flexible polymer waveguides was studied based on ultra-short pulse measurement. The experimental results indicated that flexible polymer waveguides can support over 150 GHz·m BLP under different launch conditions and down to 2 mm of bending. A 40 Gb/s data transmission over a 1 m spiral flexible polymer waveguide under flexure was successfully demonstrated. The BER plots experimentally proved that bends have the ability to suppress higher-order modes inside the waveguide and can improve the bandwidth performance of a flexible polymer waveguide.

The set of results showed a detailed study of flexible polymer waveguides and indicated that they have a strong potential for use in environments where shape flexibility and resistance to vibration and lateral movements are of great importance.

7.2 Future work

7.2.1 Pluggable optical bus coupler

There are a variety of waveguide couplers, such as prism couplers, grating couplers and end-butt couplers. Currently, the connection between two flexible polymer waveguides is mainly achieved by the end-butting coupling (MT connector), as it is easy to use, and can be plug-in and plug-out. However, this MT connector is quite inconvenient when building an optical data bus. For example,

the MOST data bus in cars is based on a ring topology. All the units are connected via an optical fibre, see Figure 7. At each connection, some power will be lost due to coupling losses. This architecture is not suitable for future extension and also experiences a great loss if there are too many electronic units. A potential solution is to build an optical data bus system, as shown in Figure 144 [35]. All the data is communicated in the main data bus link and drops out if there is an EUC. In the future, many new EUCs can be added to the system without changing the main bus link, just simply plugged-in to the board. In addition, if the old EUC is removed, the power will still remain inside the waveguide and the main data bus link remains intact.
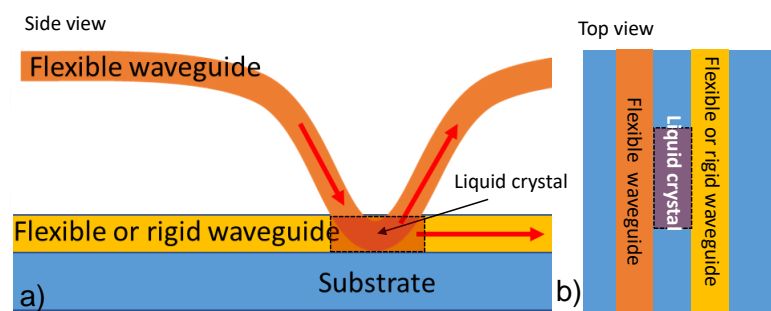
Figure 144 a): side view of new coupler design by introducing liquid crystal in intersection region. b): top view of the new coupler design, curved waveguide is not placed at the same plane as straight waveguide.

This researcher provides a method in which a force is applied to the top of the waveguide to generate a bent curve. Then, the different coupling ratio can be obtained by adjusting the force. This coupling idea is great, however, the implementation of this optical bus coupler is not suitable for integration. A potential solution is leaving a small gap between two flexible waveguides that is filled with liquid crystal. By controlling the voltage applied onto the liquid crystal (LC), the refractive index of the liquid crystal can be changed. Then, we can switch-on and switch-off the gap 'status'. For the high RI LC (on state), the top waveguide is in contact with the bottom waveguide, and the power can be coupled between the two waveguides, while for the off state, the RI of the LC is lower, and the power is blocked by the liquid crystal gap. By employing this method, we can control the coupler electronically, which is suitable for board integration. In [176], the author successfully demonstrates the use of liquid crystal to switch the power between two straight waveguides. The main challenges to achieving this method are the encapsulation of the liquid crystal and the large switching voltage.

Through careful design of the waveguide coupling position, the gap distance can be reduced, resulting in a small switching voltage and good encapsulation.

7.2.2 Bulk material scattering

Apart from the surface roughness scattering, the light rays inside the waveguide also experience bulk material scattering. This scattering is caused mainly due to the fluctuations of the local dielectric constant. In [177], the author investigated total intrinsic coupling strengths and coupling coefficients by numerically analysing the frequency responses of graded-index plastic optical fibre. However, the author's analysis is based on the assumption that the predominant mode coupling mechanism inside the fibre is forward scattering due to the microscopic heterogeneities [178-180]. Compared to plastic optical fibre, polymer waveguides have much rougher waveguide side walls. This gives rise to the question: which scattering mechanism dominates the total mode mixing effects inside the rectangular polymer waveguide, surface scattering or bulk scattering? Some preliminary results have been done to simulate bulk scattering in polymer materials, as shown in Figure 145. The incident ray is scattered from a single ray to a ray distribution by the polymer material. We can clearly observe the mode mixing from the simulation. However, there is currently no data for the simulation of siloxane material. In the future, we can measure the bulk scattering of siloxane material and use the relevant parameters to fit the simulation work. A better understanding of the bulk scattering mechanism inside the waveguide can be obtained and then a comparison between surface scattering and bulk scattering inside polymer waveguides can be drawn.
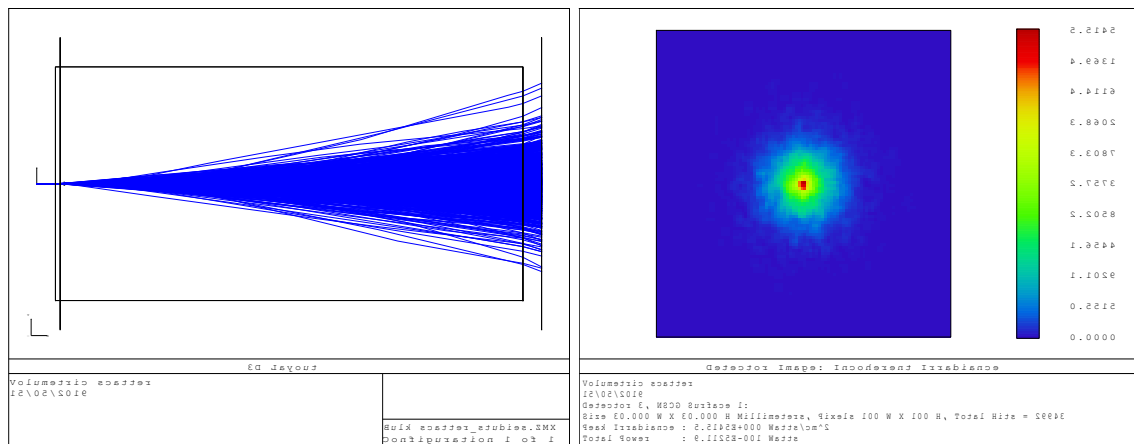
Figure 145 Simple demonstration of bulk scattering in polymer materials. A single input ray will generate hundreds of

scattered rays after passing through a bulk material (bulk scattering).

7.2.3 Extra-long flexible polymer waveguide fabrication

All the flexible polymer waveguides involved in this work were less than 25 cm long. This is due to current polymer waveguide fabrication methods. In the lab, the longest polymer waveguide sample we have is around half a metre long on rigid substrates. However, this is not long enough. Longer waveguides can help to investigate mode coupling behaviour much better and also can provide communications in the range of a few metres. Currently, the metre range of communications is dominated by optical fibres or POFs. However, there is a geometry mismatch between circular optical fibres and rectangular waveguides, and this mismatch results in power losses and reduces bandwidth performance. Long polymer waveguides can replace traditional optical fibres in metre range communications as they can directly connect to the optical PCBs at low cost. In addition, polymer waveguide films can be stacked providing easy management.

There are several types of method which can be used to fabricate longer flexible polymer waveguides, such as the roll-to-roll embossing method and the laser ablation method. Details regarding roll-to-roll method can be found in [37]. However, roll-to-roll embossing method provides high fluctuation in the performance of each waveguide. How to fabricate flexible polymer waveguides a few metres long with a small standard deviation ensuring that each waveguide has a great performance is still a worthy work to be done.

Reference

[1]   J. HECHT, *City of Light: The Story of Fibre Optics*. 198 Madison Avenue, New York, New York 10016: Oxford University Press, 1999.

[2]   M. W. J. K. C. Kao, "Spectrophotometric studies of ultra low loss optical glasses ii: double beam method," *Journal of Physics E: Scientific Instruments,* vol. 2, p. 331, 1969.

[3]   N. J. Riegel, "Optical Waveguides and Structures for Short Haul Optical Communication Channels within Printed Circuit Boards," PhD, Department of Electrical and Computer Engineering, Michigan Technological University, 2013.

[4]   H. Mardoyan, M. A. Mestre, R. Rios-Muller, A. Konczykowska, J. Renaudier, F. Jorge*, et al.*, "Single Carrier 168-Gb/s Line-Rate PAM Direct Detection Transmission Using High-Speed Selector Power DAC for Optical Interconnects," *Journal of Lightwave Technology,* vol. 34, pp. 1593-1598, 2016.

[5]   M. A. Taubenblatt, "Optical Interconnects for High-Performance Computing," *Journal of Lightwave Technology,* vol. 30, pp. 448-457, 2012.

[6]   N. Cravotta. (2002). *Wrestlemania: keeping high-speed-backplane design under control.*

[7]   Cisco, "Cisco Visual Networking Index: Forecast and Trends, 2017–2022 White Paper," 2019.

[8]   J. W. Goodman, F. J. Leonberger, S.-Y. Kung, and R. A. Athale, "Optical interconnections for VLSI systems," *Proceedings of the IEEE,* vol. 72, pp. 850-866, 1984.

[9]   F. E. Doany, C. L. Schow, R. Budd, C. Baks, D. M. Kuchta, P. Pepeljugoski*, et al.*, "Chip-to-chip Board-level Optical Data Buses Optocard," presented at the OFC/NFOEC 2008 - 2008 Conference on Optical Fiber Communication/National Fiber Optic Engineers Conference, San Diego, CA, USA, 2008.

[10]   A. F. J. Levi, "Optical interconnects in systems," *Proceedings of the IEEE,* vol. 88, pp. 750-757, 2000.

[11]   D. A. Miller, "Rationale and Challenges for Optical Interconnects to Electronic Chips," *Proceedings of the IEEE,* vol. 88, pp. 728-749, 2000.

[12]   K. Wang, A. Nirmalathas, C. Lim, E. Skafidas, and K. Alameh, "Experimental demonstration of high-speed free-space reconfigurable card-to-card optical interconnects," vol. 21, pp. 2850-2861, 2013.

[13]   M. W. Haney and M. P. Christensen, "Performance scaling comparison for free-space optical and electrical interconnection approaches," *Applied Optics,* vol. 37, pp. 2886-2894, 1998.

[14]   A. C. Walker, S. J. Fancey, M. P. Y. Desmulliez, M. G. Forbes, J. J. Casswell, G. S. Buller*, et al.*, "Operation of an optoelectronic crossbar switch containing a terabit-per-second free-space optical interconnect," *IEEE Journal of Quantum Electronics,* vol. 41, pp. 1024-1036, 2005.

[15]   H. P. Kuo, P. Rosenberg, R. Walmsley, S. Mathai, L. Kiyama, J. Straznicky*, et al.*, "Free-space optical links for board-to-board interconnects," *Applied Physics A,* vol. 95, pp. 955-965, Mar. 2009.

[16]   H.-H. Park, S. H. Hwang, M. H. Cho, S.-K. Kang, and T.-W. Lee, "Fusion of Fiber-Optic and PCB Technologies for In-board Optical Interconnection," presented at the 2006 International Conference on Photonics in Switching, Heraklion, Crete, Greece, 2006.

[17]   M. Schneider, T. Kühner, T. Alajoki, A. Tanskanen, and M. Karppinen, "Multi channel in-plane and out-of-plane couplers for optical printed circuit boards and optical backplanes," in *Proceedings 59th Electronic Components and Technology Conference*, 2009, pp. 1942-1947.

[18]   M. Ohmura and K. Saito, "High-density optical wiring technologies for optical backplane interconnection using downsized fibers and pre-installed fiber type multi optical connectors," in *Optical Fiber Communication Conference*, 2006, p. OWI71.

[19]   I.-K. Cho, J.-H. Ryu, and M.-Y. Jeong, "Interchip link system using an optical wiring method," *Optics Letters,* vol. 33, pp. 1881-1883, 2008.

[20]   N. Bamiedakis, J. Beals, R. V. Penty, I. H. White, J. V. DeGroot, and T. V. Clapp, "Cost-Effective Multimode Polymer Waveguides for High-Speed On-Board Optical Interconnects," *IEEE Journal of Quantum Electronics,* vol. 45, no. 4, pp. 415-424, Apr. 2009.

[21]   L. Schares, J. A. Kash, F. E. Doany, C. L. Schow, C. Schuster, D. M. Kuchta, *et al.*, "Terabus: Terabit/Second-Class Card-Level Optical Interconnect Technologies," *IEEE Journal of Selected Topics in Quantum Electronics,* vol. 12, no. 5, pp. 1032-1044, Sep./Oct. 2006.

[22]   X. Wang, W. Jiang, L. Wang, H. Bi, and R. T. Chen, "Fully Embedded Board-Level Optical Interconnects From Waveguide Fabrication to Device Integration," *Journal of Lightwave Technology,* vol. 26, pp. 243-250, 2008.

[23]   F. E. Doany, C. L. Schow, C. W. Baks, D. M. Kuchta, P. Pepeljugoski, L. Schares, *et al.*, "160 Gb/s Bidirectional Polymer-Waveguide Board-Level Optical Interconnects Using CMOS-Based Transceivers," *IEEE Transactions on Advanced Packaging,* vol. 32, no. 2, pp. 345-359, May 2009.

[24]   A. Horimoto, K. Kitazoe, and R. Kinoshita, "Simple channel reconnection using polynorbornene based GI waveguide for optical interconnect," in *IEEE CPMT Symposium Japan (ICSJ)*, Kyoto, Japan, 2015, pp. 122-125.

[25]   R. Kinoshita, D. Suganuma, and T. Ishigure, "Accurate interchannel pitch control in graded-index circular-core polymer parallel optical waveguide using the Mosquito method," *Optics Express,* vol. 22, no. 7, pp. 8426-8437, Apr. 2014.

[26]   R. Dangel, C. Berger, R. Beyeler, L. Dellmann, M. Gmur, R. Hamelin, *et al.*, "Polymer-Waveguide-Based Board-Level Optical Interconnect Technology for Datacom Applications," *IEEE Transactions on Advanced Packaging,* vol. 31, no. 4, pp. 759-767, Nov. 2008.

[27]   J. Beals, N. Bamiedakis, A. Wonfor, R. V. Penty, I. H. White, J. V. DeGroot, *et al.*, "A terabit capacity passive polymer optical backplane based on a novel meshed waveguide architecture," *Applied Physics A: Materials Science & Processing,* vol. 95, pp. 983-988, 2009.

[28]   N. Bamiedakis, A. Hashim, R. V. Penty, and I. H. White, "Regenerative polymeric bus architecture for board-level optical interconnects," *Optics Express,* vol. 20, pp. 11625-11636, 2012.

147

[29]   N. Bamiedakis, A. Hashim, R. V. Penty, and I. H. White, "A 40 Gb/s Optical Bus for Optical Backplane Interconnections," *Journal of Lightwave Technology,* vol. 32, no.8, pp. 1526-1537, Apr. 2014.

[30]   K. Schmidtke, F. Flens, A. Worrall, R. Pitwon, F. Betschon, T. Lamprecht*, et al.*, "960 Gb/s Optical Backplane Ecosystem Using Embedded Polymer Waveguides and Demonstration in a 12G SAS Storage Array," *Journal of Lightwave Technology,* vol. 31, no. 24, pp. 3970-3975, Dec. 2013.

[31]   N. Bamiedakis, C. Jian, R. V. Penty, and I. H. White, "Bandwidth Studies on Multimode Polymer Waveguides for >25 Gb/s Optical Interconnects," *IEEE Photonics Technology Letters,* vol. 26, no. 20, pp. 2004-2007, Sep. 2014.

[32]   N. Bamiedakis, C. Jian, P. Westbergh, J. S. Gustavsson, A. Larsson, R. V. Penty*, et al.*, "40 Gb/s Data Transmission Over a 1-m-Long Multimode Polymer Spiral Waveguide for Board-Level Optical Interconnects," *Journal of Lightwave Technology,* vol. 33, no. 4, pp. 882-888, Feb. 2015.

[33]   N. Bamiedakis, J. L. Wei, J. Chen, P. Westbergh, A. Larsson, R. V. Penty*, et al.*, "56 Gb/s PAM-4 data transmission over a 1 m long multimode polymer interconnect," in *Conf. Lasers Electro-Optics*, San Jose, CA, USA, 2015, paper STu4F.5.

[34]   K. Date, K. Fukagata, and T. Ishigure, "Core position alignment in polymer optical waveguides fabricated using the Mosquito method," *Optics Express,* vol. 26, pp. 15632-15641, 2018.

[35]   L. Lorenz, K. Nieweglowski, Z. Al-Husseini, N. Neumann, D. Plettemeier, K.-J. Wolter*, et al.*, "Asymmetric Optical Bus Coupler for Interruption-Free Short-Range Connections on Board and Module Level," *Journal of Lightwave Technology,* vol. 35, pp. 4033-4039, 2017.

[36]   R. Dangel, F. Horst, D. Jubin, N. Meier, J. Weiss, B. J. Offrein*, et al.*, "Development of Versatile Polymer Waveguide Flex Technology for Use in Optical Interconnects," *Journal of Lightwave Technology,* vol. 31, pp. 3915-3926, 2013.

[37]   R. Bruck, P. Muellner, N. Kataeva, A. Koeck, S. Trassl, V. Rinnerbauer*, et al.*, "Flexible thin-film polymer waveguides fabricated in an industrial roll-to-roll process," *Applied Optics,* vol. 52, pp. 4510-4, Jul 01 2013.

[38]   J. Guomin, S. Baig, and M. R. Wang, "Flexible Polymer Waveguides With Integrated Mirrors Fabricated by Soft Lithography for Optical Interconnection," *Journal of Lightwave Technology,* vol. 31, pp. 1835-1841, 2013.

[39]   H. Numata, M. Tokunari, and J. B. Heroux, "60-Micrometer pitch polymer waveguide array attached active optical flex," in *Optical Fiber Communications*, Los Angeles, CA, USA, 2017, paper W1A.5.

[40]   X. Dou, X. Wang, X. Lin, D. Ding, D. Z. Pan, and R. T. Chen, "Highly flexible polymeric optical waveguide for out-of-plane optical interconnects," *Optics Express,* vol. 18, pp. 16227-16233, 2010.

[41]   T. Yagisawa, T. Mori, R. Gappa, K. Tanaka, O. Daikuhara, T. Komiyama*, et al.*, "Structure of 25-Gb/s Optical Engine for QSFP Enabling High-Precision Passive Alignment of Optical Assembly," in *66th Electronic Components and Technology Conference*, Las Vegas, NV, USA, 2016, pp. 1099-1104.

[42]   N. Bamiedakis, F. Shi, D. Chu, R. V. Penty, and I. H. White, "Flexible multimode polymer waveguides for versatile high-speed optical interconnects," in *19th International Conference on Transparent Optical Networks*, Girona, Spain, 2017, pp. 1-4.

[43]   T. Tekin, R. Pitwon, A. Hakansson, and N. Pleros, *Optical Interconnects for Data Centers*, 2017.

[44]   J. Clement. (2019). *Mobile social media - Statistics & Facts*. Available: https://www.statista.com/topics/2478/mobile-social-networks/

[45]   D. Reinsel, J. Gantz, and J. Rydning, "Data Age 2025," 2017.

[46]   J. E. Cunningham, A. V. Krishnamoorthy, R. Ho, I. Shubin, H. Thacker, J. Lexau*, et al.*, "Integration and Packaging of a Macrochip With Silicon Nanophotonic Links," *IEEE Journal of Selected Topics in Quantum Electronics,* vol. 17, pp. 546 - 558, 2011.

[47]   D. A. B. Miller, "Optical interconnects to electronic chips," *Applied Optics* vol. 49, pp. F59-F70, 2010.

[48]   D.A.B.Miller and H.M.Ozaktas, "Limit to the Bit-Rate Capacity of Electrical Interconnects from the Aspect Ratio of the System Architecture," *Journal of Parallel and Distributed Computing,* vol. 41, pp. 42-52, 1997.

[49]   H. Thienpont, C. Berger, J. Danckaert, M. A. Kossel, C. Menolfi, T. Morf*, et al.*, "High-density optical interconnects within large-scale systems," vol. 4942, p. 222, 2003.

[50]   H. Dawei, T. Sze, A. Landin, R. Lytel, and H. L. Davidson, "Optical interconnects: out of the box forever?," *IEEE Journal of Selected Topics in Quantum Electronics,* vol. 9, pp. 614-623, 2003.

[51]   R. Dangel, J. Hofrichter, F. Horst, D. Jubin, A. La Porta, N. Meier*, et al.*, "Polymer waveguides for electro-optical integration in data centers and high-performance computers," *Optics Express,* vol. 23, pp. 4736-50, Feb 23 2015.

[52]   o. B. GmbH, *Bosch Automotive Electrics and Automotive Electronics*: Springer Vieweg, 2014.

[53]   W. Lawrenz, *Can System Engineering: From Theory to Practical Applications*: Springer; 1st ed. 1997. Corr. 2nd printing 2007 edition (26 Oct. 2007), 1997.

[54]   I. T. R. vehicles, "Interchange of digital information — Controller area network (CAN) for high-speed communication," 1993.

[55]   M. Farsi and M. Barbosa, *CANopen Implementation: Applications to Industrial Networks*: Wiley-Blackwell, 2000.

[56]   L. Consortium, "LIN Specification Package," 2003.

[57]   Microchip. (2016). *LIN Bus Networking - Transceivers and System-in-Package (SiP) Solutions*. Available: http://www.microchip.com/design-centers/lin

[58]   A. Devine and E. Kilbride, "Local Interconnect Network (LIN) Demonstration," 2000.

[59]   E. Zeeb, "Optical data bus systems in cars: current status and future challenges," presented at the Proceedings 27th European Conference on Optical Communication (Cat. No.01TH8551), Amsterdam, Netherlands, Netherlands, 2001.

[60]   S. D, M. P, S. J, W. R, and Z. E., "Application of POFs in data links of mobile systems," presented at the 7th International Conference on Plastic Optical Fibers, 1998.

[61]   T. Kibler, S. Poferl, G. Bock, H. P. Huber, and E. Zeeb, "Optical Data Buses for Automotive Applications," *Journal of Lightwave Technology,* vol. 22, pp. 2184-2199, 2004.

[62]   Berwanger, Josef, M. Peller, and R. Griessbach, "ByteFlight-a new protocol for safety critical applications," presented at the SAE Technical, 2000.

[63]   Grießbach, Robert, J. Berwanger, and M. Peller, "byteflight-neues Hochleistungs-Datenbussystem für sicherheitsrelevante Anwendungen," *AUTOMOTIVE ELECTRONICS. SONDERAUSGABE DER AUTOMOBILTECHNISCHEN ZEITSCHRIFT (ATZ) UND DER MOTORTECHNISCHEN ZEITSCHRIFT (MTZ),* 2000.

[64]   N. Instruments. (2019). *FlexRay Automotive Communication Bus Overview*. Available: https://www.ni.com/en-gb/innovations/white-papers/06/flexray-automotive-communication-bus-overview.html

[65]   (2016 August 29). *FlexRay Consortium*.

[66]   M. Schmid and Atmel. (2010). *Automotive Bus Systems*. Available: www.atmel.com

[67]   M. Cooperation, *MOST Brand Book* vol. 1.1: M. O. S. T., 2007.

[68]   A. Grzemba, "MOST : the automotive multimedia network ; from MOST25 to MOST150," 2011.

[69]   "New data bus systems," 2002.

[70]   "CALCE-EPRC Designing Electronics for Next-Generation Automobiles."

[71]   W. Si and D. Starobinski, "A Robust Load Balancing and Routing Protocol for Intra-Car Hybrid Wired/Wireless Networks," *IEEE Transactions on Mobile Computing,* vol. 18, pp. 250-263, 2017.

[72]   Christian, N. L, Passauer, L. K, and V. C. S. S. MD, "Impact of Fiber Optics on System Reliability and Maintainability," 1987.

[73]   D. E. Anderson and M. W. Beranek, "777 optical LAN technology review," presented at the 1998 Proceedings. 48th Electronic Components and Technology Conference (Cat. No.98CH36206), Seattle, WA, USA, USA, 1998.

[74]   "F35 Avionics," *Avionics Magazine,* pp. 408–483, 2007.

[75]   (2011). *F-35 Lightning II Electro-Optical Targeting System (EOTS)*.

[76]   J. M. U. Sr., "Application Of Neural Network Technology to Fly-By-Light Control Systems," presented at the International Society for Optics and Photonics, 1995.

[77]   Garg, Atul, R. I. Linda, and T. Chowdhury., "Application of fiber optics in aircraft control system & its development," presented at the International Conference on Electronics and Communication Systems (ICECS), 2014.

[78]   X. C. Tong, *Advanced materials for integrated optical waveguides*: Springer, Cham, 2014.

[79]   H. Ma, A.K.-Y. Jen, and L. R. Dalton, "Polymer-based optical waveguides: materials, processing, and devices," *Advanced materials,* vol. 14, pp. 1339-1365, Sep. 2002.

[80]   B. Kippelen, L. A. Eldada, and D. D. C. Bradley, "Polymer Integrated Optics: Promise vs. Practicality," vol. 4642, pp. 11-22, 2002.

[81]   L. YS, C. HS, G. R, S. T, B. EW, B. J*, et al.*, "Optoelectronic packaging and polymer waveguides for multichip module and board-level optical interconnect applications," presented at the 1995 Proceedings. 45th Electronic Components and Technology Conference, 1995.

[82]   Y. Ishii, S. Koike, Y. Arai, and Y. Ando, "SMT-compatible large-tolerance "OptoBump" interface for interchip optical interconnections," *IEEE Transactions on Advanced Packaging,* vol. 26, pp. 122-127, 2003.

[83]   L. Eldada and L. W. Shacklette, "Advances in polymer integrated optics," *IEEE Journal of Selected Topics in Quantum Electronics,* vol. 6, pp. 54-68, 2000.

[84]   M. G. Kuzyk, A. W. Norris, M. Eich, J. V. DeGroot, T. Ogawa, R. A. Norwood*, et al.,* "High reliability of silicone materials for use as polymer waveguides," vol. 5212, p. 76, 2003.

[85]   M. Zhou, "Low-loss Polymeric Materials for Passive Waveguide Components in Fiber Optical Telecommunication," *Optical Engineering,* vol. 41, pp. 1631-1643, 2002.

[86]   A. S. Flores, "Array Waveguide Evanescent Coupler for Card-to-Backplane Optical Interconnections," 2009.

[87]   X. M. Zhao, Y. Xia, and G. M. Whitesides, "Fabrication of three-dimensional micro-structures: Microtransfer molding," *Advanced Materials,* vol. 8, pp. 837-740, 1996.

[88]   G. Jiang, "Design and fabrication of optical polymer waveguide devices for optical interconnects and integrated optical coherence tomography," Doctor of Philosophy, Electrical and Computer Engineering, University of Miami, 2015.

[89]   K. Kruse and C. Middlebrook, "Laser-direct writing of single mode and multi-mode polymer step index waveguide structures for optical backplanes and interconnection assemblies," vol. Photonics and Nanostructures-Fundamentals and Applications, pp. 66-73, 2015.

[90]   E. Zgraggen, I. M. Soganci, F. Horst, A. L. Porta, R. Dangel, B. J. Offrein*, et al.,* "Laser Direct Writing of Single-Mode Polysiloxane Optical Waveguides and Devices," *Journal of Lightwave Technology,* vol. 32, pp. 3036-3042, 2014.

[91]   A. K. Das, "Laser direct writing polymeric single-mode waveguide devices with a rib structure," *Applied Optics,* vol. 42, pp. 1236-1243, 2003.

[92]   K. Soma and T. Ishigure, "Fabrication of a Graded-Index Circular-Core Polymer Parallel Optical Waveguide Using a Microdispenser for a High-Density Optical Printed Circuit Board," *IEEE Journal of Selected Topics in Quantum Electronics,* vol. 19, pp. 3600310-3600310, 2013.

[93]   K. Yasuhara, F. Yu, and T. Ishigure, "Circular core single-mode polymer optical waveguide fabricated using the Mosquito method with low loss at 1310/1550 nm," *Optics Express,* vol. 25, pp. 8524-8533, Apr 17 2017.

[94]   S. S. Zakariyah, *Laser ablation for polymer waveguide fabrication*: Croatia: InTech, 2012.

[95]   E. Griese, "A high-performance hybrid electrical-optical interconnection technology for high-speed electronic systems," *IEEE Transactions on Advanced Packaging,* vol. 24, pp. 375-383, 2001.

[96]   C. Zhang, J.-H. Sun, X. Xiao, W.-M. Sun, X.-J. Zhang, T. Chu*, et al.,* "High Efficiency Grating Coupler for Coupling between Single-Mode Fiber and SOI Waveguides," *Chinese Physics Letters,* vol. 30, p. 014207, 2013.

[97]   Z.-Y. Yin and B. K. Garside, "New configurations for high-efficiency prism couplers with application to GeO2optical waveguides," *Applied optics,* vol. 22, pp. 1023-1028, 1983.

[98]   S.-H. Hsu, C.-Y. Tsou, C.-M. Wang, and S.-C. Tseng, "10 Gb/s Optical Interconnection on Flexible Optical Waveguide in Electronic Printed Circuit Board," *Optics and Photonics Journal,* vol. 03, pp. 252-255, 2013.

[99]   N. Bamiedakis, A. Hashim, J. Beals, R. V. Penty, and I. White, "Low-Cost PCB-Integrated 10-Gb/s Optical Transceiver Built With a Novel Integration Method," *IEEE Transactions on Components, Packaging and Manufacturing Technology,* vol. 3, pp. 592-600, 2013.

[100]   M. Takezaki and R. Nagase, "Design for PMT Connector (Polymer waveguides connected with MT connector)," presented at the IEEE CPMT Symposium, Japan, 2014.

[101]   F. Ladouceur and J. D. Love, "Silica-based buried channel waveguides and devices," *Chapman & Hall,* 1996.

[102]   F. Ladouceur, "Roughness, inhomogeneity, and integrated optics," *Journal of Lightwave Technology* vol. 15, pp. 1020-1025, 1997.

[103]   I. Papakonstantinou, K. Wang, D. R. Selviah, and F. A. Fernández, "Transition, radiation and propagation loss in polymer multimode waveguide bends," *Optics Express,* vol. 15, pp. 669-679, 2007.

[104]   C. Sun, Y. Yu, G. Chen, and X. Zhang, "Ultra-compact bent multimode silicon waveguide with ultralow inter-mode crosstalk," *Optics Letters,* vol. 42, p. 3004, 2017.

[105]   A. W. Snyder and J. D. Love, "Reflection at a curved dielectric interface - electromagnetic tunneling," *IEEE Transactions on Microwave Theory and Techniques,* vol. 23, pp. 134-141, 1975.

[106]   I. C. Goyal, R. L. Gallawa, and A. K. Ghatak, "Bent planar waveguides and whispering gallery modes: a new method of analysis," *Journal of Lightwave Technology,* vol. 8, pp. 768-774, 1990.

[107]   *Passive fiber optics*. Available: https://www.rp-photonics.com/passive_fiber_optics3.html

[108]   S. O. Kasap and R. K. Sinha, *Optoelectronics & Photonics* vol. 340. New Jersey: Prentice Hall, 2001.

[109]   T. CHEM. *Column: What is Electromagnetic Wave Shield ?* Available: www.toyo-chem.com/en/products/electronics/column/emishield.html

[110]   A. W. SnyderJohn and D. Love, *Optical waveguide theory*: Springer Science & Business Media, 2012.

[111]   R. R. McLeod. *2D Planar guides*. Available: ecee.colorado.edu/~mcleod/pdfs/GWO/lecturenotes/planarridges.pdf

[112]   E. A. J. Marcatili, "Dielectric Rectangular Waveguide and Directional Coupler for Integrated Optics," *Bell System Technical Journal,* vol. 48, pp. 2071-2102, 1969.

[113]   G. B. Hocker and W. K. Burns, "Mode dispersion in diffused channel waveguides by the effective index method," *Applied Optics,* vol. 16, 1977.

[114]   W. J. Westerveld, S. M. Leinders, K. W. A. van Dongen, H. P. Urbach, and M. Yousefi, "Extension of Marcatili's Analytical Approach for Rectangular Silicon Optical Waveguides," *Journal of Lightwave Technology,* vol. 30, pp. 2388-2401, 2012.

[115]   A. S. Sudbo, "Improved formulation of the film mode matching method for mode field calculations in dielectric waveguides," *Pure and Applied Optics: Journal of the European Optical Society,* vol. 3, pp. 381-388, 1994.

[116]   J. E. Goell, "A circular-harmonic computer analysis of rectangular dielectric waveguides," *Bell System Technical Journal,* vol. 48, 1969.

[117]   O. V. Ivanova, M. Hammer, R. Stoffer, and E. van Groesen, "A variational mode expansion mode solver," *Optical and Quantum Electronics,* vol. 39, pp. 849-864, 2007.

[118]   P. D. Ltd. (2011). *Fimmwave-Numerical Waveguide Mode Solver*.

[119]   J. Saijonmaa and D. Yevick, "Beam-propagation analysis of loss in bent optical waveguides and fibers," *Journal of the Optical Society of America,* vol. 73, pp. 1785-1791, 1983.

[120] W. A. Gambling, H. Matsumura, C. M. Ragdale, and R. A. Sammut, "Measurement of radiation loss in curved single-mode fibres," *IEE Journal on Microwaves, Optics and Acoustics,* vol. 2, pp. 134-140, 1978.

[121] D. Marcuse, "Bending Losses of the Asymmetric Slab Waveguide," *Bell System Technical Journal,* vol. 50, pp. 2551-2563, 1971.

[122] M. Heiblum and J. Harris, "Analysis of curved optical waveguides by conformal transformation," *IEEE Journal of Quantum Electronics,* vol. 11, pp. 75-83, 1975.

[123] K. R. Hiremath, M. Hammer, R. Stoffer, L. Prkna, and J. Čtyroký, "Analytic approach to dielectric optical bent slab waveguides," *Optical and Quantum Electronics,* vol. 37, pp. 37-61, 2005.

[124] E. A. J. Marcatili, "Bends in optical dielectric guides," *Bell System Technical Journal,* vol. 48, pp. 2103-2132, 1969.

[125] E. Kuester, "Surface-wave radiation loss from curved dielectric slabs and fibres," *IEEE Journal of Quantum Electronics* vol. 11, pp. 903-907, 1975.

[126] I. A. White, "Radiation from bends in optical waveguides: The volume-current method," *IEE Journal on Microwaves, Optics and Acoustics,* vol. 3, pp. 186-188, 1979.

[127] R. Jedidi and R. Pierre, "Efficient analytical and numerical methods for the computation of bent loss in planar waveguides," *Journal of Lightwave Technology,* vol. 23, pp. 2278-2284, 2005.

[128] Z. Han, P. Zhang, and S. I. Bozhevolnyi, "Calculation of bending losses for highly confined modes of optical waveguides with transformation optics," *Optics Letters,* vol. 38, pp. 1778-80, Jun 1 2013.

[129] J. Torres, A. Baptista, and V. M. Machado, "Analysis of dielectric optical ring slab waveguides with a layered refractive index," presented at the 18th Telecommunications forum TELFOR 2010, Serbia, Belgrade, 2010.

[130] K. K. Hiremath, M. Hammer, and E. v. Groesen, "Analytic Mode Solver for Dielectric Slab Waveguide Bends," *Simulation,* vol. 10, p. 0, 2002.

[131] M. Krause, "Finite-Difference Mode Solver for Curved Waveguides With Angled and Curved Dielectric Interfaces," *Journal of Lightwave Technology,* vol. 29, pp. 691-699, 2011.

[132] F. L. Inc. *Optical fiber.* Available: https://www.fiberlabs.com/glossary/optical-fiber/

[133] N. Bamiedakis, R. V. Penty, and I. H. White, "Compact Multimode Polymer Waveguide Bends for Board-Level Optical Interconnects," *Journal of Lightwave Technology,* vol. 31, pp. 2370-2375, 2013.

[134] J. Chen, N. Bamiedakis, P. Vasil'ev, R. V. Penty, and I. H. White, "Low-loss and high-bandwidth multimode polymer waveguide components using refractive index engineering," in *Conf. Lasers Electro-Optics*, 2016, paper SM2G.

[135] A. Hashim, N. Bamiedakis, R. V. Penty, and I. H. White, "Multimode polymer waveguide components for complex on-board optical topologies," *Journal of Lightwave Technology,* vol. 31, pp. 3962-3969, 2013.

[136] J. Chopin, V. Démery, and B. Davidovitch, "Roadmap to the Morphological Instabilities of a Stretched Twisted Ribbon," *Journal of Elasticity,* vol. 119, pp. 137-189, 2014.

[137] J. Chopin and A. Kudrolli, "Helicoids, Wrinkles, and Loops in Twisted Ribbons," *Physical Review Letters,* vol. 111, p. 174302, 2013.

[138]   A. Kudrolli and J. Chopin, "Tension-dependent transverse buckles and wrinkles in twisted elastic sheets," *Proceedings of the Royal Society A: Mathematical, Physical and Engineering Sciences,* vol. 474, p. 20180062, 2018.

[139]   J. Chen, N. Bamiedakis, P. P. Vasilev, T. J. Edwards, C. T. A. Brown, R. V. Penty*, et al.,* "High-Bandwidth and Large Coupling Tolerance Graded-Index Multimode Polymer Waveguides for On-Board High-Speed Optical Interconnects," *Journal of Lightwave Technology,* vol. 34, pp. 2934-2940, 2016.

[140]   N. Corporation. *FM-1 Mode Scrambler.* Available: https://www.newport.com/medias/sys_master/images/images/hbc/h09/8974578384926/IN-11851-FM-1.pdf

[141]   J. Beals Iv, M.-J. Li, N. Bamiedakis, J. Chen, S. Kawanishi, R. V. Penty*, et al.,* "Modal noise investigation in multimode polymer waveguides," vol. 6781, p. 67810Q, 2007.

[142]   G. C. Papen and G. M. Murphy, "Modal noise in multimode fibers under restricted launch conditions," *Journal of Lightwave Technology,* vol. 17, pp. 817-822, 1999.

[143]   B. N, B. J, Y. F, W. A, P. RV, W. IH*, et al.,* "Low-Loss, High-Uniformity 1x2, 1x4 and 1x8 Polymer Multimode Y-Splitters Enabling Radio-over-Fibre Multicasting Applications," presented at the European Conference on Integrated Optics, ECIO, Conpehagen, Denmark, 2007.

[144]   N. Riegel, C. Middlebrook, K. Kruse, and M. Roggemann, "Using the 3D beam propagation method to model the effects of lithographic roughness on the attenuation of highly multimodal polymer waveguides," *Journal of Vacuum Science & Technology,* vol. 31, 2013.

[145]   J. E. Harvey, "Light-Scattering Characteristics Of Optical Surfaces," presented at the Stray Light Problems in Optical Systems, 1977.

[146]   E. R. Freniere, G. G. Gregory, and R. C. Chase, "Interactive software for optomechanical modeling," presented at the Lens Design, Illumination, and Optomechanical Modeling, 1997.

[147]   J. C. Jonsson, Z.-H. Gu, E. S. Lee, L. M. Hanssen, and M. Rubin, "Light-scattering properties of a woven shade-screen material used for daylighting and solar heat-gain control," vol. 7065, p. 70650R, 2008.

[148]   E. Griese, "Modeling of highly multimode waveguides for time-domain simulation," *IEEE Journal of Selected Topics in Quantum Electronics,* vol. 9, pp. 433-442, 2003.

[149]   R. N. Pfisterer, "Approximated scatter models for stray light analysis," *Optics & Photonics News,* vol. 22, pp. 16-17, 2011.

[150]   N. Bamiedakis, F. Shi, D. Chu, R. V. Penty, I. H. White, H. Schröder*, et al.,* "Mode-mixing in multimode polymer waveguides for on-board optical interconnects," p. 4, 2019.

[151]   C. G. Poulton, C. Koos, M. Fujii, A. Pfrang, T. Schimmel, J. Leuthold*, et al.,* "Radiation Modes and Roughness Loss in High Index-Contrast Waveguides," *IEEE Journal of Selected Topics in Quantum Electronics,* vol. 12, pp. 1306-1321, 2006.

[152]   T. Bierhoff, A. Wallrabenstein, A. Himmler, E. Griese, and G. Mrozynski, "Ray tracing technique and its verification for the analysis of highly multimode optical waveguides with rough surfaces," *IEEE Transactions on Magnetics* vol. 37, pp. 3307 - 3310, 2001.

[153]   ISO-11146. (2005). *Lasers and laser-related equipment — Test methods for laser beam widths, divergence angles and beam propagation ratios — Part 1: Stigmatic and simple astigmatic beams*.

[154]   K. D. Choquette, P. Westbergh, R. Safaisini, E. Haglund, J. S. Gustavsson, A. Larsson, *et al.*, "High-speed 850 nm VCSELs with 28 GHz modulation bandwidth for short reach communication," vol. 8639, p. 86390X, 2013.

[155]   P. Westbergh, R. Safaisini, E. Haglund, A. Larsson, J. S. Gustavsson, and E. P. Haglund, "High-speed 850 nm VCSELs operating error free up to 57 Gbit/s," *Electronics Letters,* vol. 49, pp. 1021-1023, 2013.

[156]   D. M. Kuchta, A. V. Rylyakov, C. L. Schow, J. E. Proesel, C. Baks, P. Westbergh, *et al.*, "64Gb/s Transmission over 57m MMF using an NRZ Modulated 850nm VCSEL," presented at the Optical Fiber Communication Conference, 2014.

[157]   D. M. Kuchta, A. V. Rylyakov, C. L. Schow, J. E. Proesel, C. W. Baks, P. Westbergh, *et al.*, "A 50 Gb/s NRZ Modulated 850 nm VCSEL Transmitter Operating Error Free to 90 °C," *Journal of Lightwave Technology,* vol. 33, pp. 802-810, 2015.

[158]   D. M. Kuchta, A. V. Rylyakov, F. E. Doany, C. L. Schow, J. E. Proesel, C. W. Baks, *et al.*, "A 71-Gb/s NRZ Modulated 850-nm VCSEL-Based Optical Link," *IEEE Photonics Technology Letters,* vol. 27, pp. 577-580, 2015.

[159]   Tektronix. (2015). *2015 Product Catalog*

[160]   P. RV, B. N, C. J, and W. IH, "Bandwidth studies on multimode polymer waveguides for high-speed board-level optical interconnects," presented at the Proceeding of SPIE, 2015.

[161]   TOPTICA. *FemtoFiber pro*. Available: https://www.toptica.com/products/psfs-fiber-lasers/femtofiber-pro/

[162]   covesion. (2013). *MSHG1550-0.5-xx*.

[163]   T. Lucatorto, M. D. Graef, F. Dunning, and R. Hulet, *Electromagnetic Radiation: Atomic, Molecular, and Optical Physics: Atomic, Molecular, And Optical Physics: Electromagnetic Radiation*: Academic Press, 1997.

[164]   P. Vasil'ev, "Ultrafast Diode Lasers, Fundamentals and Applications," Boston, MA: Artech House, 1995.

[165]   J. Chen, N. Bamiedakis, T. J. Edwards, C. T. Brown, R. V. Penty, and I. H. White, "Dispersion studies on multimode polymer spiral waveguides for board-level optical interconnects," in *IEEE Optical Interconnects Conference*, 2015, pp. 26-27.

[166]   Z. Haas and M. A. Santoro, "A mode-filtering scheme for improvement of the bandwidth-distance product in multimode fiber systems," *Journal of Lightwave Technology,* vol. 11, pp. 1125-1131, 1993.

[167]   J. Chen, N. Bamiedakis, P. Vasil'ev, R. V. Penty, and I. H. White, "Bandwidth enhancement in multimode polymer waveguides using waveguide layout for optical printed circuit boards," in *Proc. Conf. Opt. Fiber Commun.*, Anaheim, CA, USA, 2016, paper W1E. 3.

[168]   R. S. E. John, C. M. Amb, B. W. Swatowski, W. K. Weidner, M. Halter, T. Lamprecht, *et al.*, "Thermally Stable, Low Loss Optical Silicones: A Key Enabler for Electro-Optical Printed Circuit Boards," *Journal of Lightwave Technology,* vol. 33, pp. 814-819, 2015.

[169] C. E. Tabor, B. W. Swatowski, F. Kajzar, C. M. Amb, S. K. Breed, T. Kaino*, et al.*, "Flexible, stable, and easily processable optical silicones for low loss polymer waveguides," vol. 8622, p. 862205, 2013.

[170] N. Bamiedakis, F. Shi, D. Chu, R. V. Penty, and I. H. White, "High-Speed Data Transmission Over Flexible Multimode Polymer Waveguides Under Flexure," *IEEE Photonics Technology Letters,* vol. 30, pp. 1329-1332, 2018.

[171] U. Keller and L. Gallmann, "Ultrafast Laser Physics," *Science* vol. 286, p. 1507, 1999.

[172] D. J. Kane and R. Trebino, "Characterization of arbitrary femtosecond pulses using frequency-resolved optical gating," *IEEE Journal of Quantum Electronics,* vol. 29, pp. 571-579, 1993

[173] R. Trebino. *Light-Pulse-Measurement Tutorial*. Available: http://www.frog.gatech.edu/tutorial.html

[174] S. Linden, J. Kuhl, and H. Giessen, "Amplitude and phase characterization of weak blue ultrashort pulses by downconversion," *Optics Letters,* vol. 24, pp. 569-571, 1999.

[175] G. Stibenz and G. Steinmeyer, "Interferometric frequency-resolved optical gating," *Optics Express,* vol. 13, pp. 2617-2626, 2005.

[176] J. Beals, O. Hadeler, S. M. Morris, T. D. Wilkinson, R. V. Penty, and I. H. White, "Electro-optic Integration of Liquid Crystal Cladding Switch with Multimode Passive Polymer Waveguides on PCB," presented at the Conference on Lasers and Electro-Optics/International Quantum Electronics Conference, 2009.

[177] A. Inoue and Y. Koike, "Low-Noise Graded-Index Plastic Optical Fiber for Significantly Stable and Robust Data Transmission," *Journal of Lightwave Technology,* vol. 36, pp. 5887-5892, 2018.

[178] A. Inoue, T. Sassa, K. Makino, A. Kondo, and Y. Koike, "Intrinsic transmission bandwidths of graded-index plastic optical fibers," *Optics Letters,* vol. 37, pp. 2583-2585, 2012.

[179] A. Inoue, T. Sassa, R. Furukawa, K. Makino, A. Kondo, and Y. Koike, "Efficient group delay averaging in graded-index plastic optical fiber with microscopic heterogeneous core," *Optics Express,* vol. 21, pp. 17379-17385, 2013.

[180] Y. Koike, N. Tanio, and Y. Ohtsuka, "Light Scattering and Heterogeneities in Low-Loss Poly(methylmethacrylate) Glasses," *Macromolecules,* vol. 22, pp. 1367-1373, 1988.